

Remote Sensing Series 48

Maurice Rüegg

**Ground Moving Target Indication
with Millimeter Wave
Synthetic Aperture Radar**



Remote Sensing Laboratories
University of Zürich
2007

Remote Sensing Series Editorial Board:

Prof. Dr. K. I. Itten, Prof. Dr. D. Nüesch, Dr. E. Meier, Dr. T. Kellenberger,
Dr. M. Kneubühler, Dr. D. Small

Rüegg Maurice

**Ground Moving Target Indication with Millimeter Wave
Synthetic Aperture Radar**

Remote Sensing Series 48 – Zurich: Remote Sensing Laboratories

ISBN: 978-3-03703-014-1

<http://www.rs1.ch>

© 2007 — Maurice Rüegg, University of Zürich, Switzerland. All rights reserved.

Prepared with L^AT_EX 2_ε.

Printed by the Druckerei der Zentralstelle der Studentenschaft der Universität Zürich.

This publication was accepted as a dissertation by the Faculty of Science of the University of Zurich in the spring semester 2007 on the basis of expert advice by Prof. Dr. Klaus I. Itten (Department of Geography, University of Zurich), Prof. Dr. Daniel Nüesch (Department of Geography, University of Zurich), and Dr. Helmut Essen (Research Institute for High Frequency Physics and Radar Technology of the Research Establishment for Applied Natural Sciences FGAN-FHR e. V., Wachtberg).

Die vorliegende Arbeit wurde von der Mathematisch-naturwissenschaftlichen Fakultät der Universität Zürich im Frühlingsemester 2007 aufgrund der Gutachten von Prof. Dr. Klaus I. Itten (Geographisches Institut, Universität Zürich), Prof. Dr. Daniel Nüesch (Geographisches Institut, Universität Zürich) und Dr. Helmut Essen (Forschungsinstitut für Hochfrequenzphysik und Radartechnik der Forschungsgesellschaft für Angewandte Naturwissenschaften FGAN-FHR e. V., Wachtberg) als Dissertation angenommen.

Doctorate Committee: Prof. Dr. Klaus I. Itten (Chair), Prof. Dr. Daniel Nüesch, Dr. Erich Meier, and Dr. Konrad Schmid.

About the Cover: MEMPHIS 35 GHz SAR image with a resolution of 0.2 m showing a section of the highway A12 in western Switzerland near the village of La Verrerie, crossed by a railroad and a road bridge.

To my parents

*In memory of my grandfather, Alois Rüegg,
who knew about the value of both educated knowledge and common sense*

Abstract — Ground moving target indication (GMTI) for synthetic aperture radar (SAR) provides information on non-static objects in radar imagery of a static ground scene. While general applications cover a wide area of topics from ocean current measurements to glacier ice flow, millimeter wave (mmW) SAR is well suited for traffic monitoring, reconnaissance, and identification of special target movements including vibration and rotation. Through a thorough motion analysis in a standard SAR system model, this dissertation shows the effects of constant target motion, acceleration, vibration, and rotation in mmW SAR theoretically and in simulated and real data.

An efficient approach for GMTI is the use of multi-channel SAR systems for a space- and time-variant analysis of moving targets. This allows the indication, correction of position displacement, and estimation of radial velocity components of moving targets in a SAR image. The small radar wavelength of mmW SAR offers very sensitive movement detection and measurements. The work at hand includes theoretical considerations specific to mmW SAR GMTI, an adaptive algorithm to collect velocity and position information on moving targets with mmW amplitude-comparison monopulse radar, and a discussion on GMTI blind speed elimination and target velocity ambiguity resolving by dual-frequency SAR. To determine the capabilities of both, system and algorithm, four large-scale experiments with the FGAN MEMPHIS mmW system in different environments are presented.

Zusammenfassung — Die Bewegtzilerkennung (ground moving target indication—GMTI) bei Radar mit synthetischer Apertur (synthetic aperture radar—SAR) liefert Informationen zu bewegten Objekten in Radarbildern der unbewegten Erdoberfläche. Während allgemeine Anwendungen so unterschiedliche Themen wie Messungen von Meeresströmungen und Gletschereisfluss beinhalten können, ist Millimeterwellen (mmW) SAR gut geeignet für Aufgaben in der Verkehrsüberwachung, Aufklärung und der Identifikation von speziellen Bewegungen wie Objektvibrationen und -rotationen. Mittels einer ausführlichen Analyse von Bewegungen in einem SAR Systemmodell zeigt diese Dissertation die Effekte von konstanten und beschleunigten Zielbewegungen wie auch von Vibrationen und Rotationen in mmW SAR auf.

Ein effizienter Ansatz der Bewegtzilerkennung ist der Einsatz von mehrkanaligen SAR-Systemen und einer räumlich und zeitlich variierenden Analyse von bewegten Radarzielen. Dadurch wird sowohl eine Indikation wie auch eine Korrektur von Positionsverschiebungen im SAR Bild und eine Schätzung der radialen Geschwindigkeitskomponente solcher Ziele möglich. Die kleine Wellenlänge des Radars bei mmW SAR bietet eine hochempfindliche Bewegungsdetektion und Messung der Objektgeschwindigkeit. Die vorliegende Arbeit bespricht theoretische Überlegungen, die spezifisch für mmW SAR GMTI sind, einen adaptiven Algorithmus, um Geschwindigkeits- und Positionsinformationen von Bewegtzielen mit Amplituden-vergleichendem Monopuls Radar zu erhalten und eine Diskussion zur Beseitigung von GMTI Blindgeschwindigkeiten und Mehrdeutigkeiten der Objektgeschwindigkeit mittels Zweifrequenz-SAR. Vier grossangelegte Experimente mit dem FGAN MEMPHIS mmW System in unterschiedlichen Umgebungen werden vorgestellt.

Preface

It was on April Fool's Day 2003 that I sat at my new desk for the first time. It is a good date to remember and fortunately, I was not sitting there all alone, but was surrounded by people making sure that my dissertation about to begin would not become a fool's errand. The success of my efforts towards an analysis of moving targets in synthetic aperture radar is certainly due to all those people sitting at desks around me and a few more at desks across offices, buildings, cities, and countries. My desk was provided for by the Remote Sensing Laboratories of the University of Zurich.

When I did not even know what a SAR is, Erich Meier offered me an opportunity to find out about its deep-down details. He led me towards SAR signal processing, interferometry, and finally ground moving target indication. Together, we planned and conducted mmW SAR experiments both complicated and imaginative—and sometimes maybe a bit whimsical.

Overseeing my ideas and directing me away or around many problems with ease was Daniel Nüesch. He was there to hear my concerns, whether theoretical, practical, technical, or human in nature. And he was there to hear them at seven in the morning or seven at night, be it Monday or Sunday.

I am thankful to Klaus Itten for accepting me as his student, giving me a chance towards a doctorate, and providing such a calm and productive environment of science and humanity. Mostly in the background and invisible, it was with him where all the strings were pulled.

Helmut Essen acted as co-examiner for my thesis. I am indebted to him for this and even more for his extremely generous and informal cooperation with our institute for the last few years. He and his team at FGAN-FHR have designed and built one of the most amazing experimental radar systems of our time—MEMPHIS. It was the data from this system that have made my algorithms become nuts and bolts. Amongst his team, I would like to mention Manfred Hägelen and thank him for his ingenious input to my work. Manfred, along with Thorsten Brehm, Anika Kurz, Hartmut Schimpf, and Alfred Wahlen have shown unlimited patience when explaining to me the quirks of MEMPHIS or discussing the planning of our aforementioned whimsical experiments.

We could not have done all these experiments without the technical, logistical, and financial support from the procurement and technology center of the Swiss Federal De-

partment of Defence (*armasuisse*) where Peter Wellig and Konrad Schmid constantly work for a better understanding of SAR and SAR applications. In the field, their ideas were pragmatically implemented by Erich Dörr, Ueli Schwarz, and their teams, never impressed by the height of the snow, the intensity of the downpour or the steepness of the mountain slope.

There were many more people involved in the experiments. I do not want to start naming names because I am afraid I will leave someone out. All of them have my thanks: the pilots, flight engineers and load masters in their helicopters and airplanes, the engineers from the Swiss Federal Office of Metrology (METAS), the administrative staff of the airfield Emmen and of the various testing grounds we were allowed to use, and finally my friends and co-workers from the lab. Here, I dare naming some names again: thanks to Dave for the lead, Schubi for the sound, Zubi and Oli for a high entropy, Noldi for all things ultra wide and very low, Jörg for a continuous phase, Christophe for the friendly takeover, Fortunat for the rookie months, Felix for some cheerful depressions, Otti for the chilling and flexing, and Michi for the atmosphere.

Finally, I would like to mention those closest to me, who made and make me the person I am. You know who you are.

Zollikon
October 2006

Contents

Summary	i
Preface	iii
1 Introduction	1
1.1 Contributions to SAR GMTI	2
1.2 Outline	3
2 Theory of SAR and GMTI	5
2.1 Synthetic Aperture Radar	5
2.1.1 Focusing Raw SAR Data	6
2.2 Millimeter Wave SAR	12
2.3 Opportunities and Applications of SAR GMTI	13
2.4 State of the Art in SAR Ground Moving Target Indication	14
2.5 InSAR - A Single Pass ATI Experiment	15
2.5.1 Principles and Applications	16
2.5.2 Theory	18
2.5.3 Experimental Data	22
2.5.4 Discussion	26
3 Target Movement	29
3.1 General Effects in SAR Imagery	29
3.2 System Model	31
3.3 Signal Theory	32
3.3.1 Static Target Returns	32
3.3.2 Examples	33

3.4	Time-Frequency Analysis	35
3.5	Constant Target Movement	38
3.5.1	Visual Effects	39
3.5.2	Time-Frequency Analysis	42
3.6	Target Acceleration	44
3.6.1	Visual Effects	44
3.6.2	Time-Frequency Analysis	45
3.7	Target Vibration	46
3.7.1	Analysis of Simulated Data	48
3.7.2	Analysis of Vehicle Vibration	51
3.8	Target Rotation	54
3.8.1	Analysis of Simulated Data	56
3.8.2	Rotation of a Reflector and of a Radar Dish	58
3.9	Discussion	63
4	Dual-Frequency Monopulse GMTI	67
4.1	Monopulse Radar	68
4.1.1	Terminology, Definitions, Notations and Concepts	68
4.1.2	Amplitude Comparison Monopulse	71
4.1.3	The Monopulse Ratio and the Monopulse Curve	73
4.2	Monopulse SAR	76
4.2.1	Amplitude-Comparison Monopulse mmW SAR	77
4.2.2	The MEMPHIS SAR System	77
4.3	Dual-Frequency Information	78
4.3.1	Theory	78
4.3.2	Differences in SAR Imagery	79
4.4	Dual-Frequency GMTI	80
4.4.1	Theory	81
4.4.2	Endo- and Exo-Clutter Targets	83
4.4.3	Implementational Aspects	84
5	Experimental Results with Dual Frequency GMTI	89
5.1	Controlled Environment GMTI	89
5.2	Field Paths GMTI	94

5.3	Freeway GMTI	100
5.4	Vibration, Rotation, and Targets of Opportunity	104
5.5	Discussion	106
6	Conclusion	109
6.1	Summary of Results	109
6.1.1	Analysis of Target Movement	109
6.1.2	GMTI	110
6.2	Possible Directions for Further Research	111
A	The FGAN MEMPHIS SAR System	113
	List of Figures	117
	List of Tables	121
	List of Acronyms	123
	List of Symbols	125
	Bibliography	131
	Index	143
	About the Author	147

Chapter 1

Introduction

This dissertation shows that millimeter wave synthetic aperture radar is well suited for ground moving target indication. It describes the concepts and signal processing steps necessary for imaging radar remote sensing applications in traffic monitoring, reconnaissance, and target movement identification. To be able to do this three concepts for radar are combined.

The first concept is millimeter wave (mmW) radar. mmW radars are employed in a wide range of commercial, military, and scientific applications for remote sensing, industry, and security. Examples may be as diverse as automobile collision warning sensors, robotic vision, intrusion detection, or size and range measurement for industrial quality control. Among the advantages of the technology compared to lower frequency microwave radars are miniaturization (small and light hardware components and antennas), simplified signal processing, and high achievable resolution. Disadvantages may include shorter propagation ranges than that of other radar systems and a sensitivity to atmospheric attenuation during rain, fog, hail, or snow.

Synthetic aperture radar (SAR) is the second concept and the most prominent one, too. SAR is an imaging radar technology that produces a high resolution mapping of static ground scenes operating on an airborne or spaceborne carrier platform. It overcomes the general weakness of radar to provide high cross-range resolution through a moving radar platform and sophisticated signal processing. Applications of SAR cover everything from glacier volume monitoring to earthquake damage assessment and land cover classification.

The third and most specific concept is ground moving target indication (GMTI). It is a topic that has been one of the main aims of airborne radar from the beginning (next to airborne moving target indication) and also one that has intrigued the SAR community for a long time. As the name implies, GMTI for SAR provides information on non-static objects in otherwise static ground scenes.

As we will show during the course of this work, using a mmW SAR sensor for GMTI experiments has several advantages as well as drawbacks. Among the advantages are the relatively small size of the sensor antenna and hardware—suitable for application in ultra-light aircraft and unmanned aerial vehicles (UAVs)—and a high GMTI sensitivity because

of a short wavelength. The usually very small synthetic aperture of mmW SAR reduces target smearing and defocus, especially at high target velocities. The main drawbacks are a short signal range due to tropospheric attenuation at these wavelengths, large target Doppler ambiguities resulting in small unambiguous target velocity measurements, and extremely short baselines in interferometric applications.

This dissertation, combining the three concepts, would be worth much less if we did not have an operational system to underlay theoretical results and simulations with. Fortunately, there exists with MEMPHIS a "multi-frequency experimental monopulse high-resolution interferometric system" designed and built by the German FGAN-FHR (Research Establishment of Applied Science for High Frequency Physics and Radar Techniques) [1]. During the course of four large-scale experiments with MEMPHIS, we could gather enough data to show the correctness of our algorithms and make the following contributions to the realm of radar signal processing.

1.1 Contributions to SAR GMTI

Using mmW SAR for GMTI poses problems not encountered in general GMTI with SAR. The wavelength is short, Doppler effects are large and signal phase is extremely sensitive.

Objectives of this dissertation: GMTI in mmW SAR demands specific requisites regarding system design, signal processing, and information extraction. The aim of the work at hand is to present solutions for the latter two point, verified by simulations and experimental results. Concerning the first point, suggestions are given as to what an ideal sensor might look like, keeping in mind that real systems are a compromise meeting many different specifications with quite often opposite design requirements.

Specifically, this dissertation investigates the following topics:

- Four types of target movements are considered for their effects in mmW SAR imagery: constant velocity in any direction, acceleration in any direction, vibration with amplitudes and frequencies similar to those of real vehicle engines, and target rotation. The advantages of mmW SAR towards these effects are described in detail.
- A concise mathematical analysis of target movements compared to mmW radar characteristics allows a theoretical evaluation on which movements may be detected. Findings are verified through simulations and real data. Comparisons between simulations and real data are done with the additional help of time-frequency analyses.
- Specific estimations are conducted regarding the range of target velocities, the influences of non-constant speed and acceleration, the intensity of vibrations, and the type of rotation causing detectable signatures in SAR signals.

- The influence of SAR background clutter on target movement detectability is discussed.
- Specific algorithms have been developed to detect target movements, their type and magnitude in mmW SAR.

Algorithmic contributions to the dissertation include:

- a complete and efficient simulation model for all four movements of constant speed, acceleration, vibration, and rotation. While most effects have been analyzed before, they are rounded out and set in relation to each other in this work.
- a robust amplitude-comparison monopulse method for GMTI with mmW SAR. It allows a fully automatic detection of targets with a radial velocity in SAR imagery, a correction of their displacement induced by this radial velocity component, and an exact estimation of this velocity component.
- a method of dual-frequency GMTI to resolve velocity ambiguities and blind target speeds—common aliasing effects in radar signal processing.
- measurement of many target types including trucks, cars, and radar dishes in mmW SAR, often as a first publication in the open literature.

A verification of the algorithms could be accomplished with the help of the four above-mentioned large-scale experiments that included analyses of multiple vehicles at different velocities in different environments, moving in convoys or not. Broadening of application towards targets of opportunity could be shown. Finally, a specifically developed set-up to simulate rotation as well as imaged rotating radar dishes and vibrating trucks further contributed to the verification.

1.2 Outline

This work is a logically structured discussion of GMTI for mmW SAR. It starts in Chapter 2 with necessary preliminaries of SAR and an overview of the state of the art in the topic regarding signal processing and interferometric techniques. Furthermore, the chapter lists many of the most relevant references to other works in the general fields of SAR processing, mmW SAR and GMTI. The current state of the art in GMTI, along-track interferometric SAR is described theoretically and illustrated by an extensive example with an airborne sensor, including a discussion of results.

Chapter 3 describes and uses a common SAR geometry and system model to explain general effects of moving targets in SAR and mmW SAR. This model is extended to simulate and discuss constant motion, acceleration, vibration and rotation of targets.

Simulations as well as real data examples are analyzed for visual effects of focused targets in the time domain as well as—with the help of time-frequency distributions—for signatures of pulse-compressed target returns in the range-Doppler domain. Parts of the chapter have been published in [2].

In Chapter 4, an algorithm for mmW amplitude-comparison monopulse SAR processing is developed. It is able to detect target movement in SAR, measure average target velocity and apply a position correction in the SAR image via so-called $\Sigma\Delta$ processing. A second algorithm eliminates the problems of target Doppler ambiguity and blind speed by making use of dual-frequency information. The chapter also makes it clear why the common approach of ATI SAR discussed in Chapter 2 does not work for mmW SAR GMTI. The algorithms and some of the results have been published in [3] and [4].

In Chapter 5, results from four experiments with the airborne mmW SAR MEMPHIS [1] are shown. An airfield offered an ideal controlled environment for a first experiment under almost ideal but realistic conditions, with multiple targets and a straight target path on the airfield runway, two different but constant target velocities, and an open view on the scene from the SAR with low clutter. From the experiment, frequency spectra, processed SAR images with position corrected moving targets, and accurate target velocities and positions are presented. To verify the developed algorithm, differential GPS (dGPS) measurements of all target positions and movements were recorded during the experiment and compared to the GMTI results.

A second experiment, intended as an extension of the first one, compares dGPS measurements to SAR GMTI results for slow-moving targets on a field path. Vehicles of the same type as in the first experiment were used. Environment conditions were far from ideal with a twisting target path, clutter from trees, meadows, and rocks, and non-constant target velocities.

More data collected from vehicles on a freeway (targets of opportunity) during a third experiment show the potential for fast moving target indication with mmW SAR. As ground truth, traffic radar and laser measurements were used.

Further results of the developed GMTI algorithm are presented when trying to detect vibration and rotation in a forth and last experiment. As a byproduct, more targets of opportunity on main roads are shown that happened to be in the same scene as the rotating and vibrating objects. They are taken as final proof to the successful working of the algorithms.

Finally, this work concludes with a summary of results and possible directions for further research in Chapter 6.

Chapter 2

Theory of SAR and GMTI

The following sections of this chapter discuss the necessary preliminaries of SAR GMTI and give an overview with many references to the theory and processing of stripmap SAR, mmW specific considerations, and the state of the art in GMTI—including a short introduction to and a data example of along-track interferometry (ATI) with SAR.

2.1 Synthetic Aperture Radar

Synthetic aperture radar was invented and filed for patent in 1954 by Carl A. Wiley [5]. Ever since, it received much attention from the radar community, with dozens of conferences dedicated to the topic each year and countless articles in scientific journals.

Considering the specific system design, a SAR is a coherent radar system. A radar is called coherent when the first wavefront in each pulse is separated from the last wavefront of the same polarity in the preceding pulse by some integral number of wavelengths. For example, if the wavelength is exactly 3 m, the separation between pulses may be 300,000 m or 300,003 m, but not 300,001 m or 300,000.5 m.

A SAR is mounted on board of a flying platform, either airborne on some kind of aircraft or spaceborne on a satellite. Its antenna main beam is looking in a direction perpendicular to the flight direction. The radar look direction is called range or slant range and the time in range is the fast time because of the speed of light with which the radar waves are emitted. The flight direction is normally called azimuth or cross-range, and the time in azimuth is referred to as slow time because of the slow speed of the platform compared to the speed of light.

There are two basic types of radar: pulsed and continuous wave radars [6]. The pulsed radar is the more conventional radar which transmits a burst of energy and waits for its echo to be reflected back to the antenna. After a specific period of time—the pulse repetition interval (PRF)—another pulse will be sent followed by another listening period. Since radar waves travel at the speed of light, the range to the reflecting object can be calculated.

Continuous wave (CW) radars transmit a constant beam of radar energy from a transmitter antenna. When a CW radar illuminates a moving object, such as an aircraft or a car, the radar waves return to a separate receive antenna with a frequency that is slightly higher (if the object is moving towards the radar) or lower (if it is moving away from the radar) than the frequency of the transmitted radar energy. By measuring this Doppler shift the radial speed of the object can be determined. In a pure CW radar, the range to the object cannot be determined. However, by modulating the frequency of the radar over time, the object's range can be calculated with a frequency modulated continuous wave radar (FMCW radar).

In this work we concentrate on pulsed radar systems. Since the antenna beam in azimuth direction is quite large, each point on the terrain surface is reached by more than one pulse of the radar during its movement. Through the proper combination of all the echoes from the same point it is possible to obtain a higher resolution in azimuth direction than with just one echo. This may inversely be seen as adding up the antenna aperture along the flight track for all echoes of a single point as long as it is inside the antenna beam and is thus called a synthetic aperture radar or SAR. The concept is discussed in more detail in the following Chapter 2.1.1.

Fig. 2.1 shows the geometry of a SAR and illustrates the meaning of terms, including range and azimuth direction, which are commonly used when talking about SAR. The radar antenna has a footprint defined as the area on the surface where the antenna power is still 50% (-3 dB of the nominal maximum gain in both range and azimuth direction). This footprint covers a swath on the surface that results from the moving SAR platform and the sensor off-nadir angle. The time that a single point on the ground is inside the moving antenna footprint is called the aperture time or dwell time of the radar. Such a single point is called a point target while any other object is simply called a target. The radar looks from an orbit (spaceborne) or a flight track (airborne) to the ground and records the echoes of its own signal as it is reflected from the terrain surface in slant range, the geometry that results from the look angle of the radar.

In the case that the SAR sensor is not looking exactly perpendicular to the flight direction, we have a squinted situation. Such a squint angle may result from aircraft drift or earth geometry relative to a satellite orbit. The radar looks at targets ahead or behind the aircraft. Thus, these targets move towards the radar or away from it, resulting in a Doppler shifted frequency spectrum of their return signals.

2.1.1 Focusing Raw SAR Data

There are a number of excellent textbooks that cover the many principles of radar and SAR design [6–11] as well as SAR concepts and signal processing [12–15]. The following short discussion scratches on the surface of SAR image focusing and its general signal processing concepts as far as it is important to the understanding of effects analyzed in Chapter 3 and the algorithms developed in Chapter 4. For a more in-depth and cover-all

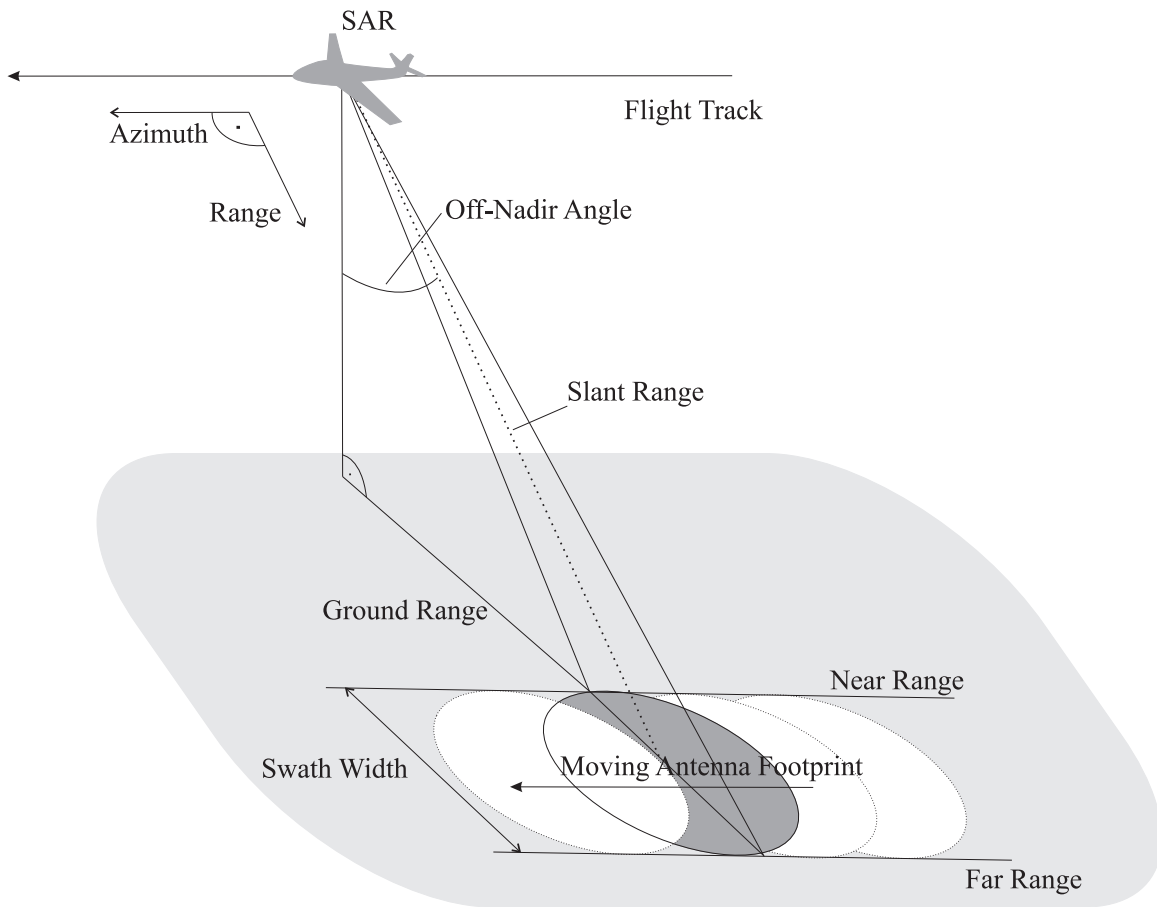


Fig. 2.1: A typical airborne SAR flight geometry including the most important terms of SAR theory.

view of SAR focusing, the reader is referred to the references given above.

2.1.1.1 Range Compression

On the one hand, the sensitivity of a pulsed radar depends on the energy transmitted in the radar pulses. It may be expressed in terms of the average transmitted power, meaning the peak power multiplied by the transmitter duty cycle. On the other hand, the resolution in range depends on the shortness of the pulse length because a long radio pulse is spread over a larger distance than a short one. Hence, sensitivity and resolution seem to require opposite requirements of a high power and short duration pulse, leading ultimately to a Dirac delta function.

The key to solving this problem is the realization that the range resolution of a radar does not necessarily depend on the duration of the transmitted pulse; it depends on the bandwidth of the pulse. For a simple rectangular pulse, the bandwidth W is just $1/\tau_p$,

where τ_p is the pulse duration. However, by manipulating the amplitude and/or phase within the pulse, its bandwidth may be altered without changing its duration. The radar resolution may be changed independently of the average transmitted power.

Range compression, also known as pulse compression, is a signal processing technique designed to maximize the sensitivity and resolution of a radar in the range direction by increasing the pulse bandwidth. Many methods exist to achieve this, including binary phase coding and frequency stepping. The most common method for SAR involves frequency modulation of the transmitted pulses. They are often referred to as chirp pulses, in analogy to the sound of a frequency-modulated audio signal. Mathematically, such a pulse p is defined as a function of the fast time t as

$$p(t) = e^{j(\beta t + \alpha t^2)}. \quad (2.1)$$

α is known as the chirp rate, and β is a linear coefficient. (2.1) implies that we use a carrier frequency f_c defined by

$$\omega_c = 2\pi f_c = \beta + \alpha\tau_p \quad (2.2)$$

where τ_p is the pulse duration, and the signal bandwidth is

$$\omega_W = 2\pi W = 2\alpha\tau_p. \quad (2.3)$$

An example of a chirp pulse is given in Fig. 2.2(a) with $f_c = 50$ MHz, $W = 100$ MHz, and $\tau_p = 2 \mu\text{s}$.

The underlying theory of range compression is the one of the matched filter [14, 15]. The decoding, or compression stage involves correlating the received signal $s(t)$ with a time-reversed replica of the transmitted chirp $p(t)$. $s(t)$ may be a bandpass or a lowpass signal. If it is a bandpass signal, baseband conversion needs to be performed to receive $s_0(t)$. Hence, the matched filtering operation in the time domain is a convolution between the complex conjugate of the reference chirp, $p^*(t)$, and the received signal, returning the desired matched-filtered echo signal

$$s_M(t) = s_0(t) * p^*(t) \quad (2.4)$$

where $*$ denotes a convolution. The Fourier transform of any signal $s(t)$ is defined as

$$S(\omega) = \int_{-\infty}^{\infty} s(t) \cdot e^{-j\omega t} dt. \quad (2.5)$$

Therefore, in the frequency domain, one gets the matched-filtered echo signal

$$S_M(\omega) = S_0(\omega)P^*(\omega). \quad (2.6)$$

It is this operation that is called range compression. Fig. 2.2(b) shows the range compressed signal $s_M(t)$ as it would be returned by a point target. This signal meets the

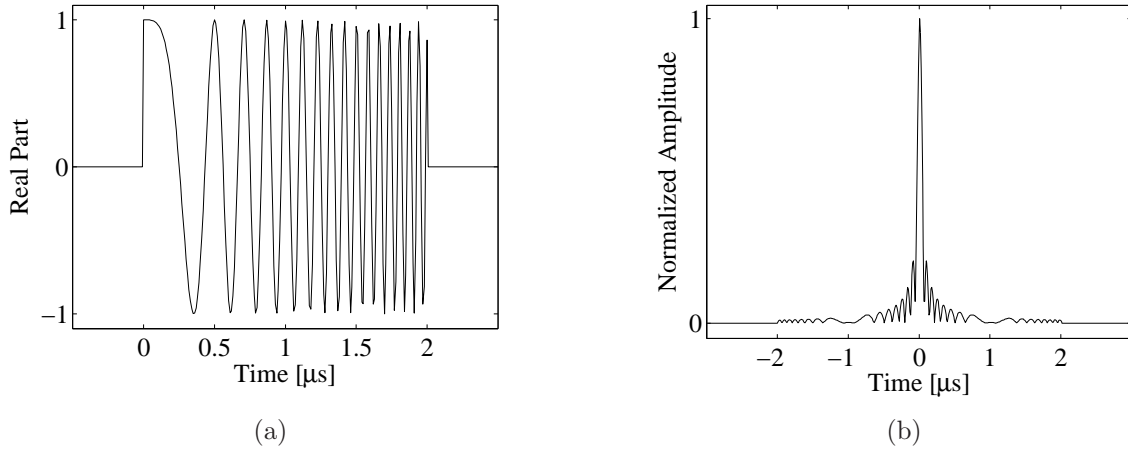


Fig. 2.2: The concept of pulse compression. An emitted radar chirp in (a) is correlated with its time-reversed replica. This matched filtering operation results in the fine resolution signal of (b).

basic requirements of a short peak of high power that were mentioned at the beginning of this chapter.

Through matched filtering, the slant range resolution δ_r achievable with a chirped pulse radar is defined solely by the signal bandwidth W [14]

$$\delta_r = \frac{c}{2W} \quad (2.7)$$

where c is the speed of light.

A further explanation and application of the above concepts and of Fig. 2.2 is given when defining a SAR system model to simulate moving targets in Chapter 3.3.

2.1.1.2 Azimuth Processing

The resolution of a conventional radar in cross-range is very poor since such a radar only measures the time between the transmission of a pulse and the reception of its echo from a target. On the ground, there may well be several targets at the same distance but different angles from the radar, depending on the radar antenna beamwidth. A small beamwidth with good azimuth resolution requires a large antenna.

In 1954, Carl A. Wiley observed that two objects, imaged from a sidelooking radar at slightly different angles with respect to the track of a moving radar, have different speeds relative to the platform, and the radar pulse reflected from the two objects have two different shifts in their frequency according to the Doppler effect [5]. This is the key to SAR that allows a greatly improved along-track resolution of a scene. For SAR, when the antenna beam in azimuth direction is quite large, each point on the terrain surface

is reached by more than one pulse of the radar during its movement, and always with a different Doppler shift. This allows a combination of the pulses over the radar dwell time. Accordingly, a small antenna equals better resolution because its beamwidth is large, resulting in many pulses echoing back from a single target at many Doppler shifts. For a stationary point target at slow-time T and target aspect angle $\varphi(T)$, this Doppler shift depends on the transmitted carrier frequency ω_c as

$$f_d(T) = \frac{v_s \omega_c \sin \varphi(T)}{\pi c} \quad (2.8)$$

where v_s is the sensor velocity in azimuth [14]. Fig. 2.3 illustrates the principle. The distance that a SAR travels over the dwell time on the target is called the synthetic aperture.

Because the Doppler shift depends on the angle $\varphi(T)$, the received frequency from a point target varies as illustrated in Fig. 2.4. This Doppler rate is comparable to the chirped pulse $p(t)$ in fast-time. As a direct consequence, SAR image focusing in azimuth is actually an azimuth compression analogous to range compression. A matched filter of the expected Doppler shift $f_d(T)$ from a point target focuses a SAR image in azimuth. $f_d(T)$ is sometimes called the Doppler history.

Unfortunately, azimuth compression is only then a one-dimensional operation when neglecting the varying distance from the sensor to a point target over the synthetic aperture, given by

$$R(T) = \sqrt{R_0^2 + z^2(T)}. \quad (2.9)$$

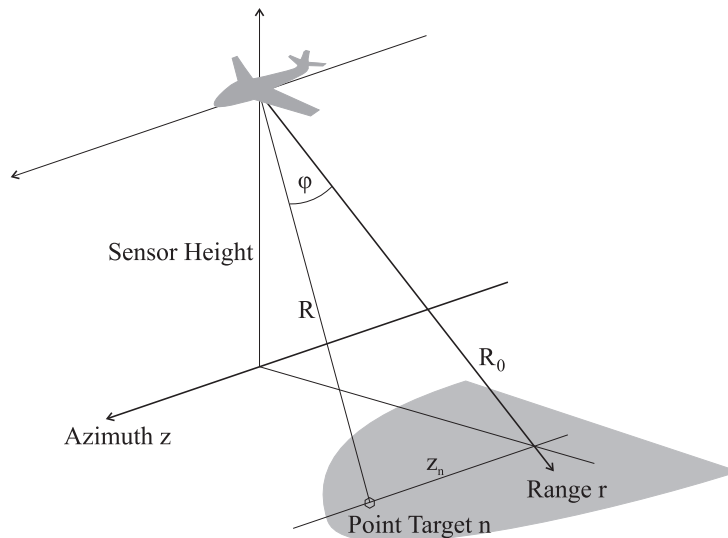


Fig. 2.3: The Doppler shift of a point target is caused by an offset z_n of a point target n in azimuth. By measuring the Doppler shift, the offset z_n may be determined, allowing for a good azimuth resolution.

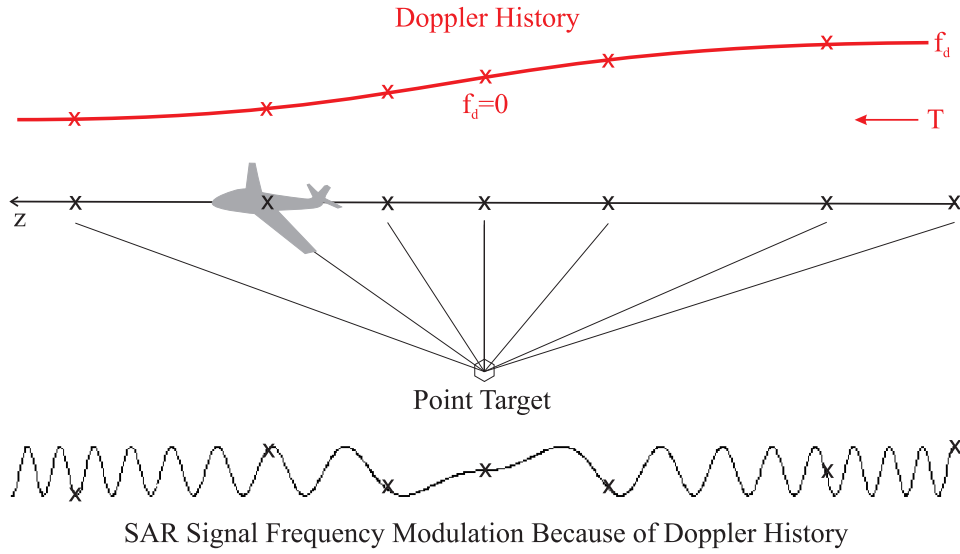


Fig. 2.4: A schematic illustration of the Doppler history as given by (2.8): the reflected Doppler frequency of a static point target depends on the angle between the sensor and the target. It induces a frequency modulation in the azimuth characteristics of the SAR signal.

R_0 is the range of closest approach and $z(T)$ the position of the sensor on the track (see Fig. 2.3). The approximation $R(T) \approx R_0$ is only valid if $R_0 \gg z(T)$. Otherwise, the problem of azimuth compression becomes a two-dimensional one. Today, the approximation is almost never assumed, and there are a great number of solutions to do two-dimensional azimuth focusing, from the time-consuming and exact time-domain backprojection algorithm [13, 16] to many frequency domain algorithms such as range-Doppler [14], $\omega - k$ [13, 17], polar format processing [18], chirp scaling [19–21], or the SPECAN algorithm [12, 22]. A comparison of different algorithms is drawn in [23].

The most beautiful part of SAR azimuth processing is that the theoretically possible azimuth resolution of a focused SAR image can be shown to be directly proportional to the physical antenna length ℓ as [14, 24]

$$\delta_z = \frac{\ell}{2}. \quad (2.10)$$

It turns out that this is an overoptimistic performance [13]. In practice, there is a finite number of measurements in the synthetic aperture T domain and spectral properties of the received signal that make (2.10) an approximation.

2.2 Millimeter Wave SAR

Extremely high frequency (EHF) is the highest radio frequency band. EHF runs the range of frequencies from 30 to 300 GHz, above which electromagnetic radiation is considered to be far infrared light. The band has a signal wavelength of ten to one millimeter, giving it the name millimeter band or millimeter wave, often abbreviated as mmW.

Radio signals in this band are extremely prone to atmospheric attenuation, making them of very little use for long distances applications. Even over relatively short distances, rain fade (absorption by rain) reducing signal strength, is a serious problem [25]. The phenomenon depends on raindrop size; the closer drop size and wavelength match each other, the more attenuation has to be expected. Equally, fog, cloud, haze, dust, and wet snowfall may attenuate signal strength [26].

The EHF band is essentially undeveloped and available for use in a broad range of products and services, including high-speed, point-to-point communications, wireless local area networks, and broadband Internet access. Highly directional signal characteristics permit systems in these bands to be engineered in close proximity to one another without causing interference.

Applications include radar systems with very high resolution [27,28]. Because of shorter wavelengths, the band permits the use of smaller hardware components such as waveguides and antennas than would be required for similar circumstances in the lower bands, to achieve the same high directivity and high gain. The drawback is the aforementioned high atmospheric attenuation. Fortunately, there exist four windows of increased transparency located around 35, 90, 140, and 220 GHz [26].

As a highly specialized derivation of general radar, mmW SAR profits from all these advantages as well as suffers from the disadvantages. Small antennas make it suitable for application in unmanned aerial vehicles (UAVs) [29]. High gain and directivity provide a good signal-to-noise ratio (SNR). A small antenna beam decreases the synthetic aperture and simplifies the azimuth focusing step in the image formation process (see Chapter 2.1.1). At the same time, mmW SAR is only operational at close ranges—flight levels of at most thousands of meters—and certainly not on satellites. The small wavelength poses high requirements on data motion compensation and therefore on navigational data quality. Finally, because the EHF band is essentially undeveloped, there are practically no off-the-shelf hardware solutions and components.

An example of an operational mmW SAR system is shown in Fig. 2.5. It shows the EADS MiSAR 35 GHz mmW SAR for use on UAVs [29]. The system design is very compact and allows for two vertically superposed antennas. There exist quite a few experimental mmW SAR systems, mostly operating at 35 GHz. Unique in this respect is the MEMPHIS system, operating at both 35 and 94 GHz simultaneously, making comparisons between the two frequencies possible.



Fig. 2.5: EADS MiSAR, including the complete hardware and two antennas, photographed during an exhibition at EuSAR 2006 in Dresden.

2.3 Opportunities and Applications of SAR GMTI

For a long time, moving targets in SAR and GMTI algorithms for SAR have intrigued large parts of the radar community [30]. The focus has not only been on the effects of target movement in a SAR image, but also on the wide field of applications made accessible by SAR GMTI. This field obviously includes a range of military applications from simple detection of slow and fast target movement, accurate velocity measurements, and SAR image position correction [31–34] to detection limits [35], foliage penetration GMTI [36], and recognition of special target motion [37] to battlefield awareness and theater intelligence [38].

At least as wide if not wider is the field of civilian, commercial and scientific applications of SAR GMTI. It includes topics from monitoring of volcano activity [39], earthquakes [40], and glacier ice movement [41] with SAR. Water current measurements are possible [42–45] as well as traffic monitoring on a large scale [46, 47]. Many of these topics are only marginally explored today. Sea current measurements have probably received the most attention due to the Shuttle Radar Topography Mission (SRTM) in the year 2000 [48], that delivered the first spaceborne data sets suitable for GMTI. Traffic monitoring could be shown, but SRTM data image resolution at 10 m could not provide information on anything but large trucks [47]. Future missions with Canada’s RADARSAT-2 [49] and especially Germany’s TerraSAR-X [50] will overcome this problem with image resolutions of 3 and 1 m, respectively, and the inherent ability of GMTI. Especially for TerraSAR-X, a science team at the German Aerospace Center DLR is engaged in a large number of traffic monitoring projects, from algorithmic GMTI questions of TerraSAR-X [51] and combining road databases with SAR images [52] to the planning of TanDEM-X opportunities [53].

Most applications today are based on aircraft SAR, however. Airborne platforms are more easily available for GMTI which is still an experimental SAR mode [54] and thus, test are less expensive and risky. Additionally, they do not require the provision for earth rotation, earth curvature, and large sensor-to-target distances as spaceborne sensors would [55]. Examples of airborne SAR GMTI experiments are described in [56] for the German PAMIR, in [57] for the German E-SAR, in [58] for the American AIRSAR, in [54] for the Canadian CV 580, and in [59] for the French RAMSES.

Traditionally, SAR and GMTI are two different radar modes of operation. A single system may have the capability to switch between these modes [60], but combining them to a single mode forces trade-offs in system design and performance. This is the reason why some engineers and scientists oppose the idea of SAR GMTI. Proponents of SAR GMTI counter with the argument that often only a SAR mode radar is available, and extracting GMTI information from there is less expensive and less complex than a second GMTI radar mode.

2.4 State of the Art in SAR Ground Moving Target Indication

GMTI radar and SAR have different design principles. While a GMTI radar needs a pulse repetition frequency (PRF) that is as high as possible to distinguish between echo signals from static clutter and fast moving targets, a SAR normally has a much smaller PRF sufficient for ground Doppler returns from the full antenna aperture. The antenna beam of a GMTI radar is usually narrow to keep the ground clutter spectrum small and ease tracking of a target. A SAR antenna beam is wide to get good azimuth resolution of the covered ground scene.

Nevertheless, when acquiring a SAR image, there may be moving targets in a scene. If we have a high resolution image of the ground and information on moving targets in the radar echo data, why not try and kill two birds with one stone? Why not extract GMTI information from SAR instead of relying on a specialized GMTI radar and having to do data fusion of SAR and GMTI radar? These considerations have led to the field called SAR GMTI.

The effects of smearing, defocusing, and displacement of moving targets in SAR imagery have long been known and are discussed in detail in [30]. Since then, many ingenious methods and techniques for detection, position correction, refocusing, and velocity measurements of moving targets have been developed. Some of the approaches include digital filtering [61], algorithms requiring three prominent points of a target image [62], the application of the fractional Fourier transform [63], or the so-called reflectivity displacement method [64]. Aspects of target acceleration on GMTI algorithms are discussed in [65], and prominent work on constant false alarm rates (CFAR) may be found in [66,67].

We may divide GMTI algorithms into two classes based on whether they require the

use of single- or multi-channel SAR data. Single channel data is obviously less expensive since a single platform with a single transmission and receive channel is needed. However, information content of a single channel is limited, resulting in GMTI algorithms with somewhat mediocre possibilities. Multi-channel SAR requires multiple data channels and offers many more opportunities to extract GMTI data by comparison of those channels in time, space, and frequency. Multiple channels may be located on a single platform as is the case for most airborne platforms and satellites like TerraSAR-X and RADARSAT-2. A conceptual implementation of multiple spaceborne SAR systems by the American Air Force Research Laboratory in 1997 introduced the idea of constellation SAR [68, 69]: spaceborne SAR systems on several small satellites. In [70], the idea was refined and called interferometric cartwheel. A proposal for performance improvement for such a flotilla of SAR system has only recently been published [71]. In Europe, the German TanDEM-X project aims at traffic monitoring with two satellites flying in formation [53].

For single-channel SAR, the most well-known class of GMTI techniques is probably multilooking [72, 73] where the spectral information from the SAR is divided to form multiple subapertures. A target moving parallel to the SAR will cause these spectra to behave differently from those of a static target. Many other methods exist, most of them exploiting moving target signatures in the Doppler domain [74]. For multi-channel SAR, there are many more classes of GMTI techniques, including displaced phase center antenna (DPCA) processing [33, 49, 75] and closely related along-track interferometry (ATI) [45, 76] (see Chapter 2.5.2), which is probably the most popular SAR GMTI technique. Other multi-channel techniques are space time adaptive processing (STAP) [76–82] and time-frequency processing [83–85]. Both classes are adapted from general radar GMTI. They are all capable of detecting radial target movements.

Very specific to SAR is the approach of polarimetric data analysis [86, 87], where the normally redundant VH and HV data channels of polarimetric SAR are analyzed for differences coming from moving targets. Shadow tracking is possible when a SAR image includes an information hole or shadow where a moving target would actually be located, but is shifted in azimuth position because of image focusing effects [88].

A somewhat stand-alone topic is the estimation of along-track velocity of targets. A target movement exactly parallel to the SAR sensor cause neither a Doppler shift in single-channel SAR nor phase differences in interferograms (see Chapter 3). Nevertheless, there are some interesting approaches covering the topic including the use of large filter banks [57].

Finally, there is $\Sigma\Delta$ processing, also known as monopulse processing [33, 89], which is discussed in detail for mmW SAR in Chapter 4.

2.5 InSAR - A Single Pass ATI Experiment

As mentioned in Chapter 2.4 above, along-track interferometry is probably the most common SAR GMTI technique. One of the main reasons for this is its derivation from general

interferometric SAR (InSAR). InSAR is one of the largest fields of SAR research activities with numerous applications. Because of its popularity, the following three sections talk about its principles, its theory, and a GMTI experiment that was something like the starting point for this dissertation.

InSAR refers to the synthesis of conventional SAR high resolution mapping from aircraft as well as satellites and interferometry techniques originally developed in radio astronomy [90] and planetary exploration [91]. As a general technique, InSAR adds an additional dimension to the normally two-dimensional SAR mapping—either in space or time. For a dimension in space, the feasibility of using a pair of SAR images to generate digital elevation models and in particular surface models was first demonstrated in [92] with optical processing techniques and later in [93] where digital signal processing for InSAR was introduced. The first temporal experiment included ocean current measurements in [94].

2.5.1 Principles and Applications

A common radar measures the distance from the sensor antenna to a target reflecting the radar beam. A SAR is able to add a second dimension and determine the location of a target in a plane. A second SAR adds a third dimension; this may be a spatial dimension (height information of the target) or a temporal dimension (target deformation or movement) depending on the SAR antenna configuration:

- In a situation with a spatial baseline B_S , a target is imaged from two different angles at the same time as illustrated in Fig. 2.6(a). This allows the measurement of the target height. It becomes possible to generate topographic maps of an area.
- A temporal baseline B_T means that two SAR measurements are made from the same position but at different times. This may be achieved by mounting two antennas to the same aircraft that must be positioned behind each other in flight direction as seen in Fig. 2.6(b). Since the system looks at the same scene twice, it is able to detect changes and measure velocities of moving objects.
- Mixed baselines combine the above two configurations as in Fig. 2.6(c).

In all three SAR antenna configurations listed above, we differentiate between either making multiple measurements at one single overflight (single-pass interferometry) or flying over the same area twice (two-pass or repeat-pass interferometry) most often with a single sensor. In along-track interferometry, the temporal ATI baseline is the decisive factor on whether one looks at short changes detectable with single pass interferometry (e. g. ocean current measurements [94]) or slow changes with repeat pass interferometry (e. g. glacier ice monitoring [95]).

An important aspect for InSAR is decorrelation. If the velocities of vehicles moving on a highway are to be measured with a temporal baseline, it makes no sense to do this in

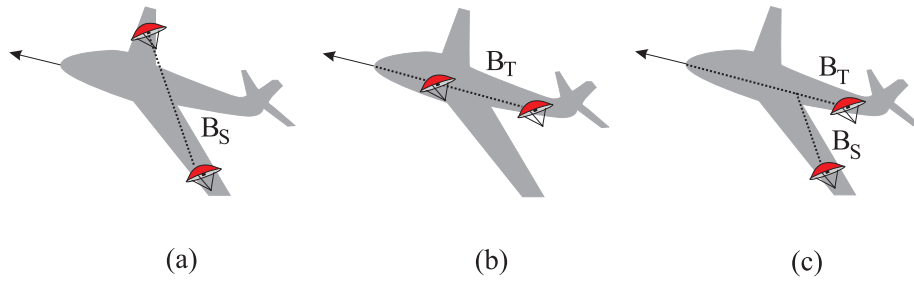


Fig. 2.6: Single pass interferometry with an aircraft and two SAR antennas. a) shows a spatial baseline configuration while b) depicts a temporal baseline. c) is a combination of both — a mixed baseline.

a repeat-pass configuration because all the cars of the first overflight will probably have moved completely out of the scene by the time of the second flight. There will be no correlation of moving objects on the highway. Similarly, spatial baselines that are too large may show a scene from two angles that may have not much in common—comparable to looking at a house from two different sides.

On the other hand, effects such as the very slow movement of the ice in a glacier or the deformation of the Earth surface by an earthquake may only be seen via repeat-pass interferometry. Additionally, the cost of a repeat-pass interferometer is much less (especially for spaceborne systems) because only a single SAR sensor is needed.

Finally, one has to be aware that in a practical situation, we will almost never find a pure spatial baseline B_S or a pure temporal baseline B_T . This is due to imperfect track alignment of an airplane as illustrated in Fig. 2.7 or the impossibility to have two spaceborne SARs covering exactly the same scene from different positions.

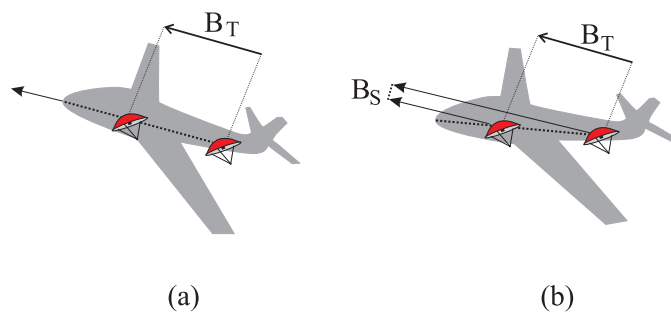


Fig. 2.7: Imperfect flight track for ATI. While two perfectly aligned ATI antennas hold no spatial baseline, slight misalignment or platform drift causes a component B_S between the antennas.

2.5.2 Theory

In the following, a theoretical introduction to InSAR and ATI is given. It is kept short and focuses on the most important steps and formulae for a basic understanding. For an in-depth view, there are some good overview texts of InSAR theory and its principles and applications available in [96–100].

InSAR theory starts where SAR raw data processing stops: at single look complex radar images of a scene. Each pixel of such a complex SAR image in the coordinates of slant range r and azimuth z may be described as

$$s_c(r, z) = A(r, z) \cdot e^{j\phi(r, z)} \quad (2.11)$$

where $A(\cdot)$ is the amplitude of the received signals and ϕ is their phase. Because interferometry exploits the differences of a scene caused by a temporal or spatial baseline of two sensors, we obviously need two images, a master image s_{c1} and a slave image s_{c2} of the same scene to determine these differences. In an interferogram we are most interested in the phase difference between s_{c1} and s_{c2}

$$\Delta\phi(r, z) = \phi_1(r, z) - \phi_2(r, z). \quad (2.12)$$

Obviously, to extract the phase differences $\Delta\phi(r, z)$ the two SAR images s_{c1} and s_{c2} must be perfectly aligned or coregistered [100–103].

When we look at the geometry in Fig. 2.8, it becomes clear where the phase difference of (2.12) comes from. Ranges r_1 and r_2 to the same point on the ground are not of the same length because of different positions and look angles of the SAR sensors. The length of their individual electromagnetic propagation path may be measured by the number of cycles of a wavelength they each contain. A difference of two lengths may be seen as a difference between two such numbers of cycles and thus as a phase shift

$$\Delta\phi = -\frac{2\pi q}{\lambda}(r_1 - r_2) \quad (2.13)$$

with λ the carrier wavelength and $q = 1$ for systems with a single transmitting antenna and $q = 2$ for systems with 2 transmitting antennae where two-way propagation applies [96]¹. The whole term is negative by definition because the phase ϕ may be seen as the change in Doppler frequency f_d which is negative when range between sensor and target increases. A negative Doppler shift implies a shortening of the echoed wavelength.

The situation is different in an along-track interferometer. The baseline is temporal and the ranges r_1 and r_2 are theoretically the same. An interferogram thus ideally shows a constant phase difference of $\Delta\phi = 0$. The only phase deviations may come from range

¹There are different modes for two transmitting antennas as well. a) Each antenna receives only those reflected signals that it has sent itself. b) The first antenna sends a signal that the second one receives and vice versa. This is often called "ping-pong" mode. For both modes, the difference in range between the antennae is included twice in the signal path difference.

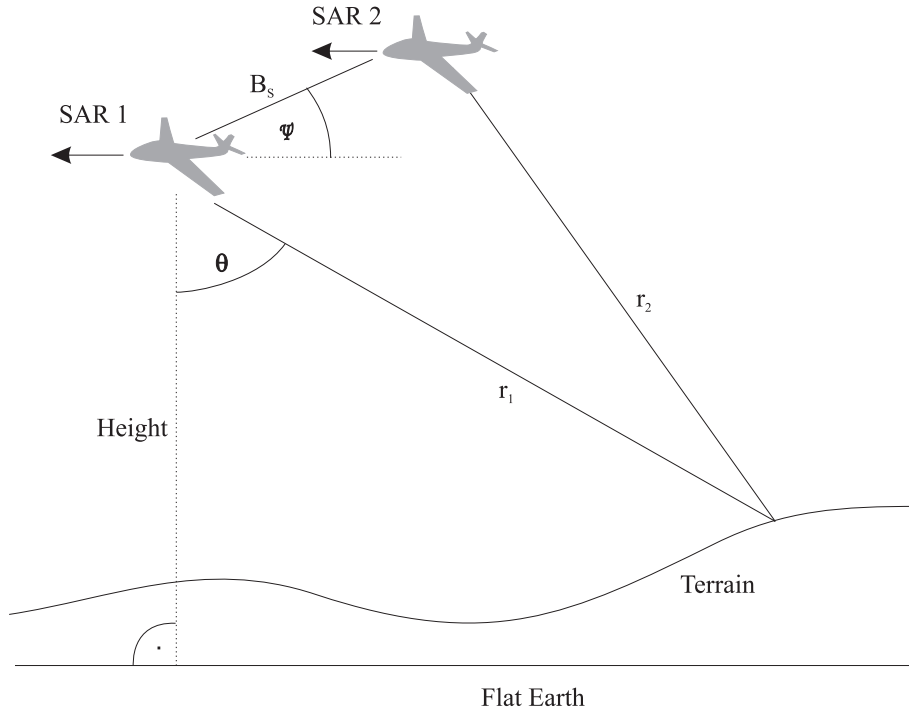


Fig. 2.8: Geometry of a two-pass cross-track interferometry experiment.

changes during the temporal baseline B_T that are caused by terrain deformation or moving objects.

To calculate the exact value of $\Delta\phi$ for a pixel in an interferogram, the two images s_{c1} and s_{c2} must first be aligned or coregistered via a correlation of their amplitude values to ensure the comparison of corresponding areas in the images. This is possible in sub-pixel accuracy. The interferogram of the two coregistered images is calculated as

$$i(r, z) = s_{c1}(r, z) \cdot s_{c2}^*(r, z) = A_1(r, z)A_2(r, z)e^{j(\phi_1(r, z) - \phi_2(r, z))} \quad (2.14)$$

where $*$ denotes a conjugate complex value. The phase of this complex interferogram i is

$$\Delta\phi(r, z) = \text{atan} \frac{i_{im}(r, z)}{i_{re}(r, z)}. \quad (2.15)$$

Contributions to the interferometric phase come from many sources. Some of them are known in advance, some are computable and some are random. The most important ones are

- topographic phase, known from a digital elevation model,
- surface deformations (earthquakes, erosion),

- surface movements (landslides, water currents, object movement due to wind, moving vehicles),
- earth curvature,
- aircraft track errors or satellite orbit errors,
- random phase noise,
- and ionospheric and tropospheric delays for spaceborne InSAR.

When a flat earth ellipsoid is assumed as a surface model, this flat surface causes a fringe pattern in the interferogram that is due to the spatial baseline vector between the two SAR sensors. Fig. 2.9 illustrates this phenomenon. It is explained via the perpendicular baseline length B_{\perp} , defined as

$$B_{\perp} \equiv B \cos(\theta - \psi) \quad (2.16)$$

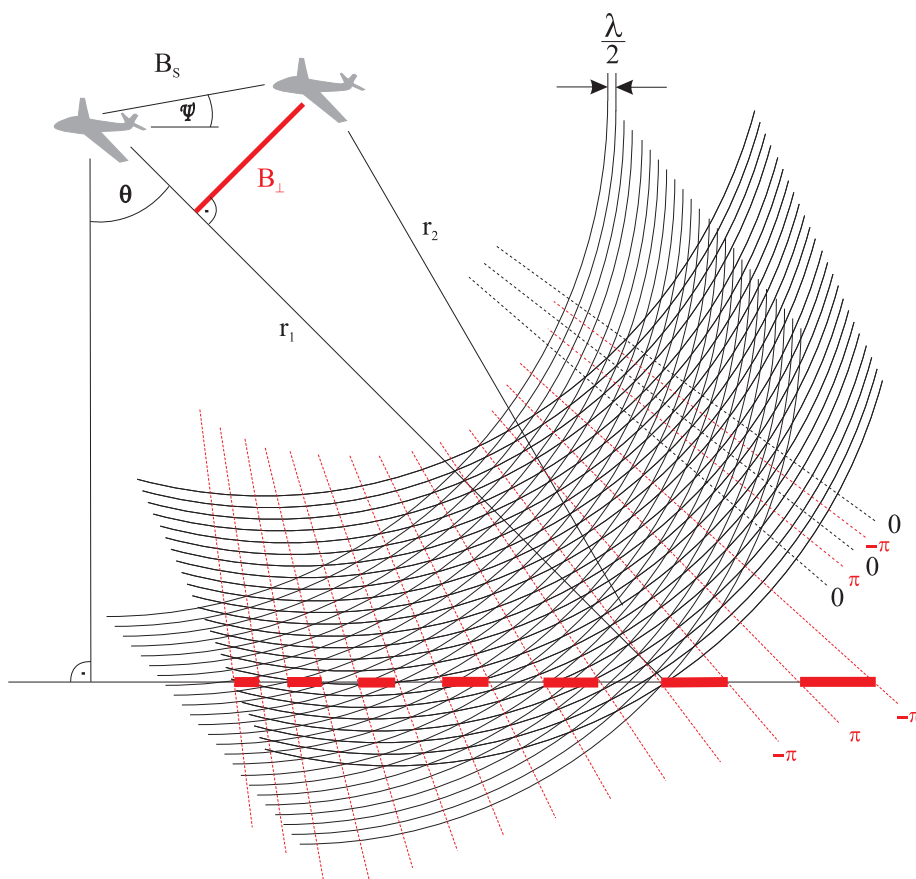


Fig. 2.9: The fringe pattern on a flat surface caused by a spatial baseline with iso-phase lines of both SAR with $\lambda/2$ spacing and the range dependent phase length on a flat Earth.

where B is the length of the spacial baseline, θ the off-nadir angle in near range and ψ the angle between the tangent plane and the baseline vector (see Fig. 2.8). The phase slope over range as visible in Fig. 2.9 may be expressed as [97]

$$\frac{\partial\phi(r, z)}{\partial r} = -\frac{2\pi q}{\lambda} B_{\perp} \cdot \frac{\partial\phi(r, z)}{\partial\theta} \quad (2.17)$$

with $q = 1$ for a single transmitting antenna and $q = 2$ for two transmitters. With this knowledge, interferogram flattening may be performed: the phase of the flat earth influence is removed from an interferogram.

A limitation of InSAR is that the interferometric phase of (2.15) may only be known modulo 2π . Hence, ambiguities appear resulting in a repetition of values and an InSAR-typical phase pattern called fringes. The fringe rate due to phase differences or the value of ambiguity—which may be seen as the topographic height difference of one full phase cycle—is given in [100] as

$$h_{2\pi} = \frac{\lambda r \sin\theta}{qB_{\perp}}. \quad (2.18)$$

This limitation of phase ambiguities may be resolved with phase unwrapping techniques that estimate unambiguous phase values from observed phase data as described in [96,104].

To check the quality of a flattened interferogram, a coherence map may be computed. The coherence $|\gamma|$ is a measure of phase noise, and the normalized coherence is given by the complex correlation between the two coregistered SAR images of $s_{c1}(r, z)$ and $s_{c2}(r, z)$ as

$$\gamma(r, z) = \frac{\langle s_{c1}(r, z) \cdot s_{c2}^*(r, z) \rangle}{\sqrt{\langle |s_{c1}(r, z)|^2 \rangle \langle |s_{c2}(r, z)|^2 \rangle}} \quad (2.19)$$

where the angles $\langle \rangle$ denote an ensemble average and s_{c2}^* is the conjugate complex of s_{c2} . Then, the interferometric coherence is given as the sum of complex correlations for all values of r and z with

$$|\gamma| = \sum_r \sum_z \gamma(r, z). \quad (2.20)$$

In general the coherence in the imaged scene changes from area to area. The problem is that the ensemble average may not be estimated on the basis of a single pixel from two SAR images. However, coherence in stationary regions may still be estimated accurately when ensemble averages are substituted by spatial averages (i.e. by assuming mean ergodicity) [105].

In practice, $|\gamma|$ is calculated from (2.19) by substituting the ensemble averages with spatial sampled averages (assuming process ergodicity in a small estimation area of $N \times M$ pixels). However, even if the ergodicity hypothesis holds and all the scatterers within the estimation area are independent with identical statistical properties, the two images differ by a deterministic phase (i. e. the interferometric phase $\Delta\phi(r, z)$) that has to be estimated

and compensated. The result is called a phase corrected coherence map given as

$$\gamma'(r, z) = \frac{|\sum_{r=0}^M \sum_{z=0}^N s_{c1}(r, z) \cdot s_{c2}^*(r, z) \cdot e^{-j\Delta\phi(r,z)}|}{\sqrt{\sum_{r=0}^M \sum_{z=0}^N |s_{c1}(r, z)|^2 \cdot \sum_{r=0}^M \sum_{z=0}^N |s_{c2}(r, z)|^2}}. \quad (2.21)$$

For completely coherent scatterer fields from both antennae, (2.19) will give an absolute value of $|\gamma| = 1$ while $|\gamma| = 0$ indicates that the scatterer fields seen from the two antennae are entirely independent. An average value close to 1 is desirable for an interferogram of high quality. This may be better illustrated by the fact that we may define the correlation as a ratio of SNR via [106]

$$|\gamma| = \frac{\text{SNR}}{\text{SNR} + 1} \quad (2.22)$$

2.5.3 Experimental Data

ATI for GMTI was the starting point for this dissertation. Before even thinking about mmW SAR capabilities, an early test scenario for moving targets in SAR imagery was worked out. On November 13, 2000, an ATI experiment with the X-band SAR AeS-1 [107] from the former AeroSensing GmbH was carried out on and near the airfield of Emmen, Switzerland. The primary aim of the experiment was the collection and analysis of GMTI data. For this, the use of five cars was planned, moving on the airfield runway and being equipped with GPS for position and velocity measurements. Very important aspects of the experiment were the basic gathering of experiences with GMTI setups and data handling for follow-up experiments.

AeS-1 was used in ATI mode for the experiment with two SAR antennas and the following system parameters: a carrier frequency of $f_c = 9.55$ GHz, a PRF of 2000 Hz, a chirped pulse bandwidth of $W = 400$ MHz, HH polarization, an off-nadir angle of $\theta = 45^\circ$, and an image resolution 0.4 m. Unfortunately, weather conditions with stormy winds during the experiment did not allow for a successful completion of the GMTI of the five moving cars. The storm caused heading, pitch, and roll changes of the airplane of up to 5° in less than 10 s time. However, sufficient-quality images could be acquired from the nearby river Reuss. Fig. 2.10 shows a focused SAR amplitude image of a 3 by 3 km² area of the river Reuss near Emmen. Also visible is the highway parallel to the river and some structures and buildings below. According to the theoretical explanations of the previous Chapter 2.5.2 one may refer to this image as s_{c1} , designating it as the master channel of the ATI SAR.

In Fig. 2.11, the phase of the raw interferogram i according to (2.15) is shown. Clearly visible is the fringe pattern caused by the flat earth as described in (2.17) and illustrated in Fig. 2.9. According to the theory, such a fringe pattern only appears when there is a spatial baseline B_S in the interferogram. An analysis of flight track data from GPS and INS (inertial navigation system) resulted in a spatial baseline of roughly 6 cm.

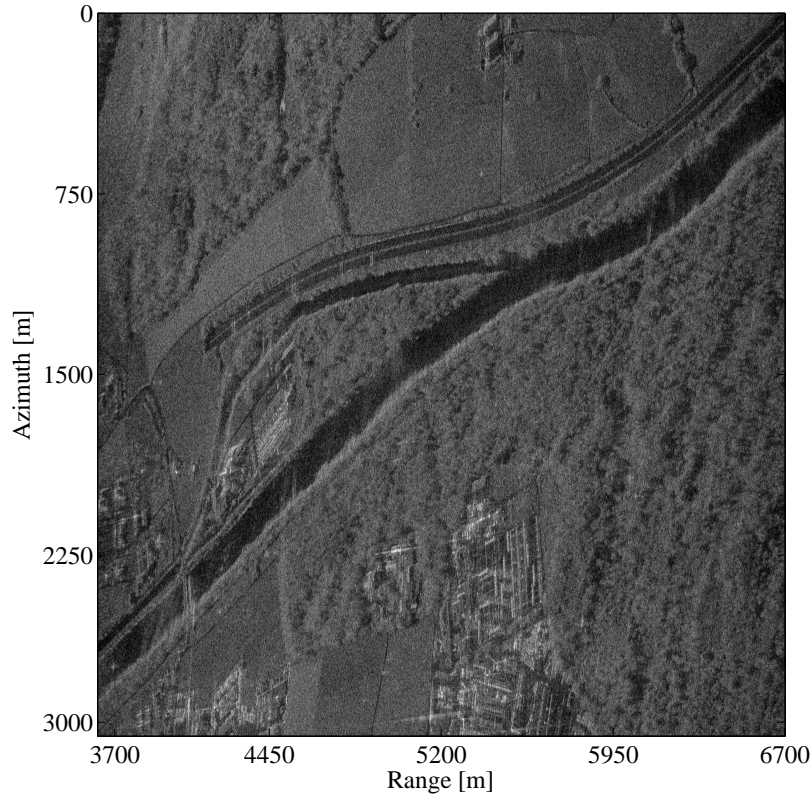


Fig. 2.10: Amplitude image of the river Reuss.

In Fig. 2.12, the fringe pattern from the flat earth has been removed. The residual phase variations clearly show the river Reuss. Also visible are pointlike distortions that probably originate from bad data quality due to the stormy weather conditions. Nonetheless, the figure shows a flat terrain ($\Delta\phi = 0$) and a movement of the river. For a numerical analysis, of the flow velocity, we need the temporal baseline calculated from the sensor velocity $v_s = 110$ m/s and the distance between the two ATI antennas of 0.6 m. B_T is then $5.5 \mu\text{s}$. The radial target velocity is derived from the phase values of the interferogram as [108]

$$\hat{v} = \overline{\Delta\phi} \cdot \frac{\lambda}{2\pi B_T} \quad (2.23)$$

where $\overline{\Delta\phi}$ is the average interferometric phase of a target. To receive a reliable value $\overline{\Delta\phi}$ from the river Reuss, a noise-reducing multilooking (phase averaging and resolution reduction by a factor of 10) was performed in zoomed area of interest as shown in Fig. 2.13(a). A phase map of Fig. 2.13(a) shows the distribution of the phases of the interferogram in Fig. 2.13(b). As expected, most values $\Delta\phi(r, z)$ are located around 0, representing the

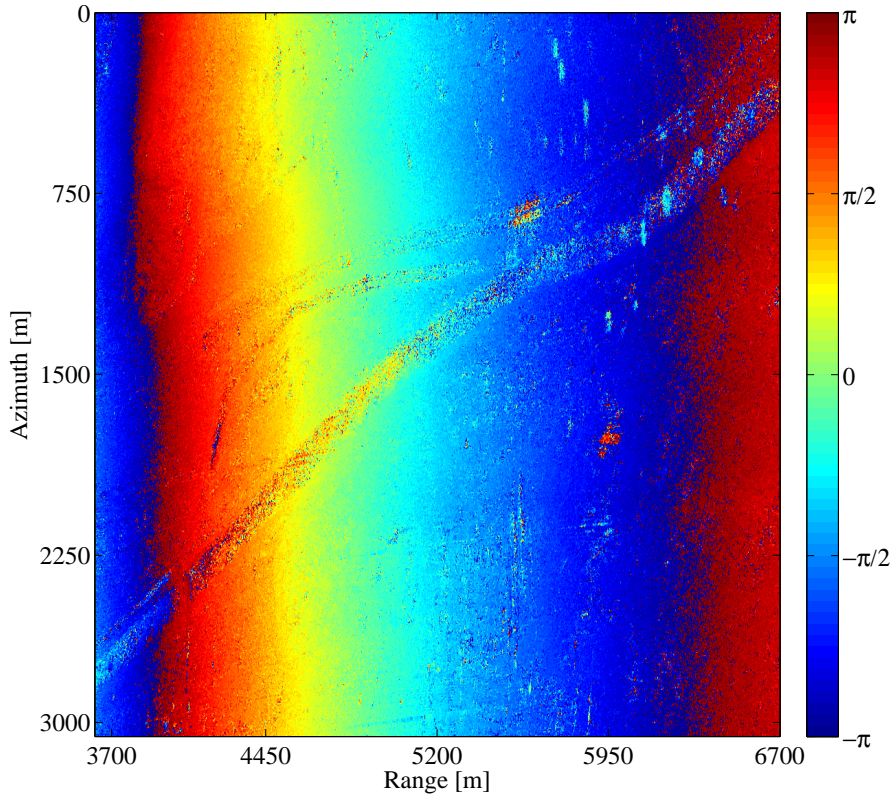


Fig. 2.11: Raw along-track interferogram of the river Reuss.

static ground. The values of the flowing water in the river Reuss ($\Delta\phi \approx 0$) are distributed cloudlike between 0 and $\pi/3$ with a mean value at $\pi/6$. Through the analysis of the phase map in Fig. 2.13(b), a numerical evaluation of the river flow velocity with (2.23) and $\overline{\Delta\phi} = \pi/6$ becomes possible and results in $\hat{v} = 0.48$ m/s radial to the radar. With a sensor off-nadir angle of 45° toward this section of the river and an angle between river bed and sensor azimuth that is very close to 45° we get an absolute current speed of 0.96 m/s on the ground.

To confirm measured values, the Department of Construction, Environment and Commerce of the canton Lucerne was contacted. Their scientists could provide a water flow velocity value of 1.15 m/s measured during an experiment on May 5, 1993, that included the coloring of river water between Lucerne and Emmen. Additionally, they maintain water volume measurements on a daily basis. For the day of their experiment, 109 m³/s where flowing down the river Reuss at Emmen. For the day of the ATI SAR experiment on November 13, 2000, 70.3 m³/s where measured. A linear approximation of the flow velocity would result in a current of 0.74 m/s. Since volume and current speed obviously do

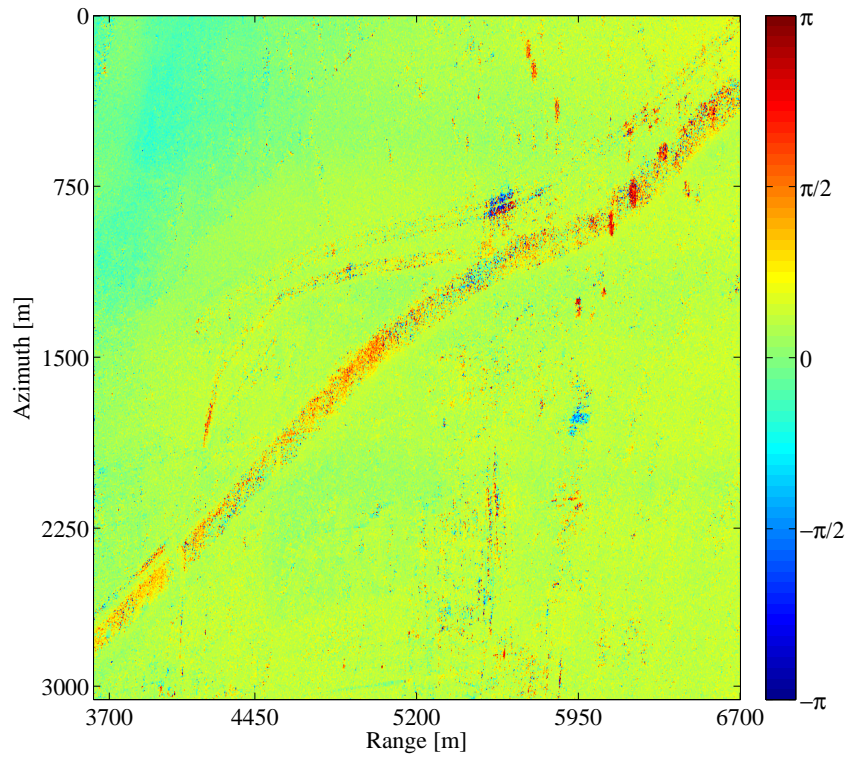


Fig. 2.12: Flattened interferogram of the river Reuss and area of zoom shown in Fig. 2.13.

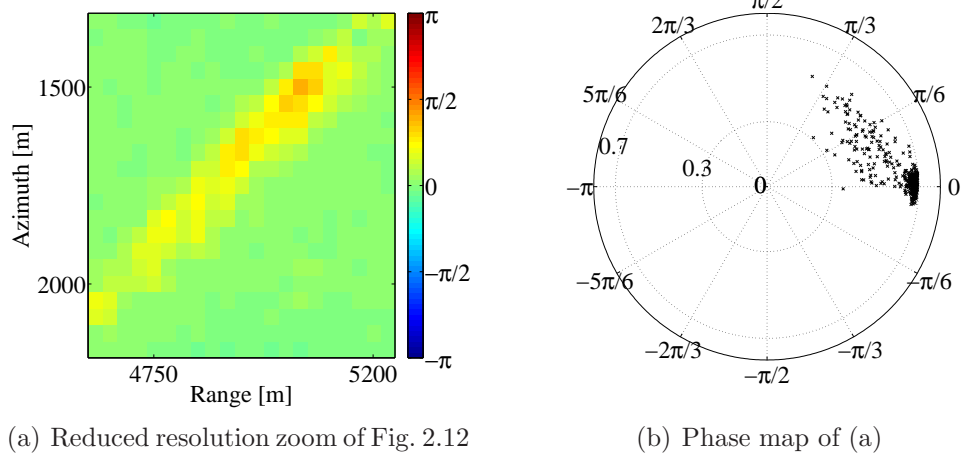


Fig. 2.13: Estimation of $\overline{\Delta\phi}$ over a small and 10-multilooked section of the river Reuss and surrounding area in (a) gives a cloudlike phase distribution between 0 and $\pi/3$ in (b).

not relate linearly, a ATI SAR measurement of 0.96 m/s seems a reasonable value—more exact for the specific location of the measurement than an average between Lucerne and Emmen.

2.5.4 Discussion

There are many issues concerning ATI SAR for GMTI and especially for current measurements. Some aspects are discussed in [45, 53]. One of the main issues is temporal decorrelation of the water surface. For this, a coherence analysis as described earlier in Chapter 2.5.2 gives some insight. In Fig. 2.14, the phase corrected coherence map of the interferogram from Fig. 2.12 is shown. The average image coherence is $|\gamma| = 0.65$. However, for the river Reuss, the coherence is much lower. A lower coherence, then, indicates a lower interferometric phase quality and higher velocity estimation errors. On the other side, the coherence is obviously directly affected by the velocity. A quick and turbulent river like the Reuss in Emmen will always result in temporal decorrelation and

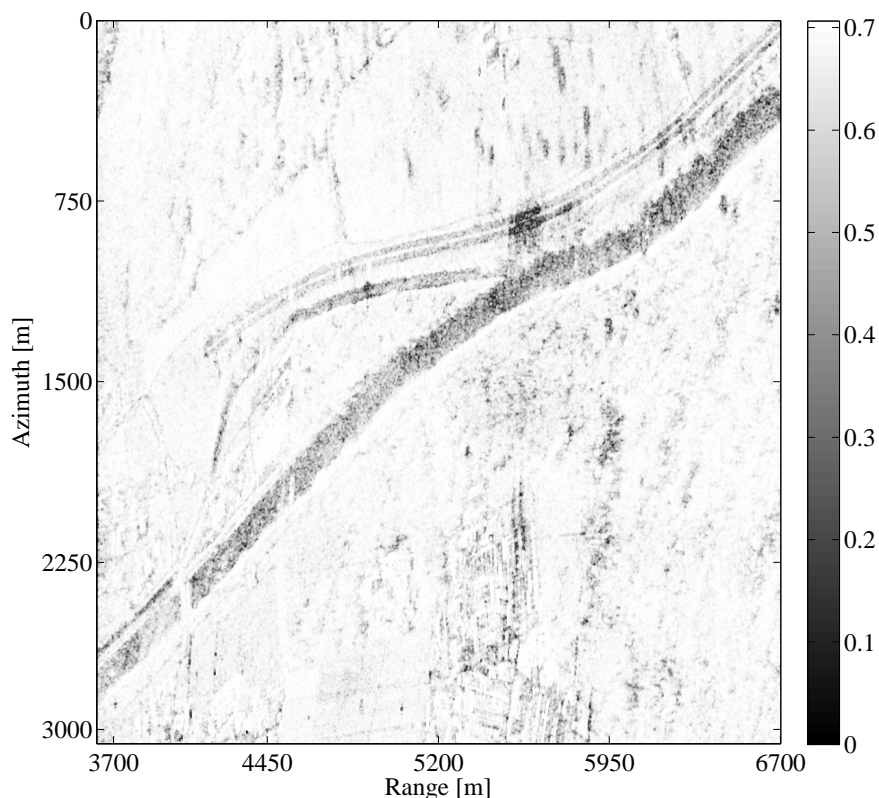


Fig. 2.14: Phase corrected coherence map of the along-track interferogram from Fig. 2.12.

low coherence.

In [108], an extensive analysis of this difficulty of ATI SAR for surface current measurements is given. It investigates the distortion induced into the measurement from the specific properties of moving water surfaces. A conclusion is reached that measurement errors may be significant if an ATI-SAR is used to estimate strong current gradients found in rivers. Furthermore, the analysis talks about the generally unknown topography of the river surface coupled with a cross-track baseline resulting from unintended but inevitable changes in the aircraft attitude and how that produces apparent surface velocity variations. It concludes that these errors must be removed, either by incorporating a digital elevation model or perhaps by measuring the elevation of the river banks using cross-track interferometry as done in [109].

Chapter 3

Target Movement

Before talking about GMTI, it makes sense to discuss and analyze the effects of target movement in SAR. Only once these effects are clear, an exploitation of them becomes possible to indicate targets. In the following, the effects of movement are explained with a two-dimensional SAR system model, and the received signals are analyzed for their characteristics.

3.1 General Effects in SAR Imagery

Generally, a mmW SAR system has some advantages as well as disadvantages when it comes to the imaging of moving targets. Because of the very short wavelength, we have a high signal phase sensitivity for even small target velocities. This effect may be observed as a Doppler shift f_d in the received signal of a target moving with a radial velocity \hat{v} as

$$f_d = \frac{2\hat{v}}{\lambda} \quad (3.1)$$

where λ is the wavelength of the carrier signal. Unfortunately, f_d may easily become aliased when being larger than the limit given by the PRF, resulting in a possibly ambiguous measured target velocity

$$\hat{v} = \frac{(f_d + n \cdot \text{PRF})\lambda}{2} \quad \text{for all } n \in \mathbb{Z}. \quad (3.2)$$

This ambiguity may be resolved by additional information, such as using dual-frequency SAR (see Chapter 4.3).

A direct effect of (3.1) is the displacement d of moving targets in a focused SAR image as described by [13, 30, 54]

$$d = \frac{\hat{v}}{v_s} \cdot R \quad (3.3)$$

where v_s is the SAR platform velocity in azimuth and R the distance to the target. Since R is changing over the radar dwell time T , target displacements may be smeared. The

advantage of a mmW SAR is its generally very small antenna aperture divergence angle in azimuth ϕ_d . This implies that the dwell time T is short for any given target and smearing is reduced.

Furthermore, [30] states range smearing of a moving target over multiple range resolution cells when

$$v_r T \geq \delta_r \quad (3.4)$$

where v_r is the target velocity in range and δ_r is the range resolution. A short dwell time T is again of advantage. However, δ_r may be in the order of centimeters for a high resolution mmW SAR, reducing the advantage of a small value for T .

Another effect is a defocusing of moving targets, depending on azimuth target velocity v_z and range acceleration a_r . As stated in [30], defocusing appears if we have

$$\frac{2\pi}{\lambda R(T)} \left| \left(1 - \frac{v_z}{v_s}\right)^2 - \frac{a_r R_0}{v_s} - 1 \right| (v_s T)^2 \geq \pi \quad (3.5)$$

where R_0 is the range of closest approach to the target. Because λ is small in a mmW SAR, (3.5) may often be true even for small target azimuth velocities v_z or range accelerations a_r .

Regarding (3.3), (3.4), and (3.5), an interesting point is that for a target moving at a constant velocity perpendicular to the sensor track with a velocity vector \mathbf{v} , we seem to have $\hat{v} = |\mathbf{v}|$ while $v_z = 0$ and $a_r = 0$. However, this is only true at R_0 . At all other points in the aperture, we get

$$\hat{v}(T) = |\mathbf{v}| \cdot \cos \varphi(T) \quad (3.6)$$

with the target aspect angle $\varphi(T) \in [-\phi_d, \phi_d]$, where ϕ_d is the antenna aperture divergence angle, and

$$v_z(T) = |\mathbf{v}| \cdot \sin \varphi(T). \quad (3.7)$$

Additionally, because φ changes with T , we have

$$a_r(T) = \frac{d}{dt} v_r(T) = \frac{d}{dt} \left(\cos \varphi(T) \right). \quad (3.8)$$

This means that even for a target moving only perpendicular to the SAR flight track with constant \mathbf{v} , and although we have a very small ϕ_d for mmW SAR, (3.5) may cause a target defocus over the synthetic aperture. Fig. 3.1 illustrates this phenomenon.

For many sensors and applications—and in most publications—the approximation

$$\hat{v} \approx v_r \quad (3.9)$$

is sufficient and reduces the complexity of GMTI. Especially when talking about focused images, an additional radial velocity may confuse the reader. However, to understand concepts of smearing and defocus, the exact notation and a differentiation between the radial velocity \hat{v} and the velocity in range v_r is used in this chapter.

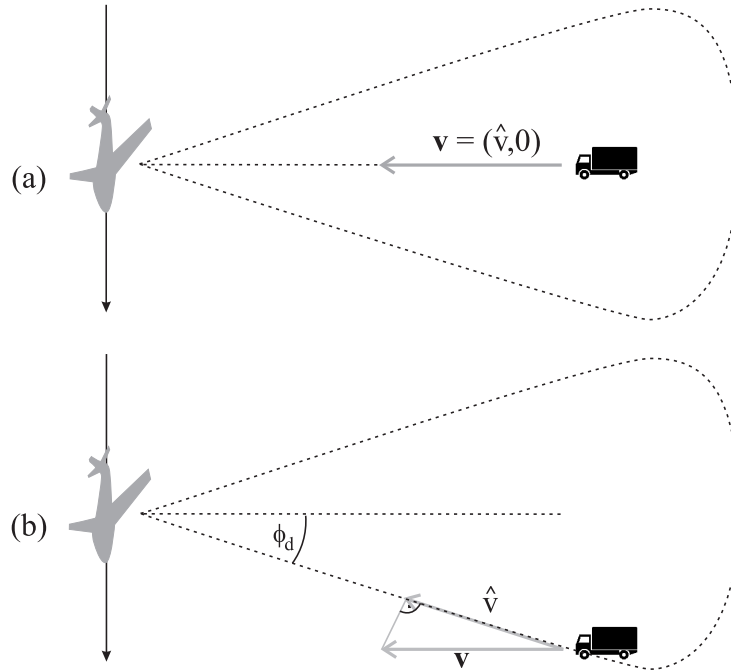


Fig. 3.1: SAR geometry with a target moving perpendicular to the flight track with \mathbf{v} . (a) At beam center, the target velocity is only radial. (b) Out of beam center, the target velocity has a radial component \hat{v} as well as one perpendicular to \hat{v} .

3.2 System Model

The following SAR geometry and system model for static point targets are based on [13]. Because we use them as a foundation to all subsequent considerations, they are explained in some detail here.

To simplify the analysis without loss of generality, we use a purely two-dimensional sensor flight geometry, with the z -coordinate pointing in the flight direction (azimuth) and the r -coordinate pointing right in the radar look direction (range). We assume an airborne stripmap SAR system on a linear flight track and neglect spaceborne data effects of earth rotation and orbit curvature. All image dimensions are given by the target area of interest, the SAR antenna radiation pattern, and the resulting recorded scene as described in Fig. 3.2.

The antenna radiation pattern defines the 3 dB beamwidth of the SAR. We model the signal inside this 3 dB beamwidth through its transfer function, given as

$$H(\omega, r, z - u) = a(\omega, r, z - u) \cdot \exp\left(-2j\frac{\omega}{c}\sqrt{r^2 + (z - u)^2}\right). \quad (3.10)$$

Obviously, the phase $\exp(\cdot)$ as well as the amplitude $a(\cdot)$ depend on the instantaneous signal frequency ω and the relative position between a scatterer at (r, z) and the SAR sensor at $(u, 0)$. c is the speed of light.

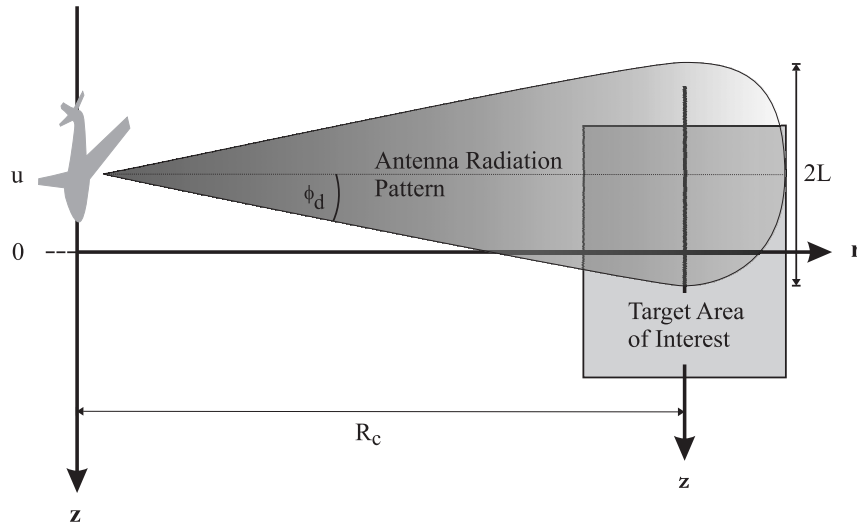


Fig. 3.2: Two-dimensional SAR geometry for the system model used.

The area of validity (3 dB beamwidth) of the antenna is strongly dependent on the type of antenna installed (planar array or curved antenna) and its specifications. For our model, we use a simple pattern defined via the half-beamwidth L with

$$L(r) = r \cdot \tan(\phi_d). \quad (3.11)$$

This implies the knowledge of the size of the antenna aperture angle ϕ_d which is approximated in [13] via the wavelength λ of the carrier frequency and the physical antenna length in azimuth ℓ as

$$\phi_d = \text{asin}\left(\frac{\lambda}{\ell}\right). \quad (3.12)$$

Finally, let R_c be the range to the center of the area of interest.

3.3 Signal Theory

3.3.1 Static Target Returns

After having defined a target geometry, we would like to define a model for the raw data as received by the radar for analysis and simulation. Raw data have the advantage over single look complex focused SAR images in that we hold an additional level of information, namely the unprocessed amplitude and phase of targets useful for a time-frequency analysis.

We start by repeating the definition of the emitted radar signal as a chirped pulse (see Chapter 2.1)

$$p(t) = e^{j(\beta t + \alpha t^2)} \quad (3.13)$$

with a pulse duration of τ_p and a signal bandwidth of $W = 2\alpha\tau_p$. Together with the transfer function from (3.10) and using the stop-and-go approximation (assuming no sensor movement between signal transmission and reception, a reasonable assumption for airborne SAR), we receive an echo $s(t, u)$ at the antenna position $u = v_s T$ from all point targets n at locations

$$\mathbf{Q}_n = \begin{pmatrix} r_n \\ z_n \end{pmatrix} \quad (3.14)$$

given by its Fourier transform

$$\begin{aligned} S(\omega, u) &= P(\omega) \cdot \sum_n A_n \cdot H_n(\omega, r_n, z_n - u) \\ &= P(\omega) \cdot \sum_n A_n \cdot a_n(\omega, r_n, z_n - u) \cdot \exp\left(-2j\frac{\omega}{c}\sqrt{r_n^2 + (z_n - u)^2}\right). \end{aligned} \quad (3.15)$$

While the term A_n is the physical target reflectivity, a_n is the return echo amplitude of a point target n with unit reflectivity. $P(\omega)$ is the Fourier transform of chirp $p(t)$. More exactly, we use the target aspect angle

$$\varphi_n(u) = \text{atan}\left(\frac{z_n - u}{r_n}\right), \quad -\phi_d \leq \varphi_n(u) \leq \phi_d \quad (3.16)$$

to define the signal amplitude of the n th target as a raised cosine

$$a_n(\omega, r_n, z_n - u) = \frac{1}{2} + \frac{1}{2} \cos\left(\frac{\pi\varphi_n(u)}{\phi_d(\omega)}\right). \quad (3.17)$$

We note that the antenna aperture angle is given depending on ω which may be important for wideband systems. Instead of (3.12) we may set $\phi_d(\omega) = \text{asin}\left(\frac{2\pi c}{\omega \ell}\right)$. With $u \in [z_n - L_n, z_n + L_n]$ and $L_n = r_n \tan(\phi_d)$ we receive a target amplitude different from zero within the synthetic aperture of the radar.

Finally, we shift our received raw SAR signal to the baseband with

$$s_0(t, u) = s(t, u) \cdot e^{-j\omega_c t}. \quad (3.18)$$

3.3.2 Examples

The presented system model and signal theory allow the simulation of static point targets. To be congruent with experimental data and analyses to be presented in Chapter 5, the radar system parameters are chosen for the simulation results according to Table 3.1. They correspond to a possible mode of the experimental mmW SAR sensor MEMPHIS (see Appendix A). Being experimental, MEMPHIS is normally carried on a very large and stable platform, a C-160 Transall, that offers the flexible deployment and robust design needed for such a system.

Table 3.1: IMPORTANT RADAR SYSTEM PARAMETERS FOR MMW SIMULATIONS ACCORDING TO THE STANDARD W-BAND MODE OF MEMPHIS.

f_c	=	94 GHz	→	$\lambda = 3.19$ mm (W-band)
W	=	200 MHz	→	$\delta_r = 0.75$ m
τ_p	=	1.2 μ s		
PRF	=	1700 Hz		
v_s	=	75 m/s		
ℓ	=	0.12 m	→	$\delta_z \approx 0.06$ m
R_c	=	780 m		

The system parameters are valid for all subsequent simulations presented in this chapter as well as for the real data experiments with MEMPHIS (for simulations with X-band system parameters see [110]). The focused SAR images have been processed with the extended chirp scaling algorithm [21]. All MEMPHIS data were recorded with a sensor off-nadir angle of $\theta = 70^\circ$.

The experiment was carried in Emmen, central Switzerland in November 2005. All data collected show the area of and around the airfield of Emmen.

Fig. 3.3 shows in (a) the pulse compressed echoes of a simulation with the above system parameters. Five point targets are simulated, four of them forming a square of edge length 20 m and the fifth one in the image center. As the targets are not yet focused in azimuth,

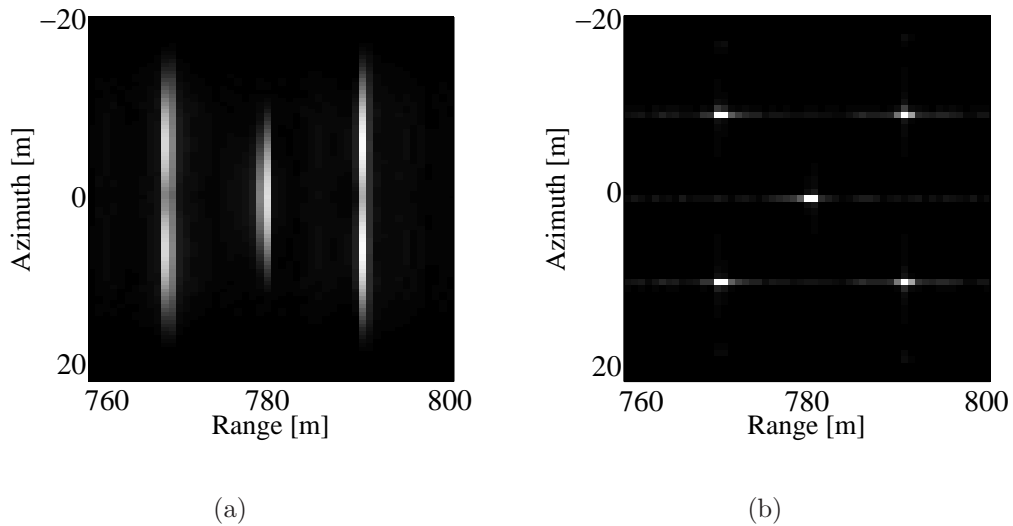


Fig. 3.3: (a) Pulse-compressed SAR intensity image and (b) the equivalent fully focused intensity image of a simulated static point target at 94 GHz. Image resolution is 0.75 m.

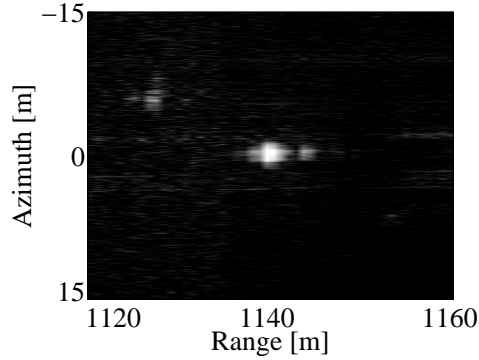


Fig. 3.4: Focused SAR image of a static corner reflector at image center.

their exact position is difficult to read from the image. In Fig. 3.3(b), azimuth compression has been performed, now showing focused point targets.

Similarly, a corner reflector in real data is shown in the center of Fig. 3.4. The reflector was standing on a tarmac to keep the clutter and noise level around it low.

3.4 Time-Frequency Analysis

The Fourier transform is a common method to analyze radar signal waveforms in the frequency domain. However, with the Fourier transform, we lose all information of time. A joint time-frequency analysis is needed to extract time-varying information in the spectrum of a radar signal.

A good bilinear time-frequency transform that belongs to Cohen's class [111] is the Wigner-Ville distribution (WVD). As such, it is an energy distribution in contrast to linear time-frequency representations which decompose the signal into elementary components (atomic distributions). The WVD of a signal $s(t)$ is defined as the Fourier transform of the time-dependent autocorrelation function

$$W(t, \omega) = \int_{-\infty}^{\infty} s(t + t'/2) s^*(t - t'/2) \cdot e^{-j\omega t'} dt'. \quad (3.19)$$

This definition requires the knowledge of the quantity

$$s(t + t'/2) s^*(t - t'/2), \quad -\infty \leq t' \leq \infty \quad (3.20)$$

which is not the case for a sampled radar signal. A window filter $h(t)$, such as a Hamming window in the time domain, solves this problem and results in the pseudo-WVD. In order to reduce the cross-term interference problem of the WVD we add a smoothing function $g(t)$ (e.g. a second Hamming window) and obtain the smoothed pseudo-WVD [112]

$$SW(t, \omega) = \int_{-\infty}^{\infty} h(t') \int_{-\infty}^{\infty} g(r - t) \cdot s(t + t'/2) s^*(t - t'/2) dx \cdot e^{-j\omega t'} dt'. \quad (3.21)$$

This distribution is a compromise between joint time-frequency resolution and the level of interference terms: the more one smoothes in time and/or frequency, the poorer the resolution in time and/or frequency [112].

In SAR, the echoes of successively transmitted pulses show a phase shift varying with azimuth time T as a function of the relative motion between the radar and each backscatterer. Each point on the ground reflects a Doppler shift proportional to the projection of the radar velocity v_s along the line of sight by the angle $\varphi(T)$ as (see Chapter 2.1.1.2)

$$f_d(T) = \frac{v_s \omega_c \sin(\varphi(T))}{\pi c}. \quad (3.22)$$

This is basically the same relation as given in (3.1) with the difference that here we have the Doppler history of a static target and in (3.1) a superimposed Doppler frequency from target movement. For small mmW antenna apertures $\varphi(T)$, $f_d(T)$ may be assumed to be linear.

This Doppler history over time as in (3.22) can be made clearly visible with a time-frequency analysis. Additionally, Doppler shifts from moving targets as well as very small variations in target Doppler—so-called micro-Doppler phenomena [113, 114]—may be observed in detail with the smoothed pseudo-WVD.

For simulated data, the smoothed pseudo-WVD is well suited. Real SAR data, however, is often corrupted by noise, and micro-Doppler effects may not be observed in either the time domain or the frequency domain. For this, atomic decompositions, such as the Gabor transform [111, 112], are very useful because—unlike an energy distribution like the WVD—they are localized in both the time and frequency domain. Therefore, the Gabor

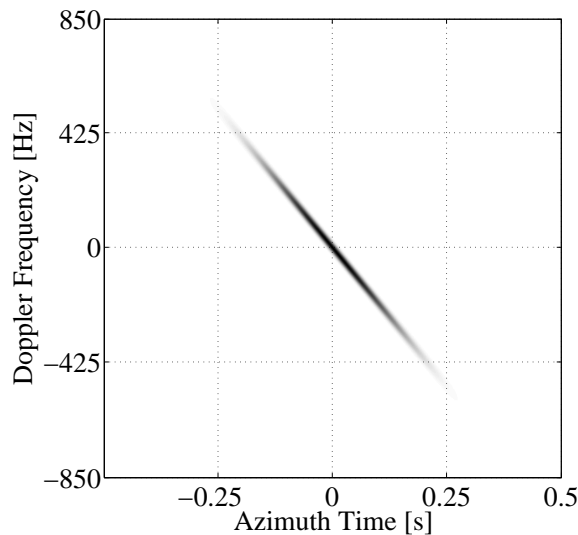


Fig. 3.5: Time-frequency representation of the pulse compressed data from a simulated 94 GHz SAR point target as in Fig. 3.3.

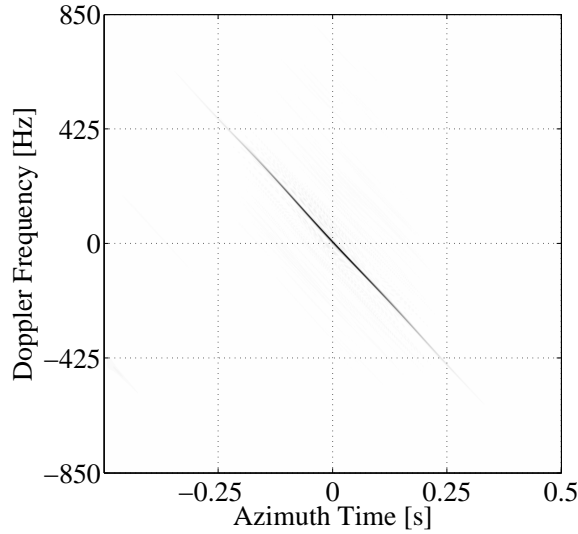


Fig. 3.6: Time-frequency representation of the pulse compressed SAR data of the static corner reflector from Fig. 3.4.

transform is often used to visualize micro-Doppler effects [113], and we did additionally analyze all experimental targets with the Gabor transform. Since both representations showed congruent results and to make a direct comparison between simulations and real data possible, we confined ourselves to presenting the ones from the smoothed pseudo-WVD in the following.

To start with, the simulated static point target at the center of Fig. 3.3 is represented in a smoothed pseudo-WVD in Fig. 3.5. At the same time, Fig. 3.6 shows the smoothed pseudo-WVD of the range compressed signals from the reflector in real SAR data of Fig. 3.4¹.

For both, the simulated and the real time-frequency representation, it may be seen that a target's signature is visible with the SAR sensor for approximately 0.5 s. This agrees with the system parameters given in Table 3.1 since the dwell time in which a point target is illuminated is given with (3.12) by

$$T = \frac{2r}{v_s} \cdot \tan \left(\arcsin \left(\frac{\lambda}{\ell} \right) \right). \quad (3.23)$$

At the same time, the time-frequency representations in Figs. 3.5 and 3.6 confirm the SAR Doppler history of (3.22) for a static point target.

¹The Doppler spectrum appears centered in the image because we included a correction of the Doppler centroid in the analysis to make image interpretation easier and more comparable to simulation results where we always had a Doppler centroid value of zero.

3.5 Constant Target Movement

The system model presented in Chapter 3.2 offers the opportunity to define target motion quite easily by declaring the target position to be a function of the slow time or sensor azimuth time

$$T = u/v_s. \quad (3.24)$$

We define the position $\mathbf{Q}_n(T)$ of target n at slow time T to be

$$\mathbf{Q}_n(T) = \begin{pmatrix} r_n(T) \\ z_n(T) \end{pmatrix}. \quad (3.25)$$

It is well known that a moving target may be smeared, defocused and displaced in azimuth in a focused SAR image [30]. This displacement is due to the Doppler shift given in (3.1) and depending on a radial target velocity \hat{v} . It may be rewritten for a target n as

$$f_{d_n}(T) = \frac{\omega_c \hat{v}_n(T)}{\pi c} \quad (3.26)$$

with the instantaneous radial target speed

$$\hat{v}_n(T) = \frac{d\mathbf{Q}_n(T)}{dT} \cdot \frac{\mathbf{r}_n(T)}{|\mathbf{r}_n(T)|} \quad (3.27)$$

where $\mathbf{r}_n(T)$ is the radial look vector. With the target velocity vector

$$\mathbf{v}_n(t) = \begin{pmatrix} v_{r_n}(T) \\ v_{z_n}(T) \end{pmatrix} \quad (3.28)$$

we get

$$\hat{v}_n(T) = v_{z_n}(T) \sin(\varphi_n(T)) + v_{r_n}(T) \cos(\varphi_n(T)) \quad (3.29)$$

using the definition of $\varphi_n(u)$ in (3.16) and the relation between u and T in (3.24). Because of the target movement and change of variables from azimuth position u to slow time T , the target aspect angle $\varphi_n(u)$ defined in (3.16) must be adapted to

$$\varphi_n(T) = \text{atan} \left(\frac{z_n - Tv_s + Tv_{z_n}}{r_n + Tv_{r_n}} \right). \quad (3.30)$$

The Doppler shift of (3.26) is superimposed on the basebanded radar signal as

$$s_{0_n}(t, T) = s_n(t, T) \cdot e^{-j(\omega_c + 2\pi f_{d_n}(T))t} \quad (3.31)$$

where $s_n(t, T)$ is the echo signal of target n . The amount of target displacement in azimuth in the focused SAR image is then given as (see (3.3))

$$d_n(T) = -\frac{\hat{v}_n(T)}{v_s} |\mathbf{r}_n(T)|. \quad (3.32)$$

When limiting the above theory to constant target movements, one gets a position of target n at sensor position u defined as

$$\mathbf{Q}_n(u) = \begin{pmatrix} z_n - u + v_{z_n}u/v_s \\ r_n + v_{r_n}u/v_s \end{pmatrix}. \quad (3.33)$$

When inserting (3.33) into (3.15) we get an echo signal at the antenna from all targets n

$$\begin{aligned} S(\omega, u) &= P(\omega) \cdot \sum_n a_n(\omega, z_n - u, r_n) \cdot A_n \\ &\cdot \exp\left(\frac{-2j\omega}{c} \sqrt{\left(z_n - u + \frac{uv_{z_n}}{v_s}\right)^2 + \left(r_n + \frac{uv_{r_n}}{v_s}\right)^2}\right). \end{aligned} \quad (3.34)$$

Because of the target movement, the target aspect angle $\varphi_n(u)$ adapted in (3.30) must be further changed to

$$\varphi_n(u) = \text{atan}\left(\frac{z_n - u + \frac{uv_{z_n}}{v_s}}{r_n + \frac{uv_{r_n}}{v_s}}\right) = \text{atan}\left(\frac{v_s(z_n - u) + uv_{z_n}}{v_sr_n + uv_{r_n}}\right). \quad (3.35)$$

Secondly, a moving target experiences a Doppler shift [30] that is dependent on the radial target velocity $\hat{v}_n(u)$:

$$f_{d_n}(u) = -\frac{\omega_c v_{r_n}(u)}{\pi c} \quad (3.36)$$

with the instantaneous radial target velocity given by

$$\hat{v}_n(u) = v_{r_n} \cos(\varphi_n(u)) + v_{z_n} \sin(\varphi_n(u)). \quad (3.37)$$

(3.36) is negative because we define a positive radial velocity to point away from the radar (according to the r -coordinate of the geometry).

Finally, we may combine the operations of baseband conversion and Doppler shift correction for each target n as

$$s_{0_n}(t, u) = s_n(t, u) \cdot e^{-j(\omega_c + 2\pi f_{d_n})t}. \quad (3.38)$$

3.5.1 Visual Effects

In Fig. 3.7, two different constant target movements are shown. The same SAR system and geometry parameters as for static targets in Chapter 3.3.2 are used and five point targets are simulated with the one difference that our center target is now moving. If the movement is only in range as in Fig. 3.7(a), where $v_r = 1$ m/s and $v_z = 0$ m/s, one gets a displacement in z of exactly -10.4 m according to (3.3) as the main visible effect in the focused SAR image. The very small white dot at the bottom of the image at almost 20 m is caused by aliasing in the Doppler spectrum, an effect that is discussed in detail below.

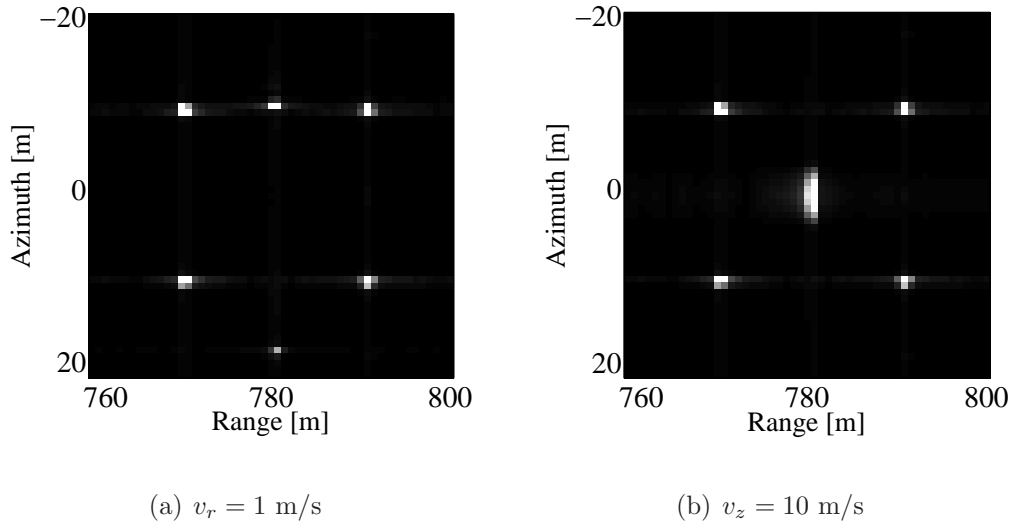


Fig. 3.7: Focused SAR scenes with a constantly moving center target. In (a), the target is moving right with $v_r = 1$ m/s, causing a displacement in azimuth. (b) shows a smeared target moving down with $v_z = 10$ m/s.

If the movement is tangential as in Fig. 3.7(b) ($v_r = 0$ m/s and $v_z = 10$ m/s), one gets mainly a smearing effect, some target defocus, but no displacement. Obviously, a combination of range and azimuth movement would result in smearing as well as displacement.

For target velocities in range, smearing and defocus is extremely small because of a slow movement and small radar dwell time. The displacement, however, is large due to the large Doppler shift caused by the high carrier frequency of mmW SAR. A velocity of only 2.71 m/s will result in a Doppler shift that is equal to the simulation PRF of 1700 Hz given by (3.2). This causes some effects that must be considered when dealing with moving targets in SAR imagery; they may be summarized as Doppler ambiguities and blind speeds [10], and they appear because of a limited PRF. They are illustrated in Fig. 3.8. When the Doppler shift of a target due to its radial velocity approaches half the PRF because of a large velocity or small PRF, the target is displaced in negative as well as positive direction. In Fig. 3.8(a), a center target with a velocity in range of $v_r = 1.35$ m/s is simulated, resulting in a Doppler shift of exactly half the PRF and a displacement in azimuth of ± 14.0 m.

If a positive target velocity in range causes a Doppler shift that is above half the PRF, the movement becomes ambiguous in the SAR—it might just as well be a negative velocity. If a Doppler shift reaches the PRF, it is aliased as 0 Hz, and we do not get a displacement at all. This is simulated in Fig. 3.8(b). The only indication of a velocity in range in such a case may be target smearing which becomes more prominent at higher velocities.

The general effect of Doppler shift aliasing is illustrated in Fig. 3.9 where a target is moving with a velocity in range that causes the Doppler shift to be aliased five times in the spectrum. In (a), the resulting aliased speed is $v_r = 1$ m/s as in Fig. 3.7(a). However,

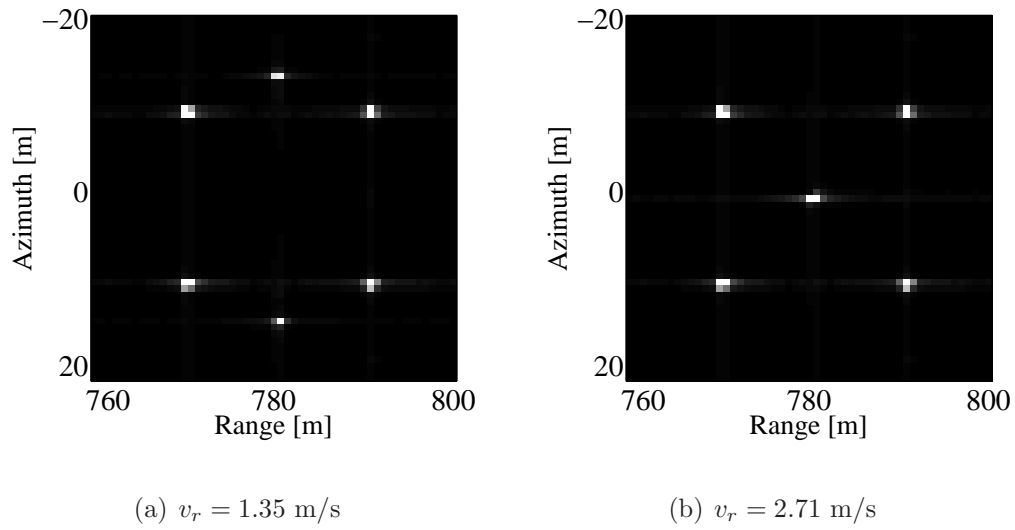


Fig. 3.8: A target velocity in range that causes a Doppler shift of $\text{PRF}/2$ in the data results in an ambiguous target displacement in (a) and a Doppler shift equal to the PRF in a blind target speed without a displacement (b).

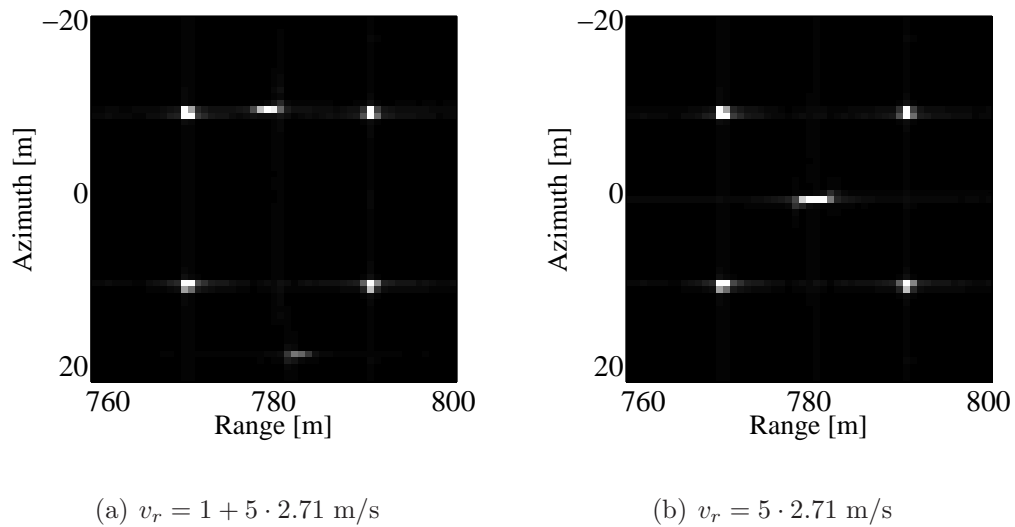


Fig. 3.9: A fast moving target in range causes multiple Doppler ambiguities, a displacement in azimuth, and smearing over many range bins as seen in (a) or, if the target moves at a blind speed, only smearing and no displacement is recognizable (b).

the target is smeared over multiple range bins during the radar dwell time, indicating a much higher speed. In (b), the resulting aliased speed is a blind velocity as in Fig. 3.8(b). Again, smearing over multiple range bins gives an indication to the high target speed.

The effect of ambiguous velocities, shown in Fig. 3.8(a) with a velocity in range that is aliased five times in the Doppler spectrum, is also detectable in Fig. 3.7(a) and—in

extremis—in Fig. 3.9(a) at the bottom of the images. There, a weak but clearly visible signature stemming from the moving target is visible. The cause is that v_r is not equal to \hat{v} (see Chapter 3.1). In fact, the radial velocity responsible for the displacement effect is highest at large target aspect angles. If it is larger than the unambiguous velocity, the target is focused at two positions in the image.

For a discussion of real data examples, the reader is referred to Chapter 5.

3.5.2 Time-Frequency Analysis

The displacement and smearing effects for targets moving with a constant velocity as discussed above may be further illustrated by a time-frequency representation of the range compressed target signatures. In Fig. 3.10, the smoothed pseudo-WVD is given for four of the target movements presented in Figs. 3.7 and 3.9. A comparison of them with the time-frequency representation of a static point target in Fig. 3.5 shows the following differences and phenomena.

In Fig. 3.10(a), a target is moving away from the radar at $v_r = 1$ m/s. The direct effect is a shift of the Doppler spectrum into the negative frequency domain resulting in a target shift in the focused data. A small part of the Doppler is even aliased and is visible in the highly positive frequency domain. This explains the second and weak target at the bottom of Fig. 3.7(a).

In Fig. 3.10(b), there is no target movement in range, but one in azimuth with $v_z = 10$ m/s equal to the situation in Fig. 3.7(b). The result in the smoothed pseudo-WVD is a slope of the Doppler history very slightly different from the one of a static point target in Fig. 3.5. A compression algorithm for static targets will smear the signature of this target moving parallel to the SAR sensor in azimuth. A second effect is the longer dwell time of the radar because of this parallel movement, increasing the smearing further.

Fig. 3.10(c) shows the high blind target velocity in range of Fig. 3.9(b) with a Doppler shift that is aliased five times in the spectrum. The target slope as well as its frequency position in the smoothed pseudo-WVD is correct. However, because the target moves over multiple range bins during the dwell time and the time-frequency plot shows only information from one range bin, the target signature is lost completely after about half the normal dwell time.

Finally, in Fig. 3.10(d), a fast moving target in range is seen to have a shift in the Doppler frequency just as the one in Fig. 3.10(a) and also a signature that is lost after half the dwell time as the one in Fig. 3.10(c). (The time domain data for this distribution was shown in Fig. 3.9(b).)

These examples show that there are many possibilities to discover moving targets in single channel SAR data through an analysis of their time-frequency distribution. Even blind speeds may be detected. However, the limiting difficulty that does not allow this technique to be applied efficiently over large scenes is the removal of clutter signals. It may be achieved with traditional space-time adaptive processing [78].

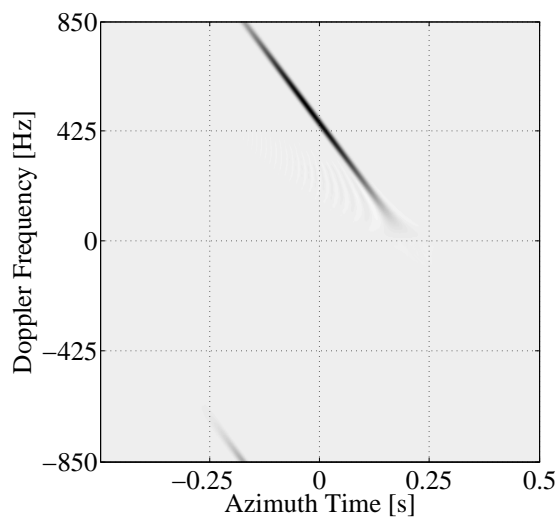
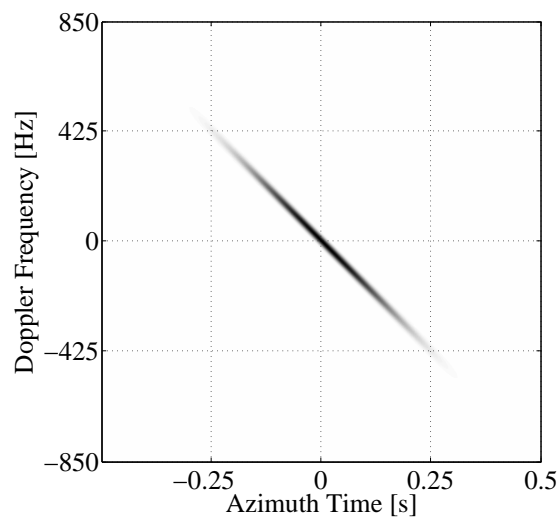
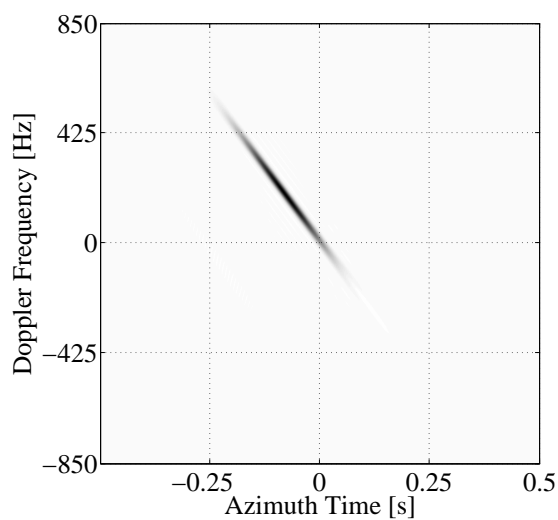
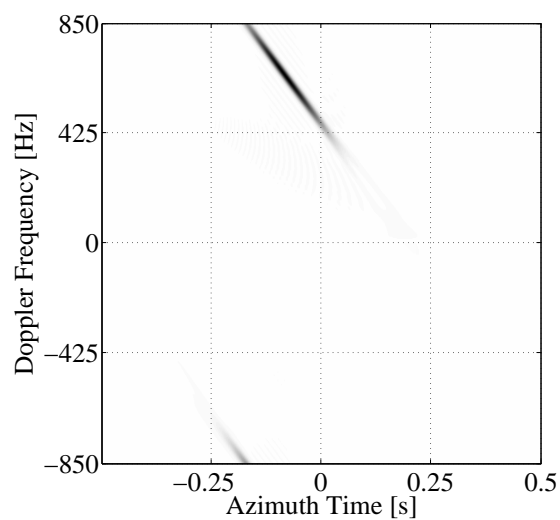
(a) $v_r = 1$ m/s(b) $v_z = 10$ m/s(c) $v_r = 5 \cdot 2.71$ m/s(d) $v_r = 1 + 5 \cdot 2.71$ m/s

Fig. 3.10: Time-Frequency representation (WVD) of the four target movements shown in Figs. 3.7 and 3.9

3.6 Target Acceleration

When considering target acceleration in SAR, one may simply add an acceleration vector $\mathbf{a}_n = (a_{r_n}, a_{z_n})$ for target n to the extended system model of the previous Chapter 3.5. One gets an instantaneous target position

$$\mathbf{Q}_n(u) = \begin{pmatrix} r_n + \frac{u}{v_s} \left(v_{r_n} + \frac{u}{2v_s} a_{r_n} \right) \\ z_n - u + \frac{u}{v_s} \left(v_{z_n} + \frac{u}{2v_s} a_{z_n} \right) \end{pmatrix}. \quad (3.39)$$

Noteworthy is that this model even allows for velocity inversion of direction in that it allows the definition of a constant acceleration while setting the constant velocity terms (v_{r_n}, v_{z_n}) equal to zero. This means that a target accelerates from a negative velocity to one of zero at sensor position u and a positive one afterwards.

From (3.15) and (3.39) we receive the echo signal at the antenna for all targets n with a constant velocity \mathbf{v}_n and acceleration \mathbf{a}_n as

$$S(\omega, u) = P(\omega) \cdot \sum_n a_n(\omega, r_n, z_n - u) \cdot A_n \cdot \exp \left(\frac{-2j\omega}{c} \sqrt{\left(r_n + \frac{u}{v_s} \left(v_{r_n} + \frac{u}{2v_s} a_{r_n} \right) \right)^2 + \left(z_n - u + \frac{u}{v_s} \left(v_{z_n} + \frac{u}{2v_s} a_{z_n} \right) \right)^2} \right) \quad (3.40)$$

and the target aspect angle is given as

$$\varphi_n(u) = \text{atan} \left(\frac{z_n - u + \frac{u}{v_s} \left(v_{z_n} + \frac{u}{2v_s} a_{z_n} \right)}{r_n + \frac{u}{v_s} \left(v_{r_n} + \frac{u}{2v_s} a_{r_n} \right)} \right). \quad (3.41)$$

As in Chapter 3.5, we must consider the Doppler shift of (3.1), dependent on the radial target velocity. However, this time we have an instantaneous radial velocity that depends additionally on the acceleration of a target

$$\hat{v}_n(u) = \left(v_{r_n} + \frac{u}{v_s} a_{r_n} \right) \cos(\varphi_n(u)) + \left(v_{z_n} + \frac{u}{v_s} a_{z_n} \right) \sin(\varphi_n(u)). \quad (3.42)$$

3.6.1 Visual Effects

Fig. 3.11 shows the main effects to be expected from the system model of accelerating targets. In (a), a simulated point target is given, accelerating with 1 m/s^2 in range and an instantaneous velocity of 1 m/s at $u = 0$. (b) shows the situation for an azimuth acceleration of 1.0 m/s^2 and an instantaneous velocity at $u = 0$ of 10 m/s . Hence, the situation at $u = 0$ is equal to the one given for the examples with a constant velocity in Fig. 3.7. However, because of a non-constant velocity in range, the moving target in (a)

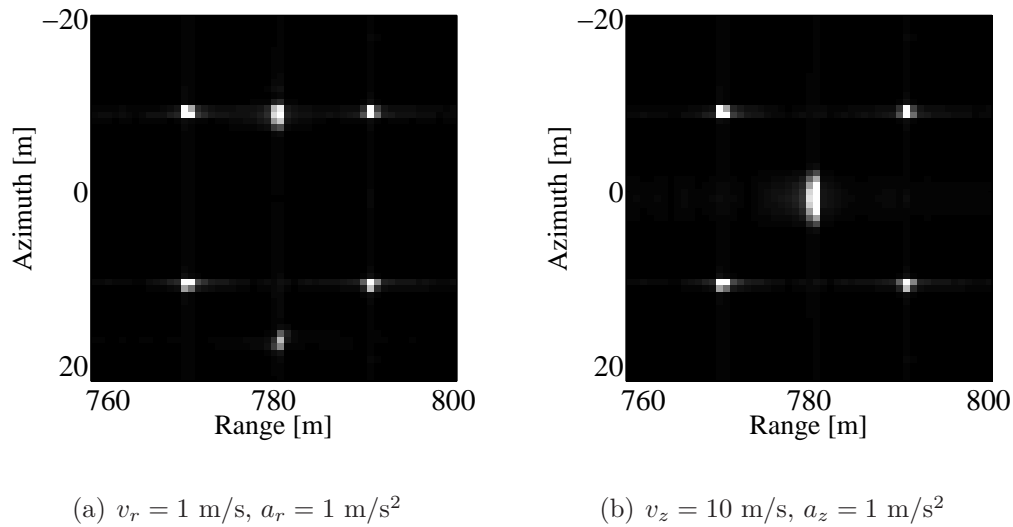


Fig. 3.11: SAR scenes with five point targets, including an accelerating center target. In (a), the acceleration is in range with instantaneous velocities from about 0.8 to 1.2 m/s. In (b), the acceleration is in azimuth with instantaneous velocities from about 9.8 to 10.2 m/s.

gets displaced over a wider area in azimuth, looking like a smeared target. (b) looks very similar to Fig. 3.7(b)—with a constant azimuth movement—because the absolute target drift tangential to the radar is almost identical in both situations; the acceleration causes an increased smearing of less than one meter in azimuth.

3.6.2 Time-Frequency Analysis

The differences in a time-frequency analysis with the smoothed pseudo-WVD between a constant target velocity and one including an acceleration of 1 m/s^2 as in Fig. 3.11 are small if visible at all. Fig. 3.12 shows the resulting plots in (a) for an acceleration in range and in (b) for one in azimuth. From a theoretical point of view we expect the range acceleration of a target to cause a shift in the Doppler history that is non-uniform. In Fig. 3.12(a), one may guess that the ambiguous part of the target spectrum close to half the PRF at -850 Hz is larger than for a target with constant range velocity as in Fig. 3.10(a). Generally, differences are very small and not obvious.

Even less distinct is the time-frequency representation of a target accelerating in azimuth with 1 m/s^2 in Fig. 3.12(b). Through the acceleration, the spectrum of the target is not completely centered at 0 Hz . However, variances in parallel target speed of less than 0.5 m/s are hard to discern when considering the SAR platform velocity of 75 m/s and sensor dwell time of 0.5 s . They cause displacement effects in the decimeter range.

Hence, target acceleration normally plays a minor part considering moving targets in SAR and GMTI algorithms. A close examination of the effects is given in [65, 115].

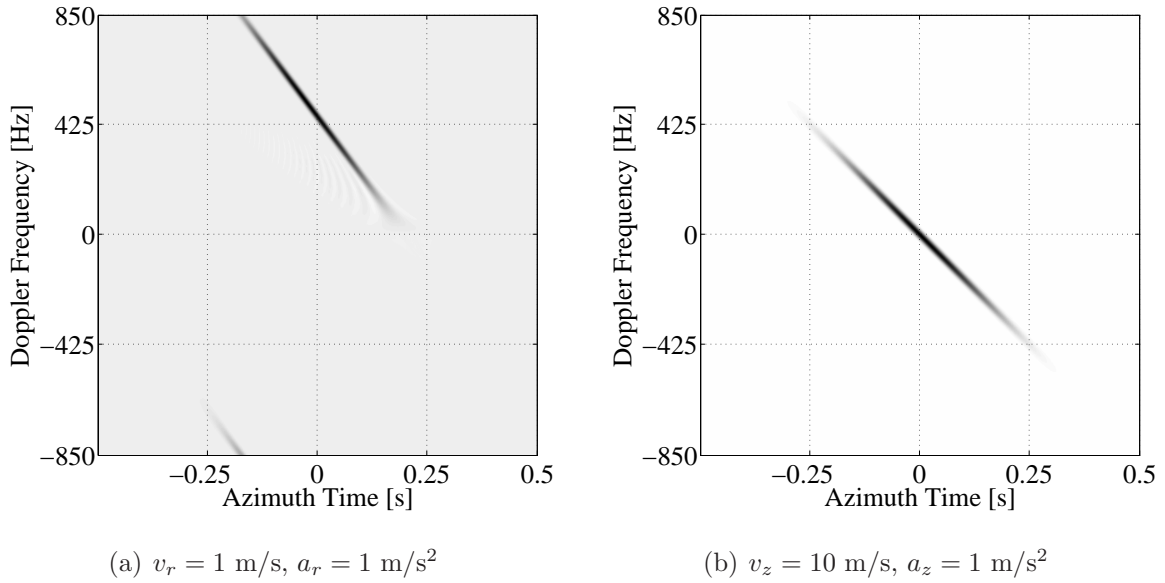


Fig. 3.12: Time-Frequency representation (WVD) of the two accelerating targets of Fig. 3.11. In (a), the acceleration in range with 1 m/s^2 is shown, in (b) the one in azimuth with 1 m/s^2 .

3.7 Target Vibration

Apart from constant target motion and acceleration, less common movements like rotation have been an early issue for SAR [116] and micro-Doppler analysis of vibration, rotation, and related motion patterns still are [37, 117, 118]. In [113], SAR imaging of moving targets is discussed in chapter 7 and micro-Doppler phenomena of vibration and rotation in chapter 8. Similar SAR micro-Doppler analyses are presented in [119, 120].

As implied by the name micro-Doppler, vibration induces very small Doppler frequency modulations in a radar signal. They originate from a target oscillation of at most tens of hertz with amplitudes being no more than a few millimeters. Clearly, mmW radar systems are especially well-suited to detect such small oscillations. Vibration amplitudes affect mmW radar wavelengths much more than longer carrier wavelengths. Non-SAR studies of vibration analysis in mmW radar have recently been conducted [121]. We show the effects of vibration in SAR here, as well as why rotation is a special case of vibration. Whereas in [37], micro-Doppler theory is discussed in detail, we lay our main focus on an accurately described system and simulation model as well as on real data from plausible targets, namely results of vehicle vibrations and radar dish rotations.

Mechanical vibrations or rotations of radar targets induce phase modulations in the received signal. These modulations are caused by the aforementioned micro-Doppler phenomenon, and they create sidebands in the Doppler frequency spectrum of the target [113].

A vibration may originate from a wide range of objects: from a standing vehicle with

a running engine (e. g. in a traffic jam) to large earth surface areas shaking during an earthquake. As we will see, vibrations cause a superimposed phase modulation on the received SAR signals.

We assume effects to be dependent on sensor azimuth time T and consider vibrations in range only because vibrations in azimuth result in insignificant smearing of objects (see [30]). Apart from the vibration, the target does not move. Hence, we define a point target n by its vibration in range

$$V_n(T) = A_{V_n} \cos(\omega_{V_n} T) \quad (3.43)$$

with vibration amplitude A_{V_n} and frequency ω_{V_n} . The target's instantaneous position is

$$\mathbf{Q}_n(T) \approx \begin{pmatrix} r_n + V_n(T) \\ z_n \end{pmatrix}. \quad (3.44)$$

The approximation is valid if we assume a large sensor to target distance and a small antenna aperture ($r_n^2 + (z_n - u)^2 \approx r_n^2$) as is the case for mmW SAR. The target velocity components are $v_{z_n} = 0$ and

$$v_{r_n}(T) = \frac{dV_n}{dT} = -A_{V_n} \omega_{V_n} \sin(\omega_{V_n} T). \quad (3.45)$$

To calculate the target Doppler shift due to the vibration we could use (3.1), (3.29), and (3.31). Equivalently, we may use (3.43) and the two-way change of phase due to the vibration to get

$$\Delta\varphi_n(T) = \frac{4\pi}{\lambda} A_{V_n} \cos(\omega_{V_n} T) \quad (3.46)$$

with the wavelength $\lambda = 2\pi c/\omega_c$. The vibration-induced micro-Doppler shift is

$$\begin{aligned} f_{d_n,vib}(T) &= \frac{1}{2\pi} \frac{d\Delta\varphi_n(T)}{dT} \\ &= \frac{-2A_{V_n} \omega_{V_n}}{\lambda} \sin(\omega_{V_n} T). \end{aligned} \quad (3.47)$$

We see that a vibrating target in SAR causes a modulation, $f_{d_n,vib}(T)$, in the received signal phase of (3.31). We also see that this effect depends on the wavelength and is strongest for a small λ as in mmW SAR.

The phase modulation causes an effect in SAR images known as paired echoes. As the name suggests, we get ghost targets above and below a vibrating target due to the Doppler shifts. As shown in [37, 113], target vibration induces an infinite series of paired echoes κ because, when considering (3.47), the received signal of (3.31) may be expressed by a series expansion with the Bessel function of the first kind of order κ

$$J_\kappa(x) = \frac{1}{2\pi} \int_{-\pi}^{\pi} e^{j(x \sin \nu - \kappa \nu)} d\nu \quad (3.48)$$

where $x = A_{V_n} \frac{4\pi}{\lambda}$ and $\nu = \omega_{V_n} T$. Since

$$\lim_{\kappa \rightarrow \infty} J_\kappa(x) = 0 \quad (3.49)$$

the paired echo signal strength decreases with increasing κ . As shown in (3.3), the displacement of the κ th paired echo coming from the vibration of target n is

$$d_{n,\kappa} = \mp \frac{\kappa \lambda \omega_{V_n}}{4\pi} \cdot \frac{1}{v_s} r_n. \quad (3.50)$$

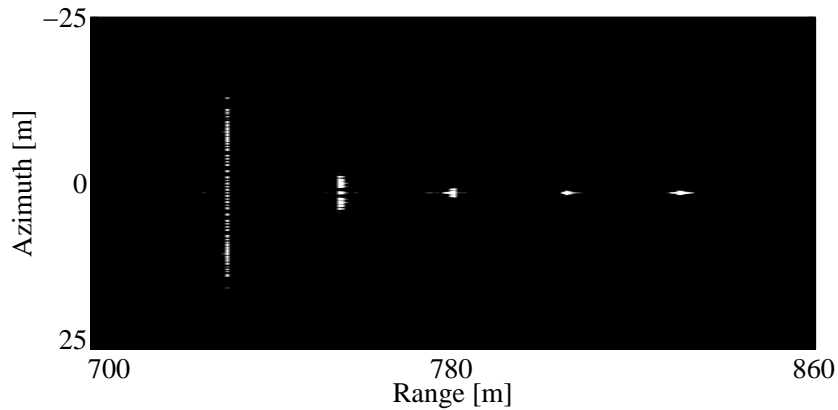
One last point to mention is that, if the SAR carrier platform is an airplane, additional micro-Doppler frequencies may come from platform vibration. This is discussed in [37] and is closely related to target vibration. Fig. 3.6 in Chapter 3.5.2 indicates that we may ignore micro-Doppler effects from platform vibrations in our examples. The distribution for a static corner reflector does not show any discernible micro-Doppler phenomenon, probably because MEMPHIS was carried on a very large and stable platform, the aforementioned C-160. Hence, we assume platform motion to be negligible in the following MEMPHIS data, too.

3.7.1 Analysis of Simulated Data

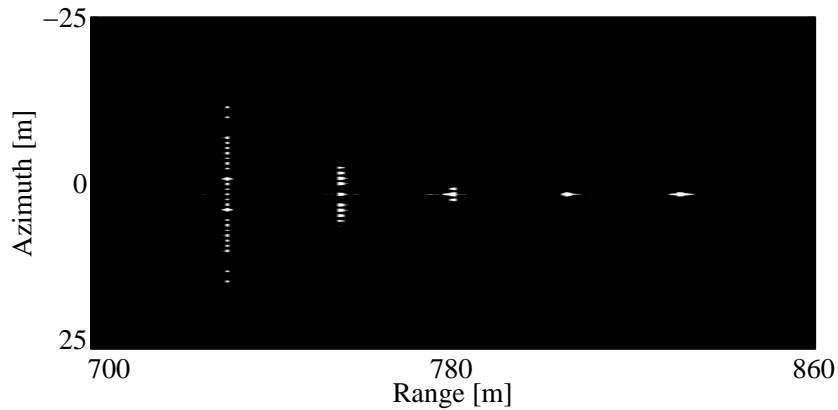
With the presented system model and the theoretical analysis of micro-Doppler phenomena, we are able to simulate vibration in raw SAR data. A visual evaluation is then possible from focused images and from a time-frequency analysis with the smoothed pseudo-WVD. In the following, we present focused simulated mmW SAR images that have been processed with the extended chirp scaling algorithm [21] as well as time-frequency analysis from pulse compressed data only.

There is the possibility to not only analyze the Doppler spectrum of a target but also its signal spectrum. For a static point target and a chirped signal, this would be something very similar to the image in Fig. 3.5, but with a truly linear slope for a linear chirp instead of (3.22), a measurement time of only the pulse duration (1.2 μ s), and a much larger spectral bandwidth of megahertz instead of hertz. These are important points. If we want to analyze micro-Doppler effects with frequency values of at most tens of hertz, we are well advised to do so in the Doppler spectrum where our measurement time—the dwell time of the radar—is much longer and frequency resolution is higher than in the signal spectrum.

In the focused SAR image of Fig. 3.13(a), we simulated five vibrating point targets, all with a vibration frequency of 30 Hz. The vibration amplitude A_{V_n} for targets from left to right is decreasing from 10 mm to 0.001 mm. All vibrations are in range, perpendicular to the flight track, and zero movement in azimuth is assumed. While targets with large vibration amplitudes clearly show multiple and very densely spaced paired echoes as theoretically predicted by (3.50), the paired echo signal strength of small vibration amplitudes is not visible at all. The spacing between paired echoes is a mere 0.08 m.



(a) 30 Hz Vibrations



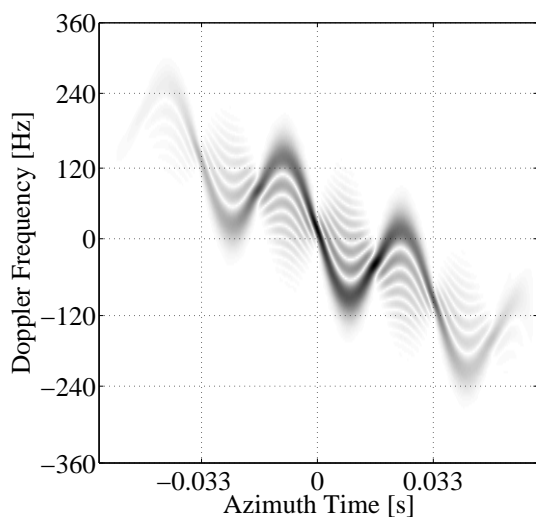
(b) 50 Hz Vibrations

Fig. 3.13: Focused 94 GHz SAR images, each with five simulated targets vibrating in (a) with 30 Hz and in (b) with 50 Hz. Vibration amplitudes from left to right are 10, 1, 0.1, 0.01, and 0.001 mm for both images.

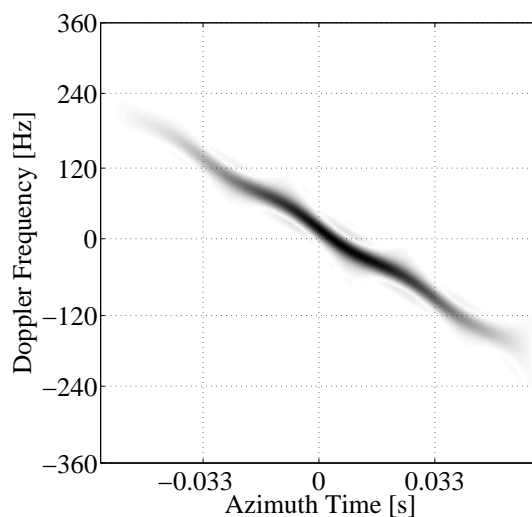
To compare the influence of vibration frequency on target signatures, the simulation has been repeated with five targets vibrating at the same amplitudes but at a frequency of 50 Hz in Fig. 3.13(b). As (3.50) predicts, the spacing between paired echoes increases and is 0.13 m. Once more, the amplitudes of 0.01 and 0.001 mm of the two targets to the right are too small for any visible effects.

Clearly, it is very difficult to measure target vibration frequencies from the displacement of paired echoes in focused SAR images. This is the case even for a large vibration amplitude of 1 mm at low frequency of 30 and 50 Hz, as the second targets from the left in both, Fig. 3.13(a) and (b) show. A time-frequency analysis gives much better information as we may see from Fig. 3.14 where we analyzed four of the ten targets of Fig. 3.13 via a smoothed pseudo-WVD. While the static Doppler slope is always visible

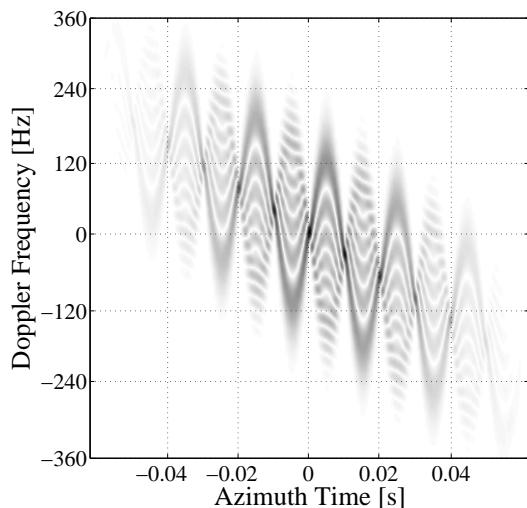
in the data, we can clearly discern a vibration signature for all four targets and even approximate the vibration frequency by the naked eye when counting wave periods over time. In Fig. 3.14(a), we see a target vibrating at 30 Hz and with an amplitude of 1.0 mm. This means that the wave period must be 0.033 s. The determination of the vibration



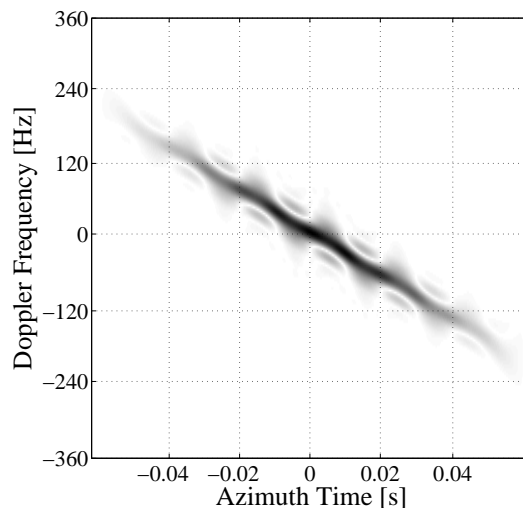
(a) Frequency: 30 Hz, Amplitude: 1.0 mm



(b) Frequency: 30 Hz, Amplitude: 0.1 mm



(c) Frequency: 50 Hz, Amplitude: 1.0 mm



(d) Frequency: 50 Hz, Amplitude: 0.1 mm

Fig. 3.14: Time-frequency representation (WVD) of four simulated SAR targets vibrating at frequencies of either 30 or 50 Hz and with amplitudes of 1.0 or 0.1 mm.

amplitude is possible since (3.47) states that

$$A_{V_n} = -\frac{f_{d_n,vib}(T)\lambda}{2\omega_{V_n}}. \quad (3.51)$$

With $\omega_{V_n} = 2\pi \cdot 30$ Hz, an amplitude of $A_{V_n} = 1.0$ mm must result from a local maximum of $f_{d_n,vib} = 118$ Hz, which may be extracted from the plot by removing the constant Doppler slope. In Fig. 3.14(b), the same vibration frequency and an amplitude of 0.1 mm results in a local maximum of $f_{d_n,vib} = 11.8$ Hz. We see that the interpretation of the target signature becomes harder. This agrees with our findings from the intensity image of Fig. 3.13(a). Still, we may discern a target vibration and approximate the vibration frequency. In the intensity image, this would be near to impossible.

For target vibrations of 50 Hz, a time-frequency analysis in Fig. 3.14(c) and (d) shows corresponding results. While the focused SAR image gives us almost no information on vibration, a smoothed pseudo-WVD identifies a wave period of 0.02 s and correct local maxima of $f_{d_n,vib} = 118$ and 11.8 Hz after subtracting the constant Doppler slope.

3.7.2 Analysis of Vehicle Vibration

Simulation results from the previous section show that whether or not target vibrations are visible may depend highly on vibration amplitude. While a higher vibration frequency causes paired echoes to be spaced farther apart from the actual target and more easily recognizable in a focused SAR image (see simulations in Fig. 3.13), it is a higher amplitude that introduces clear vibration signatures of a target in the images as well as in a time-frequency representation. We are aware of but a single publication showing real data of vibration from a target other than a corner reflector in the open literature; in [9], data from a vibrating truck is given, but unfortunately with no reference to the vibration parameters or SAR sensor. In [37] and [120], corner reflectors vibrating at 2 Hz and 1.5 mm amplitude in X-band SAR are presented, obviously with a very large amplitude and low vibration frequency, making the targets easily detectable but less realistic.

Our own experiment with MEMPHIS included two identical modern-day trucks on the airfield tarmac. Prior to the experiment, truck vibration characteristics were measured by triaxial accelerometers showing a linear frequency response from 0 to 150 Hz with an accuracy of $\pm 1\%$ and an acceleration measurement range of ± 1 g with an accuracy of $\pm 1.5\%$ [122]. Measurements were made for an idle engine and at higher rounds per minute. Because the largest vibrations were detected to be caused by an idle engine, we decided to use idle engine vibrations in our experiment. In Fig. 3.15(a) and (b) the idle motor engine vibration amplitudes are shown for a first measurement at the front bumper of a truck and for a second one on the cab roof. Maximum values are located at around 0.1 mm with strong variations of direction. Up and down movements on the truck roof were found to be the strongest.

In Fig. 3.16, the vibration frequency spectrum of such a truck with an idling engine is shown. Measurements were again done at the front bumper and on the roof. The peak

frequency for both measurements was close to 32 Hz with a second harmonic at 64 Hz, weaker than the peak by almost 20 dB.

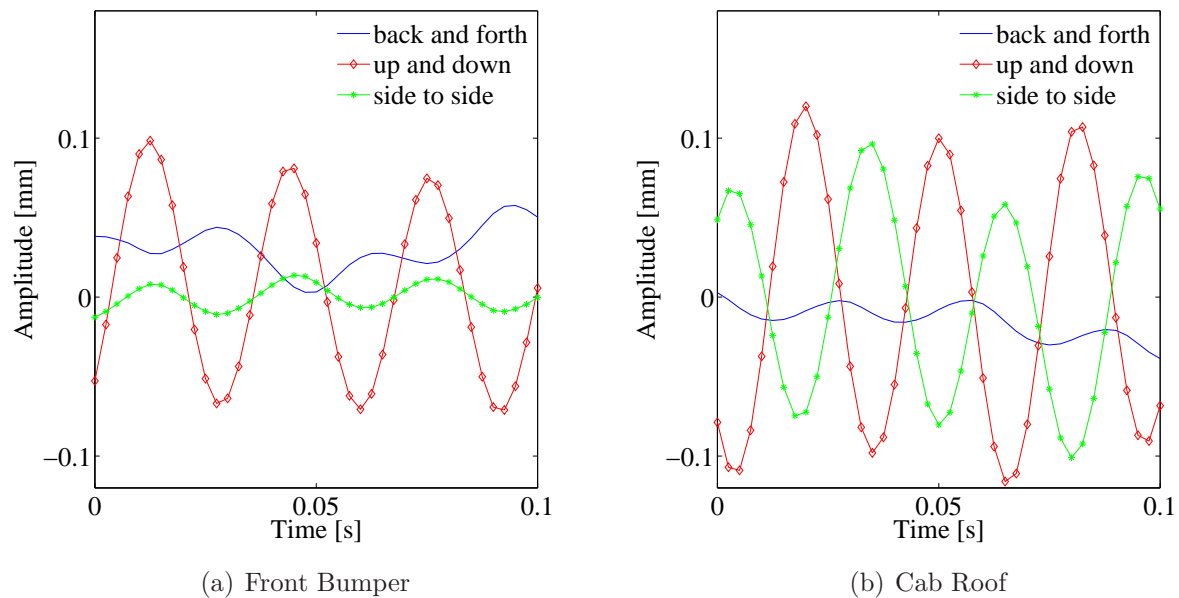


Fig. 3.15: Measured vibration amplitudes at the front bumper and on the cab roof of a truck running with an idle engine.

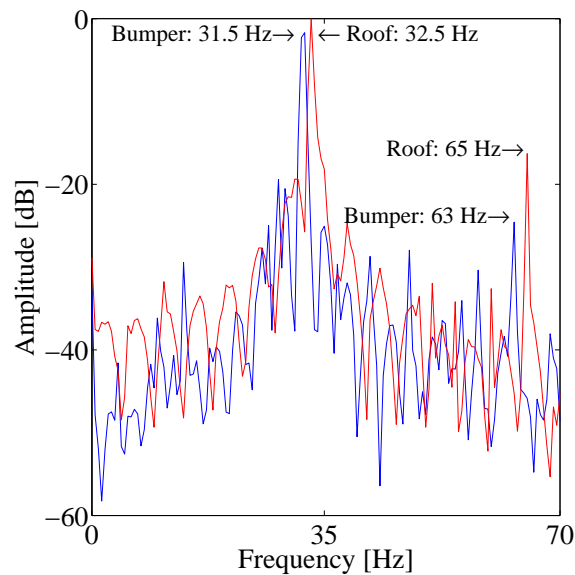


Fig. 3.16: Measured vibration frequencies at the front bumper (red) and on the cab roof (blue) of a truck running with an idle engine.

During the SAR experiment, the engine of one truck was turned off, and it was used as a permanent reference target during all data takes while the second one had its engine running idly. They were both parallel to the range axis with their cabs facing the radar because we assumed the highest target returns to be coming from the metallic cab. The focused SAR image of the two trucks is given in Fig. 3.17. There, no clear vibration-induced image signature is recognizable and no paired echoes are visible. The target vibration amplitude was small and the depression angle of the SAR was not optimal at 20° , focusing on the weak back and forth movement instead of the somewhat stronger up and down movement.

In Fig. 3.18(a) and (b), the smoothed pseudo-WVD of the two trucks is given. We see that their time-frequency characteristics are very different from a corner reflector which has to be expected when considering the many angles and faces of a truck, especially at mmW SAR. The plot for the static truck in Fig. 3.18(a) shows two very prominent areas at around ± 150 Hz Doppler. This may be caused by the space between cab and trailer, acting as a corner reflector from certain angles. There is no clear pattern recognizable, apart from fluctuating variations of the signal intensity due to the truck geometry. The plot for the vibrating truck in Fig. 3.18(b), however, appears to include a micro-Doppler pattern. We are able to discern a periodic signature at the confirmed vibration frequency of 32 Hz (0.03 s) and also of its harmonics. Unfortunately, the prominent areas of high signal strength, that are well observable for the static truck, are located around the same frequencies as the ones that seem to be coming from vibration nodes. Because the signal

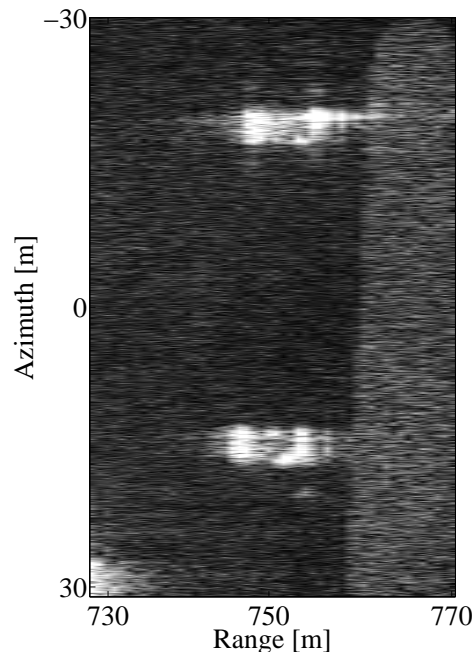


Fig. 3.17: Focused SAR intensity image of a static (top) and a vibrating (bottom) truck on a tarmac next to a meadow. No vibration-induced image signatures are recognizable.

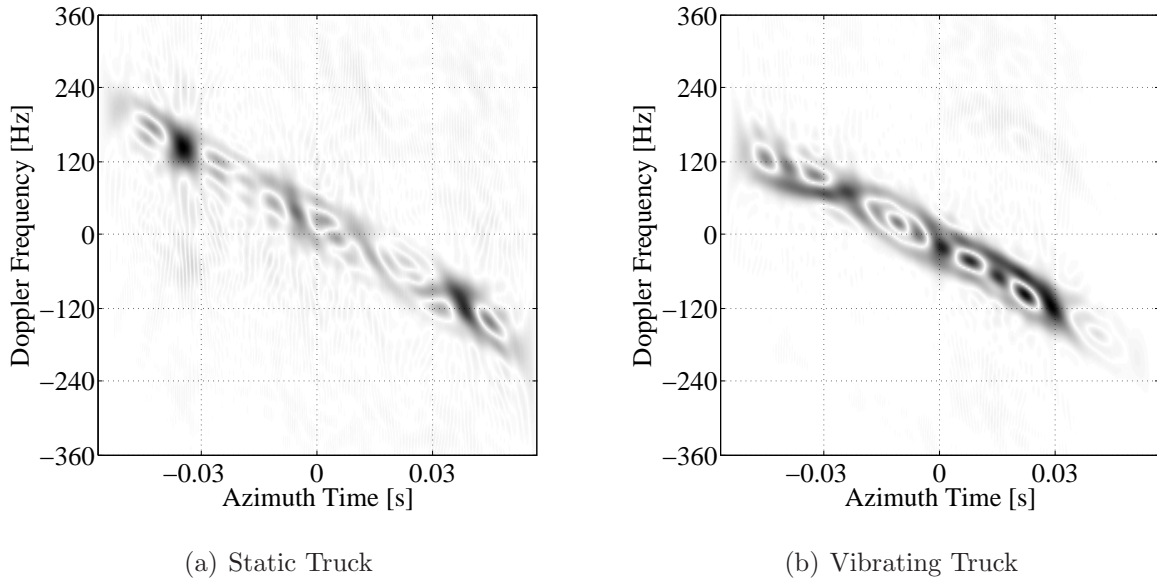


Fig. 3.18: Time-frequency representation (WVD) of the Doppler spectrum for (a) the static truck at the top and (b) the vibrating truck at the bottom of Fig. 3.17.

becomes weak after about ± 0.05 s due to target geometry, it does not allow the detection of further vibration nodes. A larger vibration amplitude would certainly make an analysis easier and better confirmable. Vehicles with a larger amplitude, however, may be hard to find in the real world.

3.8 Target Rotation

Examples of objects with rotating motion include ground-based surveillance radar antennas or helicopter rotors. They may have very different backscattering properties, but show common movement and therefore similar Doppler characteristics [118, 123]. As presented in the following analysis, the Doppler signature from rotating motion is closely related to vibration.

We develop a model for an extended object consisting of multiple aligned point targets moving in a circle around a common center. All point targets m of a rotating object n share a common rotation frequency ω_{R_n} but have individual radii $R_{m,n}$ from the center (r_n, z_n) of the object. We define the instantaneous position of such a point target as

$$\mathbf{Q}_{m,n}(T) = \begin{pmatrix} z_n + R_{m,n} \cos(\omega_{R_n} T + \phi_{0_n}) \\ r_n + R_{m,n} \sin(\omega_{R_n} T + \phi_{0_n}) \end{pmatrix} \quad (3.52)$$

where ϕ_{0_n} is the initial angle of the target at time zero. Fig. 3.19 illustrates the idea behind (3.52).

These positions $\mathbf{Q}_{m,n}(T)$ may easily be incorporated into our standard model of (3.15) for the received echoes at the SAR antenna. Depending on the method we either calculate the instantaneous radial velocity and the Doppler shift according to (3.1) or we define the two-way phase change $\Delta\varphi_{m,n}(u)$ of m as for vibrations. To use the instantaneous velocity is the direct approach; thus we need the velocity vector given by

$$\frac{d\mathbf{Q}_{m,n}}{dT} = \begin{pmatrix} -R_{m,n}\omega_{R_n} \sin(\omega_{R_n}T + \phi_{0_n}) \\ R_{m,n}\omega_{R_n} \cos(\omega_{R_n}T + \phi_{0_n}) \end{pmatrix}. \quad (3.53)$$

Together with (3.1) and (3.29), we may then add a rotation-induced micro-Doppler shift into (3.31), given as

$$\begin{aligned} f_{d_n,rot}(T) &= \frac{\omega_c}{\pi C} \left[-\sin(\omega_{R_n}T + \phi_{0_n}) \cos(\varphi_n(T)) \right. \\ &\quad \left. + \cos(\omega_{R_n}T + \phi_{0_n}) \sin(\varphi_n(T)) \right] \cdot R_{m,n}\omega_{R_n} \\ &= -\frac{\omega_c}{\pi C} [\sin(\omega_{R_n}T + \phi_{0_n} - \varphi_n(T))] R_{m,n}\omega_{R_n}. \end{aligned} \quad (3.54)$$

As for vibration, we see that the micro-Doppler effect of a rotation is larger with smaller wavelength λ or higher carrier frequency ω_c , making mmW SAR suitable for detection of such effects.

An important aspect of rotating objects is their change of reflectivity during rotation. If we assume a ground-based planar radar antenna as our rotating object, it is clear that the antenna broadside will have a much higher reflectivity than its side profile. We may optionally introduce amplitude weighting to make up for this rotation signal amplitude change by defining a variable reflectivity

$$A_{m,n}(T) = \frac{A_n}{2m} (1 + |\cos(\omega_{R_n}T + \phi_{0_n})|). \quad (3.55)$$

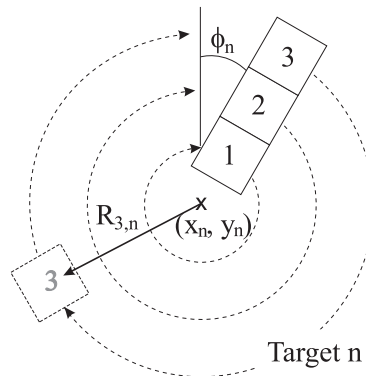


Fig. 3.19: A rotating target n , consisting of $m = 3$ point targets with radii $R_{m,n}$ sharing a common center, rotation frequency and phase offset ϕ_{0_n} .

The purpose of the factor $1/2m$ is to define the overall maximum reflectivity A_n of a rotating object equal to the reflectivity of a static point target, making a direct comparison possible.

Because a rotation implies a constantly changing velocity at every point of an object with non-zero $R_{m,n}$, we get many effects for rotating targets, caused by the Doppler shift of (3.1). We will see this clearly when we look at simulated and real data below.

3.8.1 Analysis of Simulated Data

First results of rotating objects in SAR have been presented in [116]. We simulated the large variable displacement effects (smearing) that appear in an ideal situation (no background clutter) in Fig. 3.20 where three rotating objects are visible. We made the following assumptions as to the rotation movement. Each object is made up of two point targets, a static one representing the immobile part of an object (and giving us a feeling of where the object is truly located in the SAR image) and a rotating one circling the static one at a distance of $R = 0.5$ m. The reflectivity of the circling target does not change with aspect angle; this is an idealistic assumption but prevents the loss of information because of reflectivity changes that may occur during a rotation. Simulations with changing amplitudes have been carried out, too. The attenuation and partial disappearance of the signal reflected from the target, however, is not helpful to the understanding of rotation effects.

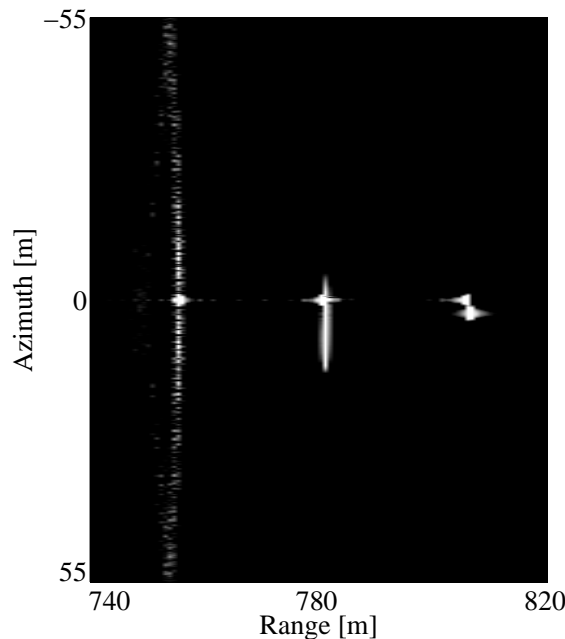


Fig. 3.20: Three simulated focused 94 GHz SAR targets rotating at 10 Hz (left), 0.5 Hz (center), and 0.2 Hz (right), all with a rotation radius of 0.5 m.

In order to show that the smearing effects may be asymmetrical, we gave the rotation an offset of $\phi_{0_n} = \pi/8$ for all targets as defined in (3.52). Finally, the rotation frequency was chosen to be 10 Hz for the left target, 0.5 Hz for the center target and 0.2 Hz for the right target.

We may discern the individually sampled displacements of the target rotating with 10 Hz in Fig. 3.20 quite easily, and we may also identify a slight range curvature or range bin changes due to the radius of rotation. Obviously, the first phenomenon is heavily dependent on the SAR system PRF and the second one on target radius and SAR resolution. The other two targets are harder to analyze because their rotation periods of 2 and 5 s is larger than the SAR dwell time of 0.5 s. We can only observe a partial period of rotation.

A time-frequency analysis shows good results that correspond well with theoretical results. In Fig. 3.21, the 10 Hz rotation is shown over a time interval of the full radar dwell time of 0.5 s. We may easily identify the rotation period of 0.1 s per turn. Additionally, a clear relation to target vibration may be seen from Fig. 3.21. If we were to fully ignore the small smearing effects caused by the rotation movement in azimuth, we would have a pure vibration at 10 Hz and with an extremely large vibrational amplitude of 0.5 m. Thus, the basic difference in real world vibrations from real world rotations is the magnitude of movement and the frequency. This means that we may even use (3.51), which we stated for vibrations, to determine the radius of rotation from a time-frequency signature.

A much smaller rotation frequency of 0.5 Hz, observed over the same time interval of 0.5 s, shows the expected partial signal pattern in a time-frequency distribution, as given in Fig. 3.22(a) for the center target of Fig. 3.20. An approximation of the rotation frequency

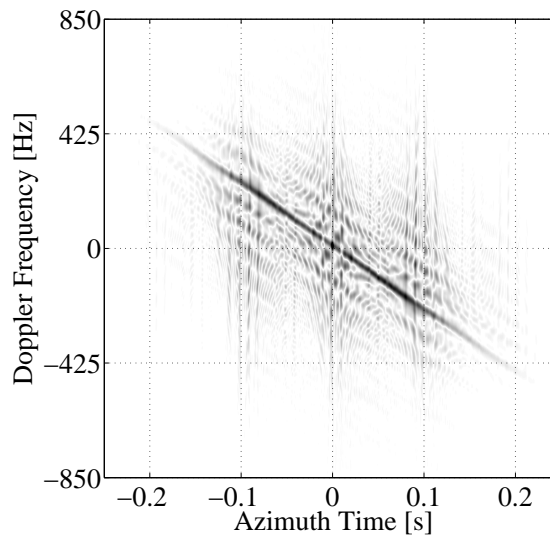


Fig. 3.21: Time-frequency representation (WVD) of a simulated target rotating at 10 Hz. The pattern shows the relation to vibrations as given in Fig. 3.14.

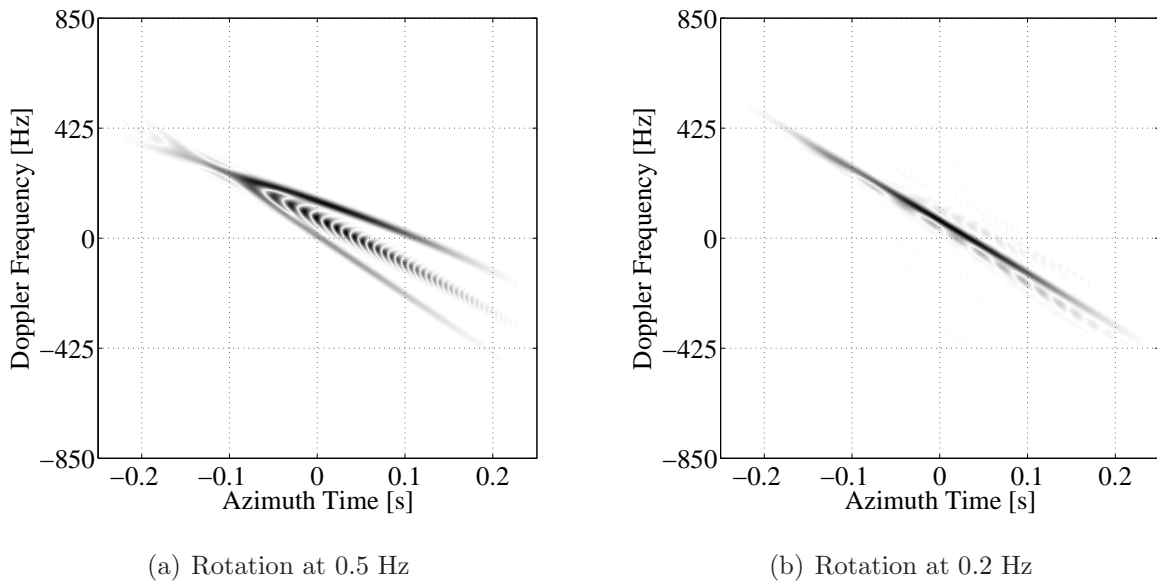


Fig. 3.22: Time-frequency representation (WVD) of two simulated rotating targets with individual rotation frequencies of 0.5 Hz in (a), and 0.2 Hz in (b) respectively.

is possible since the time-frequency characteristic shows one forth of a sine wave in 0.5 s. Similarly, the time-frequency representation for the target rotating with 0.2 Hz is shown in Fig. 3.22(b). A small deviation from the signature to be expected of a static target is visible, indicating a slow rotation. Unlike in Fig. 3.22(a), it becomes clear that such a small observation interval does not provide sufficient information on the movement in the time-frequency distribution. Such a slow rotation may best be extracted with traditional GMTI methods as done in Chapter 5.4.

3.8.2 Rotation of a Reflector and of a Radar Dish

A second setup during the MEMPHIS data collection experiment described above included a rotating corner reflector turning with 1 Hz on a heavy wooden pedestal on the airfield tarmac. The reflector was a four-way trihedral reflector mounted to a lever arm that was moved by an electric motor, which allowed the rotation frequency to be tuned to one hertz. The lever arm and thus the rotation radius was 1 m. The reflector was fixed to the lever arm and did not rotate on the arm. Hence, it did not provide a constant radar cross section. Its four-way reflection characteristics, however, prevented zero reflectivity from any angle and reduced the variation with a maximum cross section every 90°. Fig. 3.23 shows the pedestal, the lever arm, and the reflector during the experiment.

The rotating corner reflector was imaged with MEMPHIS during the same overflight as the two trucks. The resulting focused reflector is shown in Fig. 3.24 with a 0.75 m resolution. At the top of the image, the pedestal is shown as a small target. The moving



Fig. 3.23: Rotating corner reflector turning on a pedestal with 1 Hz.

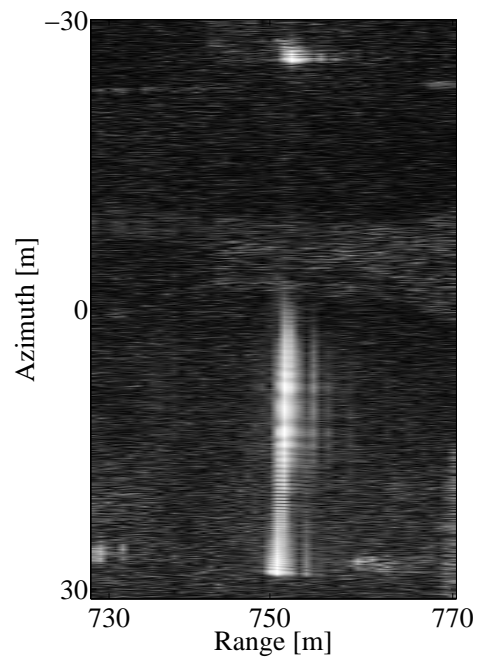


Fig. 3.24: Focused SAR intensity image of the rotating corner reflector from Fig. 3.23 turning on a pedestal with 1 Hz. The pedestal is recognizable at the top of the image while the rotating reflector is smeared in azimuth from center to bottom.

corner reflector is heavily smeared in azimuth and, because of low clutter returns from the tarmac, it is very nicely visible. The signal from the rotating corner is asymmetrically smeared with no returns above the static pedestal because only a partial rotation was recorded by the SAR. This is comparable to simulation results (see Fig. 3.20). The dwell time of the SAR over the target was approximately half a second.

To get reference data and offer change-detection possibilities, the corner reflector was also imaged when not moving during another overflight. This data confirmed an absent signal in regions whereto the corner reflector was smeared during rotation and a stronger signal at the pedestal and true corner location.

A time-frequency analysis with the smoothed pseudo-WVD of the rotating corner reflector in the pulse compressed radar data gives us a very illustrative Doppler frequency spectrum over time, as shown in Fig. 3.25. Instead of a straight line as for a static target, we receive a curve clearly reflecting the varying acceleration of the corner during a rotation. While the focused SAR intensity image from Fig. 3.24 may leave doubts about the origin of a smeared target signature, the time-frequency analysis proves the rotation movement of the reflector.

To show that the detection of rotation is not only possible for artificial targets such as a rotating reflector, we also imaged the airfield air surveillance radar dish located nearby (see Fig. 3.26). Its antenna has a large diameter of several meters and a rotation frequency of one complete turn every four seconds. The impressive focused SAR intensity image is shown in Fig. 3.27. While the asymmetrical, experimental rotating corner reflector showed an asymmetrical SAR signature, the symmetrical surveillance radar dish gives a more point-symmetrical image. A signature with such large displacement effects for a

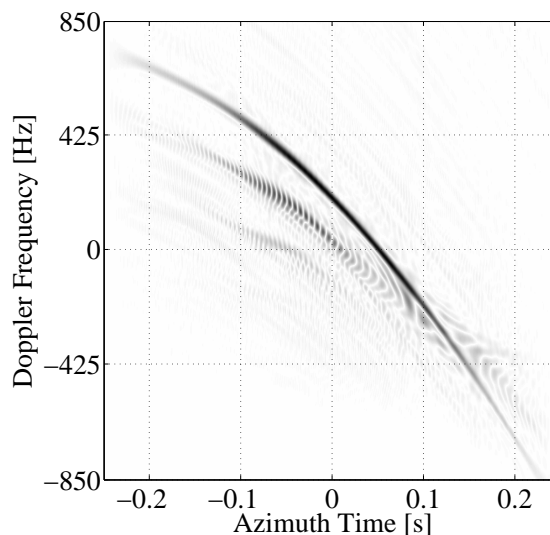


Fig. 3.25: Time-frequency representation of the corner reflector from Fig. 3.23, rotating at 1 Hz.



Fig. 3.26: An airfield air surveillance radar dish with a maximum diameter of almost 10 m.

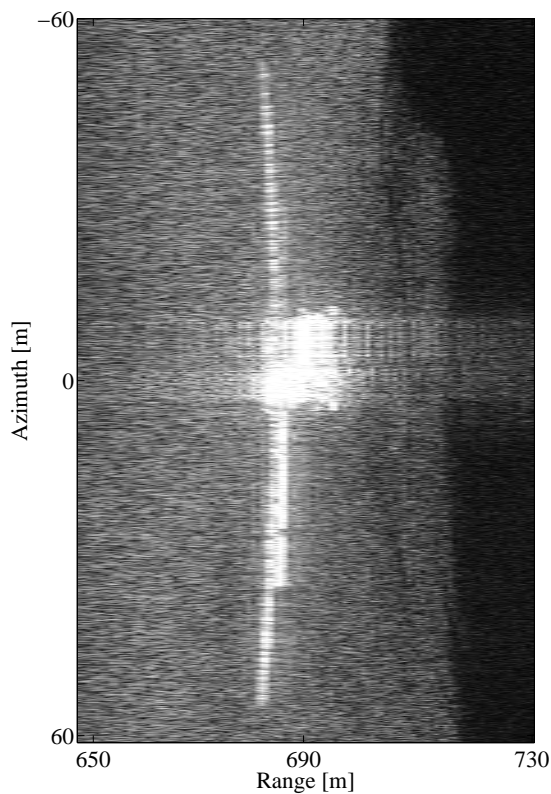


Fig. 3.27: Focused SAR intensity image of a ground-based radar antenna with a diameter of several meters, rotating at 0.25 Hz.

small rotation frequency of 0.25 Hz and dwell time of 0.5 s is only possible if the timing between SAR and radar dish rotation is harmonized, meaning a frontal SAR imaging of the antenna dish. Imaging of the antenna dish from the side would mean a lower cross section in the SAR and radial velocities of close to zero, giving small displacement effects.

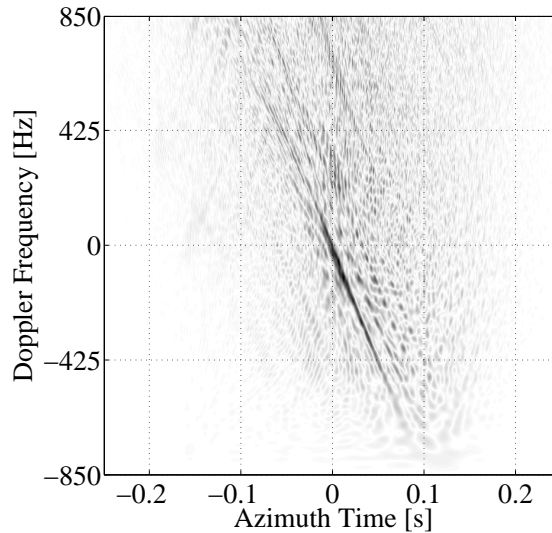


Fig. 3.28: WVD of the ground-based radar antenna from Fig. 3.27.

In Fig. 3.28, the time-frequency representation of the air surveillance radar dish is given. The signature shows a slight indication of a small fraction of a sine wave period, indicating a small rotation frequency of the target. After all, the SAR dwell time of 0.5 s allows for only one eighth of a rotation. Also shown are large returns of the static antenna pedestal. The advantage of the time-frequency representation is that, even if the imaging of the antenna had happened from the side with only small displacement effects in the SAR image, a curvature of the signature would eventually be visible.

Three more images of the ground-based radar dish, taken during the same flight campaign as the one of Fig. 3.27, show different angles of the dish on the ground during SAR imaging in Fig. 3.29. The effect of a varying target reflectivity, depending on rotation angle at the time of imaging with the SAR, is nicely illustrated in the three images. While the image on the left shows the radar dish imaged mostly with its front towards the SAR, the one in the middle clearly indicates a squinted angle between dish and SAR and the one on the right a side view of the dish with almost no radial velocity and no smearing.

If we are to estimate a rotation frequency of a target from its time-frequency analysis, we see a strong dependence on the dwell time. For the rotating corner reflector, we might be able to derive the actual rotation frequency of 1 Hz from the fact that half a sine wave is visible over 0.5 s in the time-frequency representation of Fig. 3.25. For the surveillance radar dish, an estimation of the rotation frequency is almost impossible because only a small fraction of a sine wave is visible in the time-frequency representation of Fig. 3.28. This is supported by the simulation results in Fig. 3.22.

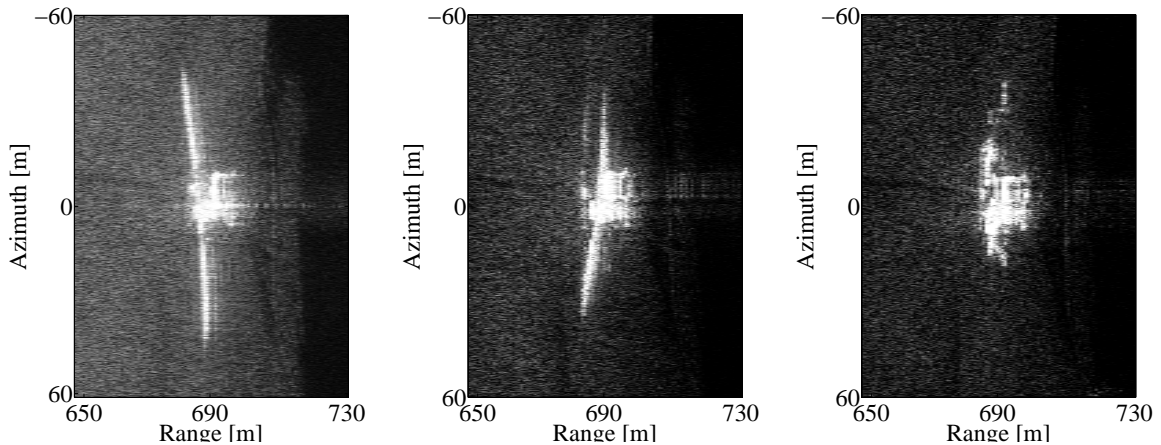


Fig. 3.29: Three focused SAR intensity images of the ground-based radar antenna dish of Fig. 3.26 with different angles of the dish during SAR imaging.

3.9 Discussion

Constant movement and acceleration are well-known and well-discussed target movements in SAR. Nevertheless, a thorough understanding and analysis of movement effects are important when wanting to develop GMTI algorithms. Aliasing effects of blind speeds and ambiguous Doppler shifts are essential especially for mmW GMTI.

Related to constant movement and acceleration, micro-Doppler effects are an interesting field of SAR research. A system model was proposed that allows flexible simulations of vibration and rotation. It defines the instantaneous position of a target, its displacement effects in SAR imagery, and the Doppler shifts induced in the signal. An analysis of motion patterns in focused intensity images as well as in time-frequency distributions was conducted, showing micro-Doppler phenomena in simulations and in real data that match the underlying signal theory.

We introduced the reader to the possibilities of airborne mmW SAR imaging of vibrating and rotating targets. The large range of potential applications may include anything from the detection of vehicles standing in traffic jams with idling engines to the reconnaissance of airfields where rotating helicopter blades or ground-based radar dishes are present.

The time-frequency distributions presented to analyze vibration and rotation were done using the smoothed pseudo-WVD, an energy distribution that is a compromise between joint time-frequency resolution and the level of interference terms. The Gabor transform, an atomic distribution that is well suited for data that is corrupted by noise and clutter, was considered as an alternative. Because the simulations were completely noise-free and the real data included a low clutter and noise level, the presentation of only WVD results is justified.

From theoretical analyses, mmW SAR is well suited to detect vibration and rotation

because it is very sensitive to micro-Doppler effects. Still, limitations are apparent for target vibrations with very small vibration amplitudes, such as the ones to be expected of a modern-day large truck with an engine running idly.

As seen in the simulated vibration data, a higher vibration frequency causes paired echoes to be spaced farther apart from the actual target and more easily recognizable in a focused SAR image while a higher amplitude introduces clearer vibration signatures of a target in the images as well as in a time-frequency representation. Although we showed only a limited variation of vibration amplitude and frequency parameters, results hinted at well detectable signal signatures for amplitudes larger than 0.1 mm. Results for smaller amplitudes tend to be harder to interpret, as was confirmed by the real data experiment with the two trucks.

The real data we presented was recorded with MEMPHIS at 94 GHz. First, an analysis of a static corner reflector showed that aircraft vibration did not influence time-frequency analyses of real data. An evaluation of the focused SAR image of a static and a vibrating truck did not show any visible effects. This confirmed our simulation results that pointed at too closely spaced and too weak paired echoes. The time frequency distribution, however, did give an indication of vibration, although the interpretation of the pattern proved to be less distinct than hoped for after analyzing the simulations.

Regarding the time-frequency signature of a vibrating truck, it could be seen that target geometry may influence the return echoes to an extent where it becomes difficult to identify an underlying micro-Doppler phenomenon from such a weak vibration. The SAR sensor depression angle may be important when considering that up and down vibrations of a vehicle are much stronger than back and forth or side to side vibrations, as our ground-truth measurements of the trucks showed. An imaging from the side of the trucks may in retrospect have been useful, even though the main radar returns had to be expected from the metallic cab. A quantitative conclusion on vibration amplitude limitations, however, is difficult and may depend too heavily on assumptions in a simulation or on sensor and target characteristics for experimental data.

For rotating targets, difficulties arose when imaging slow rotational movements where the rotation period was much larger than the radar dwell time, which is generally very short for mmW SAR. Nevertheless, focused images of rotating targets showed clear target displacement into many azimuth bins along the target range. Time-frequency distributions showed the micro-Doppler influence of rotation nicely for simulated as well as for real data. In particular, the faster rotations of a corner reflector and an antenna dish proved to be useful for an estimate of rotation frequency. An increased dwell time of the radar could be a welcome measure to increase visibility of time-frequency characteristics of rotating targets.

While vibration and rotation may be visible in a SAR intensity image, the origin of a smeared target signature or of paired echoes is most often not clear. A time-frequency analysis of such signatures, however, not only allows the target movement identification, but also the measurement of vibration amplitude and frequency as well as rotation fre-

quency and radius. A mmW wave sensor with a large dwell time and strong target vibrations of more than 0.1 mm or rotations where the rotation period is of the order of the dwell time seem to promise successful indication of both movements.

Chapter 4

Dual-Frequency Monopulse GMTI

Indication of target movement in SAR as discussed in the last chapter is difficult from information of a single data channel. Time-frequency representations may help as well as some specialized techniques like multilooking [72, 73]. However, a more efficient approach for GMTI is the use of multi-channel SAR systems for a space- and time-variant analysis of moving targets. A reasonable method, derived from well-known general concepts in radar engineering and developed specifically for mmW SAR, is presented and described in detail in the following. It allows the indication, correction of position displacement, and estimation of radial velocity components of moving targets in a SAR image. All three steps are possible due to a determinable Doppler frequency shift in the radar signal caused by radial target movement. The presented algorithms focus on the capabilities of the mmW SAR system MEMPHIS [1] with multi-channel amplitude-comparison monopulse data acquisition and the ability to use carrier frequencies of 35 and 94 GHz simultaneously, making it a dual-frequency SAR. The theoretical parts include a description of general monopulse techniques, mmW specific SAR GMTI considerations, an adaptive algorithm to collect velocity and position information on moving targets with mmW monopulse radar, and a discussion on GMTI blind speed elimination and target velocity ambiguity resolving by dual-frequency SAR. To determine the capabilities of both, system and algorithm, four large-scale experiments with MEMPHIS in different environments are presented in the following Chapter 5.

Monopulse processing for GMTI is often used as an equivalent to ATI in the SAR community [32]. We would like to make a distinction in that ATI refers to interferometric SAR (InSAR) and the direct comparison of two or more received data records [45] from multiple antennas. Monopulse or $\Sigma\Delta$ processing is a general term often used for tracking radar systems and always specified through a sum data signal and one or more isochronous difference data signals [124–126]. Monopulse processing makes use of the complex ratios between these multiple signals and is well suited for GMTI, as we will see in the following.

4.1 Monopulse Radar

4.1.1 Terminology, Definitions, Notations and Concepts

The term monopulse for radar systems was first introduced by H. T. Budenbom of the Bell Telephone Laboratories in 1946, according to a later paper by himself [127]. It is a hybrid word with *mono* being Greek and meaning one and *pulse* coming from the Latin word *pulsum*. Generally, the word describes the underlying technology quite well. A signal (a pulse) is emitted and its return echo is received by multiple, physically separated data channels. Because of time delays or intensity differences of a target in the channels, information on the angle to the target may be gained. This is especially useful for tracking radar systems, where this information may be directly used as an input to adjust the radar beam.

Prior to the use of monopulse, tracking systems extracted information from many pulses to determine target angle. Sequential lobing was one of the first tracking techniques where tracking was achieved by continuously switching a narrow beam between pre-determined symmetrical positions around the antenna's line of sight axis. A second technique is called conical scanning. It is a logical extension of sequential lobing with the one difference that, in this case, the antenna is rotating at an offset angle or has a feed that is rotated about the axis of the antenna [7]. Monopulse was then developed to replace the sequential pointing of an antenna beam by multiple parallel beams.

Target angle from a single pulse is gained in a monopulse system by differentiating between receive channels. A sum channel, Σ , consists of all available receive channels from all antenna beams. Further, in a classical system there are two difference channels, Δ , one in azimuth and one in elevation. As will be described below, generating a ratio between sum and difference channels, the angle to the target may be determined, in azimuth and elevation from one single pulse.

However, according to [124], there are at least two objections to the term monopulse:

- The word implies that angle estimates are formed from each pulse; this can be done, but it is not the way a monopulse radar actually tracks targets.
- The monopulse technique is not limited to pulsed radars; it can be used just as well in CW or modulated CW radars. It may even be used in a passive mode to track a source of signals or noise such as a transmitting antenna or even the sun.

When talking about monopulse, we have to differentiate between two closely related configurations of the antenna hardware. The first is called *phase-comparison monopulse*. It is the configuration that is most popular for SAR applications, be it for cross- or along-track interferometric uses. Such a monopulse system consists of a cluster of multiple reflectors. While the traditional tracking radars often show four reflectors side by side in a square or cloverleaf arrangement and joined together at their edges to form a rigid

assembly, InSAR often has the antennas spaced much farther apart or in the extreme even on two different carrier platforms, as planned for the TanDEM-X mission [53].

The alternative configuration is *amplitude-comparison monopulse*. It describes the concept of having a single-reflector antenna with a cluster of multiple feed horns. This may be a Cassegrain reflector as illustrated in Fig. 4.1 or a dielectric lens [128]. Because the horns are offset laterally from the focal point, the beams are squinted on opposite sides of the axis. They emit a common pulse that forms one large antenna beam signal as shown in Fig. 4.2, and signal reception is independent for all horns. The MEMPHIS systems uses a four-horn feed amplitude-comparison monopulse mode for GMTI as will be described in Chapter 4.2.

The antenna patterns of the component beams of the two classes are likewise distinc-

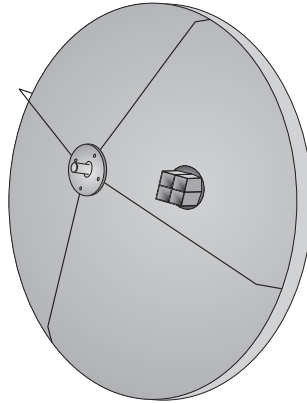


Fig. 4.1: Schematic amplitude-comparison monopulse Cassegrain reflector antenna with four receiver horns at antenna center.

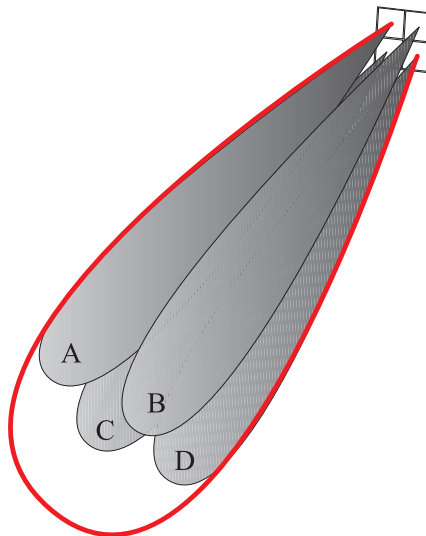


Fig. 4.2: Three-dimensional antenna pattern of an amplitude-comparison monopulse antenna with four horns.

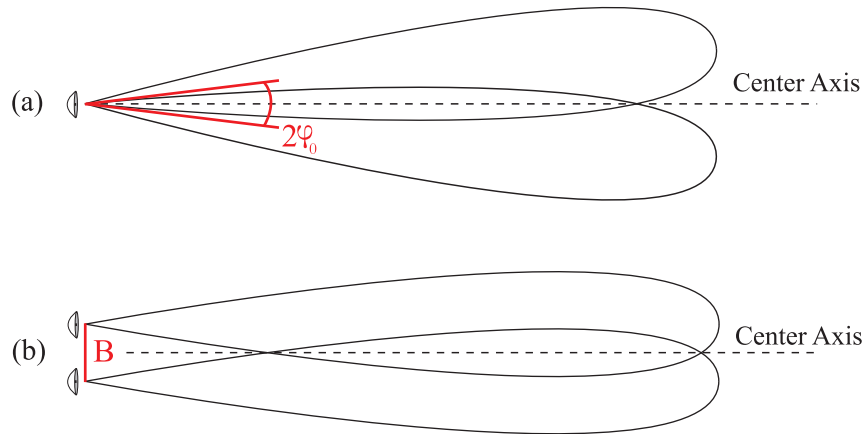


Fig. 4.3: (a) Amplitude-comparison monopulse with one phase center and two squinted beams. (b) Phase-comparison monopulse with two phase centers, parallel beams and a separation baseline.

tive. A pair of beams for each class is illustrated in Fig. 4.3. In amplitude-comparison monopulse, the beams have a common phase center but are squinted symmetrically away from the axis by the angle φ_0 . A target produces signal intensities of the same phase but different amplitudes in the two beams. The amplitudes are only equal when the target is on-axis. In phase-comparison monopulse, the beams are parallel and identical except for a lateral displacement of their phase centers on opposite sides of the axis. In SAR applications, this displacement is known as the baseline B .

If we assume an amplitude-comparison monopulse antenna with a four-horn feed arranged in a square as in Fig. 4.2, we may express the sum and difference signals in azimuth and elevation through the four feeds \mathbb{A} , \mathbb{B} , \mathbb{C} , and \mathbb{D} as

$$\Sigma = \mathbb{A} + \mathbb{B} + \mathbb{C} + \mathbb{D} \quad (4.1)$$

$$\Delta_{az} = (\mathbb{A} + \mathbb{C}) - (\mathbb{B} + \mathbb{D}) \quad (4.2)$$

$$\Delta_{el} = (\mathbb{A} + \mathbb{B}) - (\mathbb{C} + \mathbb{D}). \quad (4.3)$$

In theory, the four horns could be connected to four identical receivers, the outputs of which could then be compared. In practice, the four receivers, even if adjusted initially for equal gain and phase, would vary unequally as a function of time, signal level, radio frequency, and environmental conditions. The result, as was learned in some of the early monopulse development, would be large drifts in the electrical axis (boresight direction) and in the measurement of off-axis target angles. The usual method, therefore is to form the sum, an elevation difference, and an azimuth difference prior to the receiver through wiring or waveguides as shown in Fig. 4.4. Therein, the combining devices are known as hybrid junctions. Being electrically passive and mechanically compact and rigid, these

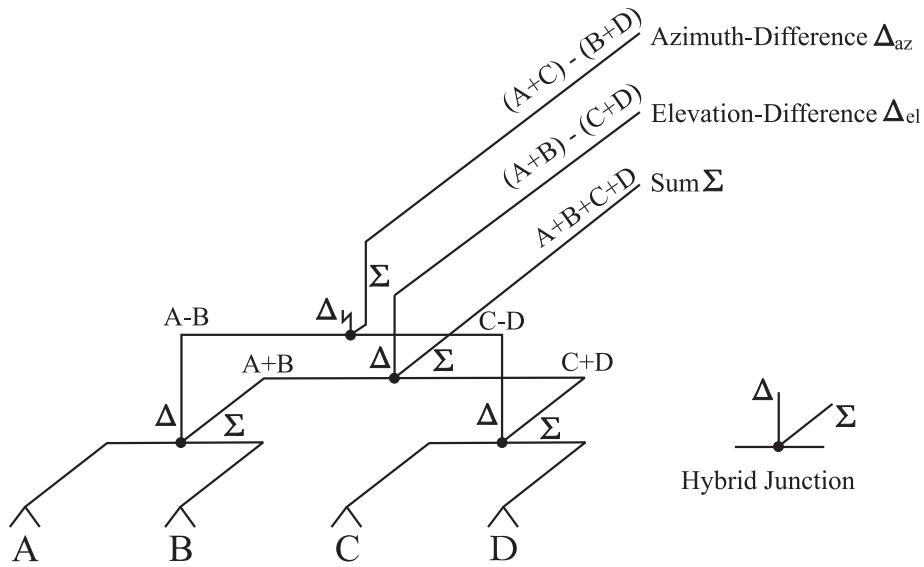


Fig. 4.4: Monopulse channel circuitry with four receive antennas and four hybrid junctions.

devices have much less drift than the active circuits in receivers, therefore the null axis is more stable [124].

It must further be pointed out that the patterns that are added and subtracted are not quite the same as the patterns that would be obtained from the individual horns if the other three horns were missing. They are not even the same as the outputs of the individual horns in the four-horn cluster since they are affected by mutual coupling. Therefore, they should be considered as members of a group rather than as patterns standing alone.

4.1.2 Amplitude Comparison Monopulse

A schematic target tracking with the squinted beams of an amplitude-comparison monopulse radar is shown in Fig. 4.5. While a target is on-axis of a ground-based tracking radar and produces equal signal strength in both its elevation beams $A + B$ and $C + D$ in the top image, in the bottom image the same target moved out of the antenna axis. Therefore, we would get $\Delta_{el} = 0$ for the top image and $\Delta_{el} \neq 0$ for the bottom one.

Extending the image in Fig. 4.5 to three dimensions, azimuth beams $A + C$ and $B + D$ allow the determination of the traverse angle to the target. Monopulse angle estimation is then possible by comparing the signal strengths in the various beams. These signal strengths are exactly proportional to the angular target position, and values may be used directly, e. g. as an input for angle correction in a tracking radar. In [129] angle estimation is described in detail.

Obviously, there exist many more design concepts for amplitude-comparison monopulse than the simple four horns arranged in a square as described here and in all subsequent chapters. One popular example is the five-horn feed antenna where an additional horn

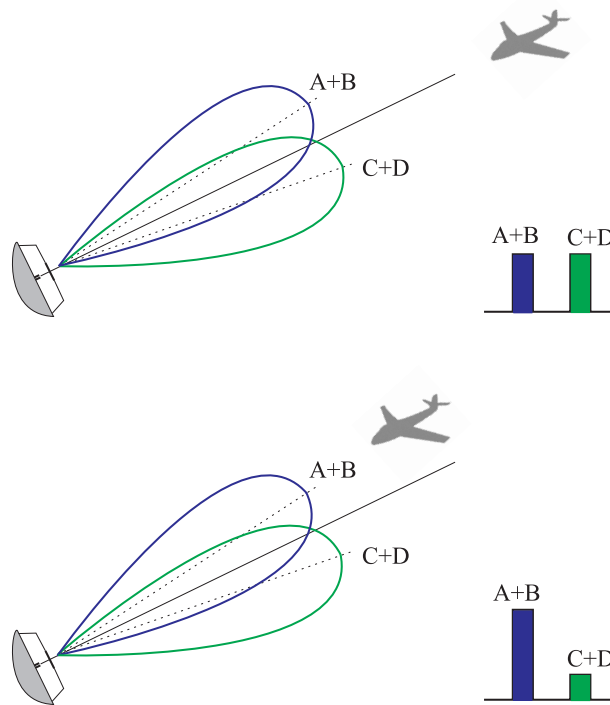


Fig. 4.5: Monopulse concept for a tracking radar. Top: a target is on-axis of a ground-based tracking radar and produces equal signal strength in both its elevation beams $\mathbb{A} + \mathbb{B}$ and $\mathbb{C} + \mathbb{D}$. Bottom: the same target moved out of the antenna axis, and the signal strength is not equal any more for the two beams.

is located at the center of the antenna to increase the power of the sum beam. Other examples include even more channels such as a 12-horn antenna presented in chapter 6.9 of [124]) or even a 24-horn antenna described in [130].

Let us return to the classical four-horn antenna with a small outlook to SAR. The reasons why we refer to the traverse difference signals as azimuth difference become obvious when we are merging monopulse radar with SAR in the following Chapter 4.2, where azimuth is the cross-range direction. Equally related to SAR is a relation of the monopulse sum and difference channels Σ and Δ with InSAR techniques. We mentioned earlier that phase-comparison monopulse would be used as an equivalent to interferometric antenna arrangements for SAR. A cross-track InSAR may be seen as a monopulse radar with an elevation difference while an along-track InSAR is the same as a monopulse radar with an azimuth difference. However, as we have seen when discussing ATI results for river flow velocities in Chapter 2.5.3, InSAR is usually not based on Σ and Δ , but on a master and a slave image, s_{c1} and s_{c2} , and hence the physically separated data channels. The two concepts may be translated into each other by the relations

$$\mathbb{M} = \frac{1}{2}(\Sigma + \Delta) \quad (4.4)$$

and

$$\mathbb{S} = \frac{1}{2}(\Sigma - \Delta). \quad (4.5)$$

where ideally $\mathbb{M} = s_{c1}$ and $\mathbb{S} = s_{c2}$ of Chapter 2.5.3. However, these equations are only valid for physically separated antennas with a large baseline between them. Otherwise, as mentioned above, the patterns that are added and subtracted are not quite the same as the patterns that would be obtained from the individual channels. For an amplitude-comparison monopulse radar, the assumptions $\mathbb{M} = s_{c1}$ and $\mathbb{S} = s_{c2}$ are most often not valid because of receiver characteristics and feed layout.

In [124] it is stressed, that amplitude-comparison and phase-comparison monopulse are two different configurations of the same concepts. The two terms amplitude and phase refer only to the way the antenna horns are set up and the way their beams are arranged with respect to each other. They have nothing to do with the way the received signals are processed. Neither does amplitude-comparison monopulse compare amplitudes nor does phase-comparison hint to a phase comparison. The standard handling and signal processing of monopulse data is equal for both concepts as described in the following.

4.1.3 The Monopulse Ratio and the Monopulse Curve

The processing of monopulse signals most often involves the calculation of a ratio instead of absolute values. Therefore, InSAR applications are not a typical example of monopulse techniques since in InSAR absolute phase differences play an important role. The typical monopulse ratio of radar systems is a complex-valued fraction of complex valued sum and difference signals as recorded by the system with

$$\Sigma = |\Sigma| \cdot e^{j\phi_\Sigma} \quad (4.6)$$

and

$$\Delta = |\Delta| \cdot e^{j\phi_\Delta} \quad (4.7)$$

where $|\cdot|$ is the amplitude and ϕ is the phase of signals. The monopulse ratio is defined as

$$\frac{\Delta}{\Sigma} = \frac{|\Delta|}{|\Sigma|} \cdot e^{j(\phi_\Delta - \phi_\Sigma)}. \quad (4.8)$$

For an ideal system, the phase difference between sum and difference signals of a static target is equal to zero as

$$\phi_\Delta - \phi_\Sigma \equiv 0 \quad (4.9)$$

whereas this may not be the case for a real system. In a real amplitude-comparison system, the feed horns are separated physically by a small distance, and they show a constant phase offset from each other. In a real phase-comparison system, the antennas may not be aligned exactly, resulting again in a constant phase offset. Additionally, signal interference, noise and non-pointlike targets will add to phase disturbances.

The ratio between Σ and Δ from (4.8) contains the complete information on the aspect angle of a target in one dimension. With Δ_{az} and Δ_{el} from (4.2) and (4.3) two dimensions are available. The third dimension may be obtained from the radar two-way signal delay to the target. Additionally, there would be the possibility to use the difference signal from the diagonal horns of an amplitude-comparison monopulse system with a square of four horns. However, according to chapter 3.1 of [124], the difference channels do not carry information that may be easily exploited.

The characteristics of the monopulse ratios over all possible target aspect angles φ is called the monopulse curve. If we envision the illustration in Fig. 4.5, we can define the intensity of signal amplitudes reflected from a target in the beams $\mathbb{A} + \mathbb{B}$ and $\mathbb{C} + \mathbb{D}$ as intensities with a $\sin(x)/x$ pattern. They may be defined as

$$s_1(\varphi) = \mathbb{A} + \mathbb{B} = \frac{\sin(\varphi - \varphi_0)}{\varphi - \varphi_0} \quad (4.10)$$

for the first beam and

$$s_2(\varphi) = \mathbb{C} + \mathbb{D} = \frac{\sin(\varphi + \varphi_0)}{\varphi + \varphi_0} \quad (4.11)$$

for the second beam where $2\varphi_0$ is the squint angle between the beams as introduced in Fig. 4.3(a). With (4.8) we receive the monopulse channels

$$\begin{aligned} \Sigma(\varphi) &= s_1 + s_2 \\ &= \frac{\sin(\varphi - \varphi_0)}{\varphi - \varphi_0} + \frac{\sin(\varphi + \varphi_0)}{\varphi + \varphi_0} \end{aligned} \quad (4.12)$$

and

$$\begin{aligned} \Delta(\varphi) &= s_1 - s_2 \\ &= \frac{\sin(\varphi - \varphi_0)}{\varphi - \varphi_0} - \frac{\sin(\varphi + \varphi_0)}{\varphi + \varphi_0}. \end{aligned} \quad (4.13)$$

In the left column of plots in Fig. 4.6, the normalized signal intensities of signals are shown in the first row as coming from physical antenna beams as described in (4.10) and (4.11). The squint angle between the two beams is given with $\varphi_0 = \pi/20$, an example value corresponding to a small angle. In the middle row, the monopulse channels as given in (4.12) and (4.13) are plotted. Finally, the bottom row shows the resulting monopulse curve

$$M(\varphi) = \frac{\Delta(\varphi)}{\Sigma(\varphi)} \quad (4.14)$$

from the monopulse ratio of (4.8) for all target aspect angles. Each value on this curve can be attributed to a single target aspect angle. In addition, we note the correct definition of zero phase difference in (4.9).

Equally, the top plot in the right column of Fig. 4.6 shows signal intensities of physical beams with a large squint angle of $\varphi_0 = \pi/4$. The middle row shows the plotted monopulse

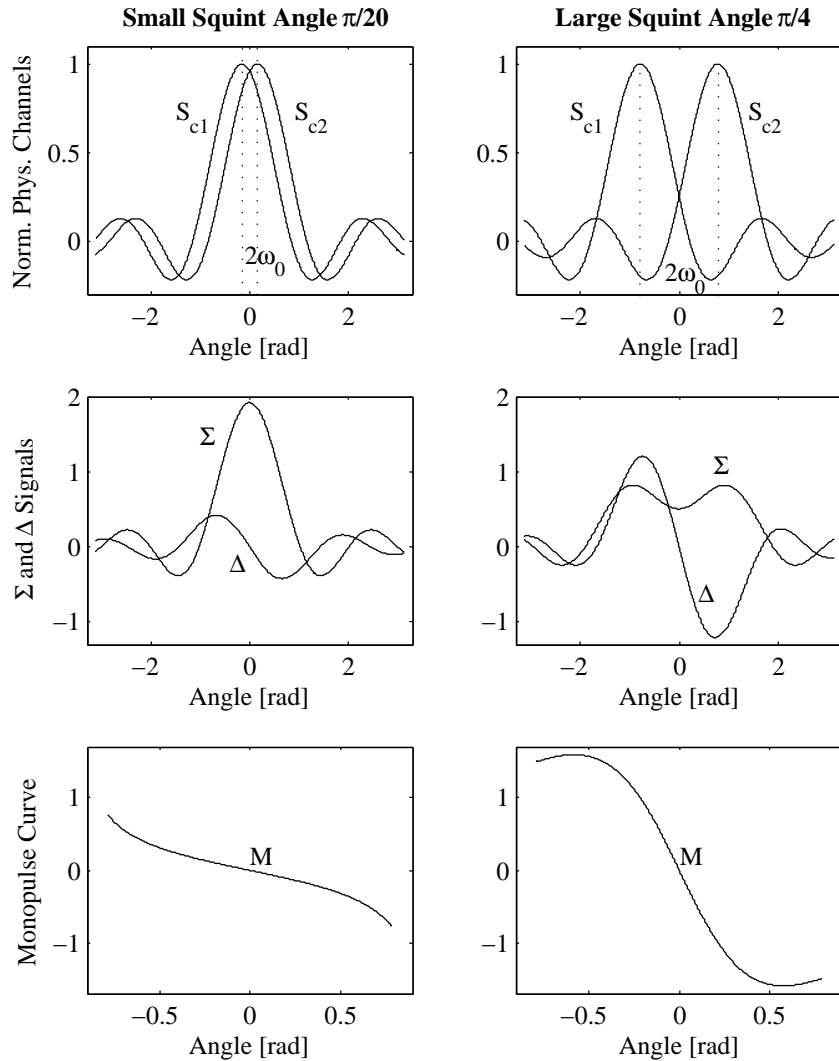


Fig. 4.6: Theoretical monopulse signals of a tracking radar — left: normalized physical channels, middle: recorded monopulse signals Σ and Δ , right: monopulse curve M .

Σ and Δ channels and the bottom row the resulting monopulse curve. Such a large squint angle serves as an extreme example. We see how the curve M features a much steeper slope than in the left column. This allows for a much finer resolution of small target aspect angles with the drawback that larger aspect angles cannot be resolved at all (the slope is too flat or the monopulse ratio is even ambiguous for certain values). A further drawback is a reduced target detection because of a lower concentration of the energy in the sum beam; after all the beam is strongest and most narrow with a squint of $\varphi_0 = 0$.

Further considerations about the squint angle are discussed in chapter 6.4 of [124].

4.2 Monopulse SAR

A monopulse SAR, just as any monopulse radar, has a sum signal Σ and multiple isochronous difference signals Δ . They are the result of two, four or more separate channels transmitting the same radio signal at the same time (monopulse), but receiving ground return echoes independently. While Σ is the sum signal of echoes from all channels, Δ is formed from the differences thereof. While in a tracking radar, these differences in amplitude as well as phase come from different target aspect angles, in SAR they are additionally disturbed by moving targets. The disturbances are caused by angle-dependent Doppler frequency shifts. Fig. 4.7 shows a schematic view of a monopulse system with four channels \mathbb{A} , \mathbb{B} , \mathbb{C} , and \mathbb{D} . In (a) the difference signal will be equal to zero, meaning a target at boresight while (b) and (c) show targets that are displaced in either azimuth or elevation. As such, it is closely related to Fig. 4.5 in the previous Chapter 4.1.2. While for a tracking radar, using monopulse, these off-center signals may be translated directly into a correction angle as given in (4.14), for a SAR, this is equal to a Doppler frequency behavior in the signals that is different from static clutter as explained in the following.

Measurable frequency shifts in a mmW SAR are only present in the Doppler domain (target displacement in azimuth) and not in the range domain (elevation) where the difference in magnitude between carrier frequency and Doppler shift is very large [30]. Hence, the elevation difference signal Δ_{el} does not play any important role and we will ignore it in the following. This means that a situation as in Fig. 4.7(c) does not appear in a monopulse SAR, and when referring to Δ , we will always mean the azimuth difference Δ_{az} .

Once we form the signal monopulse ratio

$$\text{MPR} = \frac{\Delta}{\Sigma} \quad (4.15)$$

we will get zero for all boresight echoes of static targets of zero Doppler frequency, a distinct monopulse curve M from all other echoes as a function of Doppler frequency, and moving targets deviating from this curve.

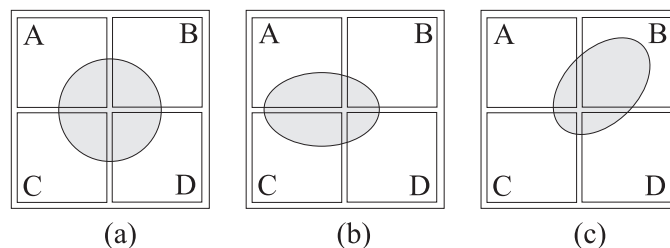


Fig. 4.7: Monopulse concept with a target seen by four independent receive channels A to D . In (a) the target is at boresight, in (b) and (c) it is displaced.

4.2.1 Amplitude-Comparison Monopulse mmW SAR

In Chapter 4.1.1, we mentioned that there are two different kinds of monopulse radars: amplitude-comparison and phase-comparison monopulse. While the idea of phase-comparison monopulse is commonly used in InSAR applications, mmW SAR systems must rely on amplitude-comparison monopulse because the physical baseline length B becomes very small and hard to be practically realizable for GMTI applications. For example, measurements of radial target velocities \hat{v} from 5 to 20 m/s at a wavelength λ of 4 mm would result in a baseline of only between 4 and 1 cm as calculated using

$$B = \frac{\lambda v_s}{2 \hat{v}} \quad (4.16)$$

and assuming an airborne SAR platform velocity in azimuth v_s of 100 m/s. (4.16) results under the assumption of a phase difference between physical channels equal to $\lambda/2$. The time difference between the antenna phase centers at the same position is $t = B/v_s$ and during that time, a target will move a distance $\hat{v} \cdot t$ equal to $\lambda/2$.

When using an ATI processing approach as described in Chapter 2.5.2, such closely spaced receive channels will probably interfere with each other. Amplitude-comparison monopulse does not put any such restriction on system design and neither does monopulse processing require highly independent receive channels.

4.2.2 The MEMPHIS SAR System

The configuration of MEMPHIS as described in [1] permits an amplitude-comparison monopulse mode, using a setup as described in Fig. 4.7 to combine the signals from four independent horns arranged in a square. Ideally, the signals share a common phase center, but since the individual horns are separated locally from each other by a short distance, this is practically not completely accurate, and we will also get a small constant phase difference between channels for static targets in addition to those phase differences caused by target movement.

The system operates simultaneously at carrier frequencies of 35 and 94 GHz with two independent monopulse antennas and standard chirped signals of 200 MHz bandwidth (0.75 m sample resolution) and a PRF of 1700 Hz for each antenna. Since the Doppler frequency of a target moving with radial velocity, \hat{v} , is given by (3.1) and ambiguous as stated in (3.2) we may receive unambiguous radial velocity measurements of up to 7.28 m/s for $f_d \leq \text{PRF}$ at 35 GHz if the target movement direction is known and ± 3.64 m/s otherwise. At 94 GHz, the unambiguous velocity limit at 1700 Hz PRF is 2.71 m/s or ± 1.35 m/s. All higher radial target velocities are ambiguous within the Doppler spectrum.

A detailed system description is given in Appendix A.

4.3 Dual-Frequency Information

4.3.1 Theory

Ambiguous velocity measurements and, closely related blind target speeds, are two important issues that often arise when looking at ground moving targets with high frequency SAR systems. Velocity ambiguities are due to target Doppler frequency shifts outside of the PRF and hence are aliased. Blind speeds are a special case where radial target speeds are aliased to a 0 Hz Doppler shift. Their effects have been discussed in Chapter 3.5.1.

First reports about exploiting dual-frequency radar to resolve Doppler ambiguities date back more than 35 years [131]. The method is to resolve Doppler shifts that are multiples of the PRF for one carrier frequency by using a second frequency where the Doppler shifts are a different multiple of the same PRF and aliased to a different value [132]. Hence, the problem reduces to a matter of the least common multiple. Applications for dual-frequency radar range from detection of moving targets in the presence of ground clutter to wind and storm measurements in meteorology and topographic height extraction in InSAR. Derivations of the principle include everything from dual-PRF systems [133] to dual-baseline InSAR [134].

If applying the dual-frequency technique to SAR GMTI, we are able to increase the unambiguous velocity range using the theory of least common multiples. Let us set $f_d > \text{PRF}$ in (3.1), and we get a new dual-frequency condition for Doppler ambiguities given as

$$\text{PRF} < \frac{2\hat{v}}{\text{lcm}(\lambda_1, \lambda_2)} \quad (4.17)$$

where we make use of both carrier wavelengths λ_1 and λ_2 of a dual-frequency system. lcm is defined as the least common multiple between two values. Unfortunately, least common multiples are only defined for integer values. λ_1 and λ_2 , however, will almost never be integer values in most dual-frequency SAR systems. The solution is to define the precision of such a system. Let us say that we trust a SAR to be precise up to x decimal digits of its wavelength in meters and we may define

$$\text{PRF} < \frac{2 \cdot \hat{v} \cdot 10^x}{\text{lcm}([\lambda_1 \cdot 10^x], [\lambda_2 \cdot 10^x])} \quad (4.18)$$

where $[\]$ means the nearest integer. Hence, we just expand the fractions and round off the accuracy of velocity measurements for our system.

As an example, let us use the system parameters of MEMPHIS. At 35 GHz, we have a wavelength of $\lambda_1 = 0.008571$ m and at 94 GHz one of $\lambda_2 = 0.003191$ m. If we want three digits in the wavelength to be significant, we have to set x equal to 5. For a system PRF of 1700 Hz in (4.18), we get a maximum unambiguous radial target velocity \hat{v} of 2323.7 m/s since $\text{lcm}(\lambda_1 \cdot 10^5, \lambda_2 \cdot 10^5) = \text{lcm}(857, 319)$ m = 273,383 m. If we restrain ourselves to a lower system precision of two significant digits for the wavelength ($x = 4$),

we get $\hat{v} = 116.9$ m/s (because $lcm(86, 32)$ m = 1376 m) which is still much larger than the unambiguous velocities for a single frequency obtained in Chapter 4.2.2.

From a practical point of view, we may define a system of linear equations for a dual-frequency SAR with wavelengths λ_1 and λ_2 and measured, *ambiguous* target Doppler shifts f_{d1} and f_{d2} .

$$\begin{aligned} f_{d1} &= \frac{2\hat{v}}{\lambda_1} - m \cdot \text{PRF} && \text{for all } m \in \mathbb{Z} \\ f_{d2} &= \frac{2\hat{v}}{\lambda_2} - n \cdot \text{PRF} && \text{for all } n \in \mathbb{Z} \end{aligned} \quad (4.19)$$

Of course, this system is underdetermined with unknown true radial velocity \hat{v} and ambiguities m and n . If we assume (4.18) to be true, the system is solvable by adding (4.18) as a constraint to (4.19), depending on the system accuracy indicated by x .

This system accuracy indicated by x may be verified. Since \hat{v} in the two equations of (4.19) may in practice not be the same measured value but rather \hat{v}_1 and \hat{v}_2 , potential discrepancies between ambiguity-resolved radial target velocities \hat{v}_1 measured at λ_1 and \hat{v}_2 at λ_2 result in a precision indicator $\Delta\epsilon$ given as

$$\Delta\epsilon = |\hat{v}_1 - \hat{v}_2|. \quad (4.20)$$

If $\Delta\epsilon$ is considerably larger than the system accuracy, we need to lower x .

4.3.2 Differences in SAR Imagery

Different ambiguous Doppler shifts f_{d1} and f_{d2} caused by moving targets in dual-frequency SAR cause differences in the focused SAR images. To illustrate this, let us look at a dual-frequency image pair of real data. In June 2004, a GMTI experiment with the MEMPHIS SAR system was realized on the runway of the airfield in Emmen, Switzerland. In this experiment, five Puch all-purpose vehicles were used as targets, with T_1 to T_3 at a nominally constant speed of 15 m/s and T_4 and T_5 at 10 m/s along the runway. Thus, they formed two independent small convoys. The front vehicle of either convoy (T_1, T_4) was equipped with a corner reflector to increase signal reception in the SAR. Two additional corner reflectors R_1 and R_2 were placed on the runway, serving as static reference targets.

The runway was imaged by MEMPHIS at 35 and 94 GHz simultaneously, with 200 MHz signal bandwidth, and a PRF of 1700 Hz. Fig. 4.8 shows the 750 m wide and focused Σ signal image at 35 GHz with all targets and the corner reflectors. The targets were moving from left to right, away from the SAR sensor and are vertically displaced in the image (in azimuth). Note that the targets moving more slowly (T_4, T_5) are actually displaced further away from their true position and in the other direction in the SAR image than

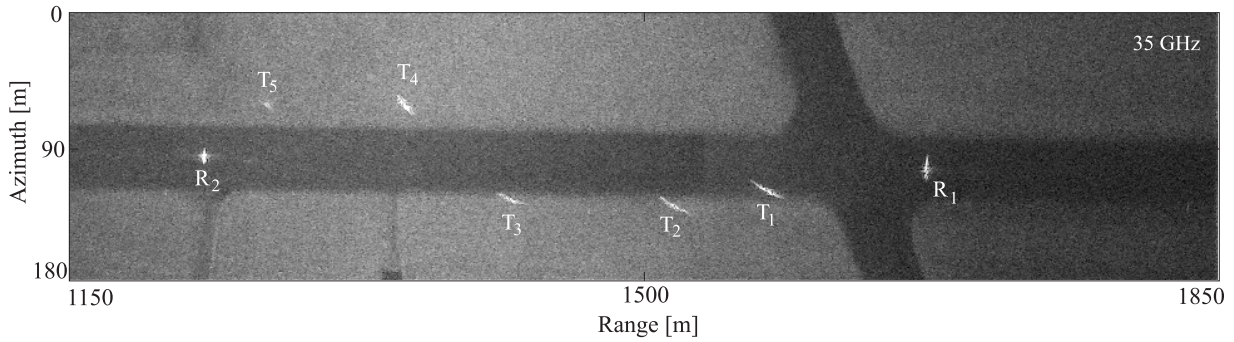


Fig. 4.8: Focused 35 GHz SAR image of an airfield runway. The image dimensions are $750 \times 150 \text{ m}^2$ with a resolution of 0.75 m. The misplaced targets T_1 to T_5 are moving to the right. The static corner reflectors are marked as R_1 and R_2 .

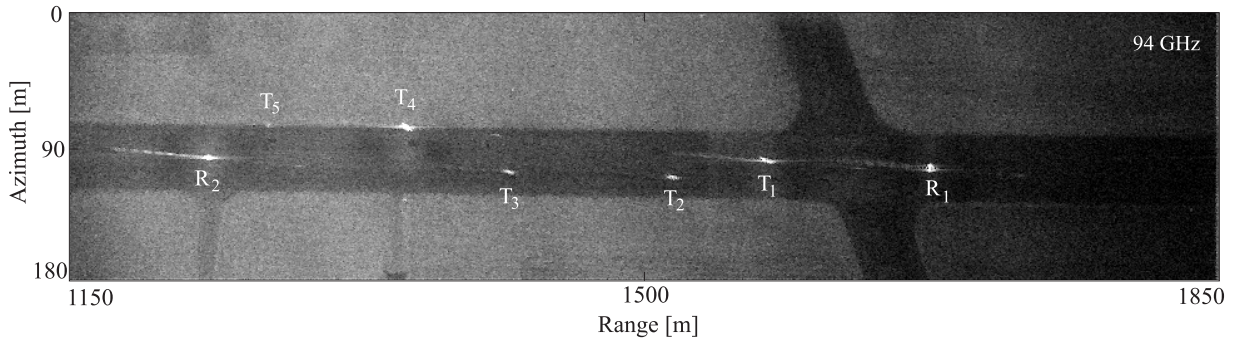


Fig. 4.9: Focused 94 GHz SAR image recorded simultaneously with the one in Fig. 4.8. Note how the moving targets T_1 to T_5 are misplaced differently than at 35 GHz because of different Doppler shifts.

the ones moving more quickly (T_1 to T_3). This is exactly what may happen due to the limited PRF and aliasing in the Doppler spectrum implied by (3.2).

In Fig. 4.9, the focused Σ signal image at 94 GHz is shown as a comparison to Fig. 4.8. Note how the moving targets experience a different azimuth displacement than at 35 GHz. This variable shift at different carrier frequencies may even be exploited by applying change detection to the two images. One has to keep in mind, though, that objects may have different backscattering characteristics at different frequencies.

4.4 Dual-Frequency GMTI

Independently of whether one or two carrier frequencies are available, GMTI is always possible for monopulse SAR at a single frequency—just not with unambiguous velocity determination. We developed the following $\Sigma\Delta$ algorithm to automatically indicate moving targets, get an ambiguous velocity estimation, and correct their position shifts in the SAR image. For the resolving of the true radial target velocity we are relying on (4.18)

and the dual-frequency information.

4.4.1 Theory

While we have distinguished between amplitude- and phase-comparison monopulse methods in Chapter 4.2.1, the data processing approach may be the same for both. Despite the misleading name, we do neither look at amplitudes nor phases in monopulse processing, but always at the complex ratios Δ/Σ . Hence, the theory is exactly the same as for general monopulse radar, and we may define the SAR sum signal as in (4.6) and the SAR difference signal as in (4.7) to receive the complex monopulse ratio

$$\text{MPR} = \frac{\Delta}{\Sigma} = \frac{|\Delta|}{|\Sigma|} \cdot e^{j(\phi_{\Delta} - \phi_{\Sigma})}. \quad (4.21)$$

As in general monopulse radar, the phase difference is ideally equal to zero

$$\phi_{\Delta_{SAR}} - \phi_{\Sigma_{SAR}} \equiv 0. \quad (4.22)$$

However, (4.22) will most probably not be true for a real system because of physical channel separation and multiple feed horn phase centers.

Specific to SAR, there are deviations from the general monopulse radar processing techniques described in chapter 7 of [124]. We look at the processed single look complex signals $S_c(r, \omega_d)$ in the range-Doppler domain. The transformations from the received echo signal $s(t, z)$ at the antenna to the processed SAR image $s_c(r, z)$ and its equivalent in the range-Doppler domain, $S_c(r, \omega_d)$, is

$$s(t, z) \xrightarrow{\textcircled{1}} s_c(r, z) \xrightarrow{\textcircled{2}} S_c(r, \omega_d) \quad (4.23)$$

where t is the fast time, r and z coordinates in range and azimuth and ω_d the Doppler frequency. $\textcircled{1}$ stands for the SAR processing of raw data to a single look complex image (e. g. [23]). $\textcircled{2}$ is the transformation into the range-Doppler domain given by the Fourier transform as

$$S_c(r, \omega_d) = \int_{-\infty}^{\infty} s_c(r, z) e^{-j\omega_d z} dz. \quad (4.24)$$

In the following, we calculate the monopulse ratio Δ/Σ for a SAR signal in the range-Doppler domain. Therefore, we do not assume a standard $\sin x/x$ radar backscattering intensity of the physical channels (e. g. [7]), but look at the Doppler frequency distribution at each range bin r as a standardized Gaussian distribution curve with a half-power frequency ω_p and a normalization constant $\nu = 1/\omega_p$. Because the phase difference between the channels is zero, the monopulse ratio can be formed by the signal amplitudes spectra. We assume that the influence of the range, r , on the monopulse ratio is negligible because of small image strips at large slant range distances. Hence, we define the image azimuth spectrum amplitude of the physical antenna channels independently from r as

$$|S_{c1}(\omega_d)| = e^{-\nu^2(\omega_d + \omega_0)^2} \quad (4.25)$$

and

$$|S_{c2}(\omega_d)| = e^{-\nu^2(\omega_d - \omega_0)^2}. \quad (4.26)$$

ω_0 is the Doppler frequency shift of the channels resulting from the squinted antenna beams with

$$\omega_0 = \frac{4\pi v_s \sin \varphi_0}{\lambda} \quad (4.27)$$

between the monopulse beams as shown in Fig. 4.3(a). We get the $|\Sigma|$ and $|\Delta|$ signals

$$\begin{aligned} |\Sigma(\omega_d)| &= |S_{c1}| + |S_{c2}| \\ &= e^{-\nu^2(\omega_d + \omega_0)^2} + e^{-\nu^2(\omega_d - \omega_0)^2} \\ &= e^{-\nu^2\omega_d^2 - \nu^2\omega_0^2} \left(e^{2\nu^2\omega_d\omega_0} + e^{-2\nu^2\omega_d\omega_0} \right) \end{aligned} \quad (4.28)$$

and

$$\begin{aligned} |\Delta(\omega_d)| &= |S_{c1}| - |S_{c2}| \\ &= e^{-\nu^2(\omega_d + \omega_0)^2} - e^{-\nu^2(\omega_d - \omega_0)^2} \\ &= e^{-\nu^2\omega_d^2 - \nu^2\omega_0^2} \left(e^{2\nu^2\omega_d\omega_0} - e^{-2\nu^2\omega_d\omega_0} \right). \end{aligned} \quad (4.29)$$

Considering the properties of the hyperbolic functions $\sinh(x) = \frac{1}{2}(e^x - e^{-x})$ and $\cosh(x) = \frac{1}{2}(e^x + e^{-x})$ we get

$$|\Sigma(\omega_d)| = e^{-\nu^2(\omega_d^2 + \omega_0^2)} \cdot 2 \cosh(2\nu^2\omega_d\omega_0) \quad (4.30)$$

and

$$|\Delta(\omega_d)| = e^{-\nu^2(\omega_d^2 + \omega_0^2)} \cdot 2 \sinh(2\nu^2\omega_d\omega_0). \quad (4.31)$$

The ideal monopulse curve of all Doppler frequencies from the static ground scene in a SAR may thus be described mathematically by a hyperbolic tangent as

$$M(\omega_d) = \frac{|\Delta(\omega_d)|}{|\Sigma(\omega_d)|} = \tanh(2\nu^2\omega_d\omega_0). \quad (4.32)$$

In Fig. 4.10, the physical channels given by (4.25) and (4.26) are plotted on the left, analogously to the situation at the top of Fig. 4.3, while the sum and difference signals of (4.28) and (4.29) are shown in the center and the resulting monopulse curve of (4.32) on the right. For this example, a total spectrum from -850 to 850 Hz was chosen corresponding to the PRF of MEMPHIS with ω_p equal to 300 s^{-1} and ω_0 to 100 s^{-1} . The slope of the monopulse curve depends on ω_0 and is thus directly related to the angle φ_0 between the physical channels, as stated in (4.27). The larger φ_0 gets, the steeper the slope of Δ/Σ . This may be of an advantage when measuring very accurate target velocities with a small Doppler shift compared to the total signal spectrum. For a mmW SAR, however, the target Doppler shift will become large because of the high carrier frequency, and a slight slope enables the exact measurement of a larger range of target velocities.

A moving target deviates from the monopulse curve of the static scene with the magnitude of deviation depending on the target's radial velocity component. This makes a

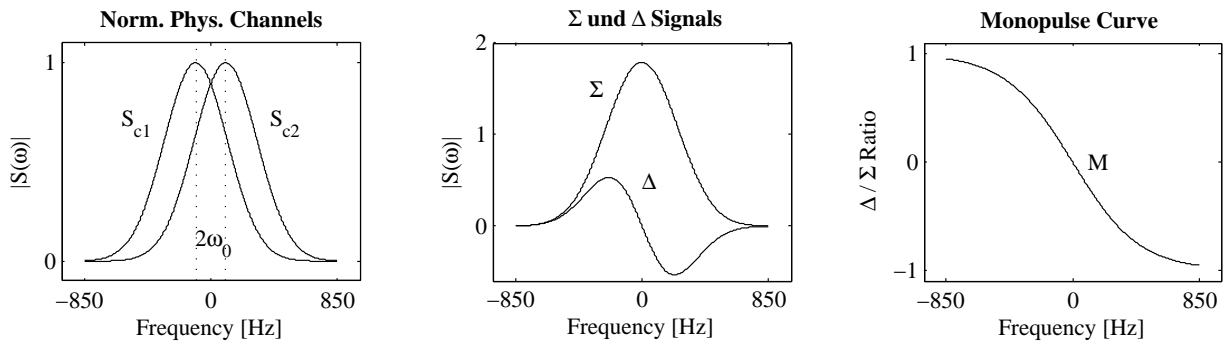


Fig. 4.10: Theoretical Doppler spectra of monopulse SAR — left: normalized physical channels S_{c1} and S_{c2} , middle: recorded monopulse signals of Σ and Δ , right: monopulse curve M .

moving target clearly discernible in the monopulse curve, regardless of whether the target's Doppler frequencies are inside or outside the clutter spectrum. Additionally, the monopulse curve of the static scene makes it possible to determine the Doppler shift of a target and therefore allows a correction of the azimuth displacement and estimation of the radial velocity.

4.4.2 Endo- and Exo-Clutter Targets

Monopulse processing includes the estimation of a monopulse curve from the static clutter background. After this estimation, single monopulse ratios may be compared to this curve and a decision is possible whether a ratio fits the curve (indication for a static target) or deviates from it (indication for a moving target).

As an illustrative example of the principle, Fig. 4.11 presents two moving targets in clutter imaged with MEMHPIS in a special radar modus with twice the PRF needed for normal SAR applications. Twice the PRF needed means that all clutter from static ground returns is confined to the inner half of the azimuth spectrum [10]. A moving target causing an additional Doppler shift because of its radial velocity may now be located inside this clutter spectrum, or it may be shifted outside of the clutter.

In all four plots of the figure, the typical monopulse curve is visible as a black line in the form of a hyperbolic tangent as it was estimated from the spectral monopulse information of the complete scene.

In the left column of Fig. 4.11, a target moving at 15 m/s is located inside the clutter spectrum as visible from the monopulse ratios of the range bin including the target. In the top plot, the target and clutter spectrum are combined. Such a target may be made clearly visible with monopulse processing and clutter filtering as described in the following Chapter 4.4.3. The bottom plot shows the resulting spectrum of the moving target.

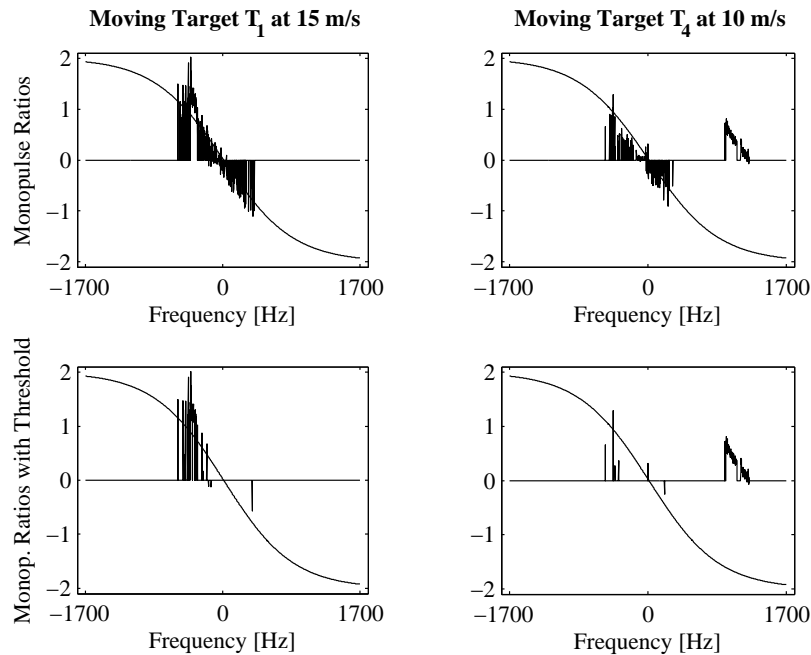


Fig. 4.11: The left column shows an endo-clutter target inside the monopulse processed clutter spectrum (top) and after removal of the static clutter (bottom). In the right column an exocutter target is shown, again including the static clutter (top) and after removal (bottom). The SAR PRF equals 3400 Hz.

In the right column of Fig. 4.11, a target moving at 10 m/s is Doppler shifted and aliased to appear outside of the static clutter spectrum. It is clearly discernible at the far right of the spectral plot in the top image. In the bottom image, the static clutter is removed with monopulse processing. However, a simple approach with a bandpass filter could have removed the inner half of the spectrum leaving only the exo-clutter moving target. This technique is the standard procedure for pure GMTI radars. However, SAR systems almost never use a PRF that is much higher than the Doppler frequencies of the clutter returns and moving targets will mostly be endo-clutter.

4.4.3 Implementational Aspects

To be able to estimate an accurate monopulse curve $M(\omega_d)$ as defined in (4.32) from given sensor Σ and Δ signals in all samples (r, ω_d) and to identify moving targets, we perform the following steps which include stochastic modeling of $M(\omega_d)$. All these steps are executed on blocks of data split in the azimuth direction to avoid Doppler information from a too large sub-scene which might include multiple moving targets per range bin:

1. Because signal and SAR speckle noise may influence monopulse processing, we define an amplitude threshold T_A and consider only samples where the sum signal $|\Sigma(r, \omega_d)|$

is larger than the threshold with respect to the average clutter return amplitude \bar{A} in dB as

$$|\Sigma(r, \omega_d)| > \bar{A} \cdot 10^{T_A/20}. \quad (4.33)$$

This amplitude thresholding returns the noise-reduced Σ and Δ channel amplitudes as shown on the left of Fig. 4.12 for an example data set with MEMPHIS. Note that the negative part of the amplitude of the difference channel, $|\Delta|$, is mapped to positive values in contrast to the curve in Fig. 4.10.

2. We calculate and store the complex monopulse ratios

$$\text{MPR}(r, \omega_d) = \Delta(r, \omega_d)/\Sigma(r, \omega_d) \quad (4.34)$$

over the complete Doppler spectrum for all range bins. Then, we use only the real part of this ratio (assuming a phase difference between channels of 0 as in (4.22), see chapters 3 and 7 of [124]). The imaginary part is considered for a phase correction later in step 6.

3. Presuming independence of the monopulse ratio from range r , we calculate the mean values of $\text{MPR}(\omega_d)$ over all r .
4. As shown in (4.32), the monopulse curve $M(\omega_d)$ has the form of a hyperbolic tangent. To fit a curve $M(\omega_d)$ through all values $\text{MPR}(\omega_d)$, we assume a parameterization

$$M(\omega_d) = a \cdot \tanh(b\omega_d - c) \quad (4.35)$$

where a , b , and c are free parameters. An example is shown on the right side in Fig. 4.12.

5. We estimate a , b , and c through non-linear data modeling. A good technique is the Levenberg-Marquardt method in combination with singular value decomposition for

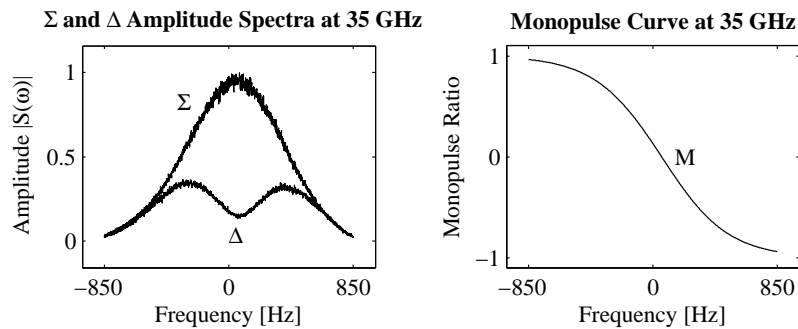


Fig. 4.12: Left: monopulse data Σ and Δ channels at 35 GHz for an example data set acquired with MEMPHIS. Note that the negative part of the amplitude of the difference channel, $|\Delta|$, is mapped to positive values. Right: estimated and parameterized monopulse curve M from the ratio Δ/Σ .

the solution of the sets of linear equations (compare chapter 15 of [135]). For the method to work, reasonable initial values of a , b , and c must be chosen. They may easily be determined from the theoretical monopulse curve of a given SAR sensor in Fig. 4.10.

6. As mentioned in Chapter 4.2.2, the individual receive channels of a monopulse system are separated locally from each other by a short distance, and we get a small constant phase difference between channels for static targets in addition to those phase differences caused by target movement. By estimating the imaginary monopulse ratios and their monopulse curve $M_{im}(\omega_d)$, we adjust the phase of all monopulse ratios through a multiplication of the complex Σ and Δ signals with $e^{-j\phi}$ where

$$\phi = \text{atan} \left(\frac{b_{im}}{b_{re}} \right) \quad (4.36)$$

and b_{re} , b_{im} are the b parameters of the real and imaginary monopulse curve of (4.35). Therefore, (4.36) represents the constant difference in the monopulse phase between the physical channels.

7. We estimate the monopulse curve again, now with the phase-corrected ratios.
8. Defining a monopulse threshold T_M , we ignore all ratios $\text{MPR}(r, \omega_d)$ that deviate less than the threshold from $M(\omega_d)$. Such a threshold may be defined in dB with the help of the standard deviation σ of the fitted monopulse curve $M(\omega_d)$ as

$$\left| \frac{\Delta(r, \omega_d)}{\Sigma(r, \omega_d)} - M(\omega_d) \right| < \sigma \cdot 10^{T_M/20}. \quad (4.37)$$

9. We determine the necessary frequency shift of all remaining signals presumed to be coming from moving targets. The frequency shifts may be directly translated into radial velocities \hat{v} by (3.1), and an azimuth position correction in the image becomes possible.

Note that more than one target in the same range bin may be present if the processed block size of images is set to be too large, complicating the algorithm because more than one Doppler shift must be extracted. This means that the parts in the Doppler spectrum after monopulse filtering have to be clustered in order to identify individual moving targets. Smaller block sizes may increase the adaptivity of the algorithm. However, if the block size is too small, estimation of the monopulse curve $M(\omega_d)$ may be inaccurate. The complete proposed algorithm is shown as a flowchart in Fig. 4.13.

For the results presented in the following Chapter 5 a block size of 2048 echoes was selected at both frequencies corresponding to slightly more than one second of data recording. No block contained more than one target. For targets appearing in more than one block, a target data buffer common to all blocks was used.

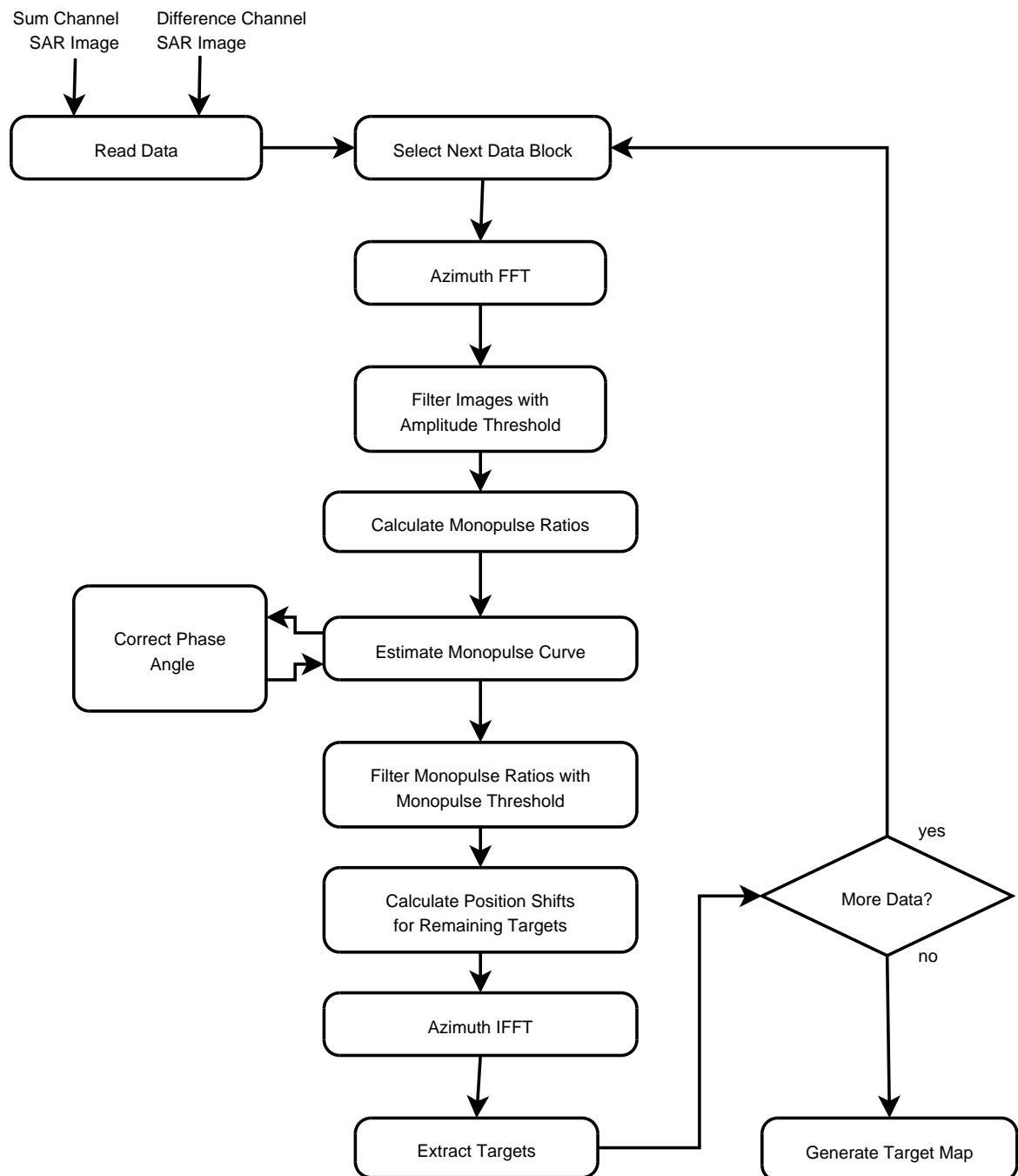


Fig. 4.13: GMTI algorithm that generates a moving target map from Σ and Δ channel SAR images of a scene.

The values for both T_A and T_M are sensor-specific and must be determined experimentally. For the experiments in the following Chapter 5, they were both set to 10 dB.

The presented algorithm is based on a theory assuming constant target velocity. Accelerations are ignored. They cause Doppler shifts in the monopulse ratio that are non-uniform and hard to correct in the spectrum. Fortunately, a small target dwell time of a mmW SAR with a small antenna divergence angle keeps target velocity variations during illumination by the radar at a minimum. This is shown by the experiment presented in Chapter 5.2.

One difficulty could be the Doppler centroid of the data. In Fig. 4.10, we have shown the theoretical Doppler spectra to be expected from a monopulse system. However, for real data, the signal peak of the sum channel may almost never be centered exactly at zero but shifted by the Doppler centroid caused by a radar azimuth look angle different from 90° . Additionally, the Doppler centroid shows a strong dependency on range, r , and often—considering the data focusing scheme—one on azimuth z , as well. A good estimation of Doppler centroid is needed to correct these shifts accurately before monopulse processing the data. Otherwise, correct estimation of the hyperbolic tangent will be impossible and static targets may be indicated as moving by the algorithm. Estimation of the Doppler centroid, especially at very high carrier frequencies such as for mmW SAR, is difficult and has to include navigational data as well as spectral estimation methods [12].

Chapter 5

Experimental Results with Dual Frequency GMTI

This chapter presents GMTI results achieved with the dual-frequency monopulse algorithm developed in the previous Chapter 4. Data from four different SAR experiments with MEMPHIS in Switzerland are used. The first and the last experiment were located at the airfield of Emmen. The first one, already introduced in Chapter 4.3.2 to explain GMTI algorithm details, was a controlled environment experiment with targets in low clutter and at constant speeds. It is presented in Chapter 5.1. The last one had its focus drawn towards special movements such as rotation and vibration and the detection of targets of opportunity, meaning arbitrary targets being imaged by the SAR by chance as shown in Chapter 5.4.

The second experiment mentioned above was conducted on a field path on the Mont Racine in western Switzerland. Therefore, targets with varying but slow speed on an uneven road are analyzed in Chapter 5.2. The influence of target velocity direction relative to the SAR sensor is discussed.

One more experiment was done for fast moving targets on a freeway. It is presented in Chapter 5.3. The site of the experiment was again located in western Switzerland, near a village called La Verrerie south of the city of Fribourg. The freeway imaged by the SAR was the A12 between Berne and Vevey.

5.1 Controlled Environment GMTI

A first MEMPHIS GMTI experiment was executed in June 2004. For this controlled environment experiment, five target vehicles T_1 to T_5 —Puch all-purpose vehicles mentioned in Chapter 4.3.2—were moving down the runway of the airfield in Emmen with their exact positions and velocities logged by GPS receivers at one second intervals. Post-measurement dGPS processing was used to increase position and velocity data to sub-meter accuracy. T_1 , T_2 , and T_3 were moving at 15 m/s on the lower side of the runway in Figs. 4.8 and 4.9



Fig. 5.1: Experiment on the airfield of Emmen. Five Puch all purpose vehicles are moving along the runway. Their positions and velocities are logged by dGPS.

while T_4 and T_5 drove with 10 m/s along the upper border to minimize the possibility of collision. A photograph during the experiment showing the five targets on the runway is given in Fig. 5.1.

Monopulse GMTI processing as described in Chapter 4.4 gives the spectral results shown in Fig. 5.2 for 35 GHz and in Fig. 5.3 for 94 GHz. Given are the spectra for the static reflector R_1 and targets T_1 moving at 15 m/s and T_4 at 10 m/s with $T_A = 10$ dB. The calculated monopulse ratios at the range bin of the reflector at the top left of the figure correspond very well to the estimated monopulse curve. At the bottom left, we see that no frequency remains in the spectrum after including a monopulse threshold $T_M = 10$ dB. However, the targets T_1 (middle) as well as T_4 (right) are clearly identified via monopulse processing. Their relative frequency shifts are easily discernible.

Figs. 5.4 and 5.5 show the outcome in the time domain of our described monopulse algorithm for 35 and 94 GHz, respectively. All signal parts found to be static by monopulse processing have been filtered out in the Doppler domain before inversely Fourier transforming the remaining signal back to the time domain. For orientation purposes, the airfield runway is outlined in the figures. Obviously, the target repositioning is as sensitive as the velocity estimation. An error in the velocity estimation of $\Delta v_r = 0.1$ m/s results in a position uncertainty of one meter as calculated in (3.3), assuming an aircraft velocity of $v_s = 100$ m/s and a range to the target of $R = 1000$ m.

All indicated targets appear in red and their calculated true ground positions in green. The resulting velocity components in range are listed in Table 5.1 and compared with calculated relative velocities between the sensor and the targets obtained from dGPS data. All targets are detected at 35 GHz while at 94 GHz, T_2 experienced a blind speed at the

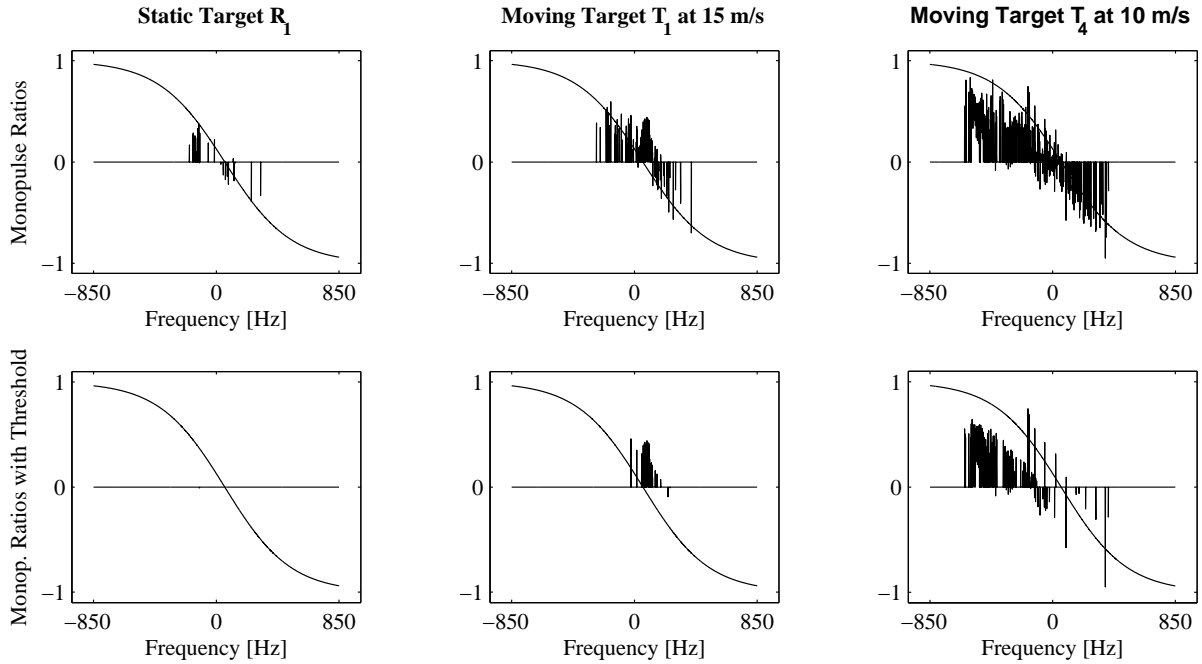


Fig. 5.2: Monopulse ratios at 35 GHz for the Emmen experiment before (top) and after (bottom) thresholding with T_M . Left: Ratios of a static reflector fit on the adaptively calculated monopulse curve. Middle: Thresholding of the range bin including T_1 and background clutter (top) leaves the indication of a target moving at 15 m/s (bottom). A positive Doppler shift is clearly discernible. Right: Indication of T_4 moving at 10 m/s and showing a negative Doppler shift when static clutter is removed.

time of illumination and the target intensity of T_5 is weak and disappears in the clutter. Even at 35 GHz, T_5 is very weak and barely indicated as a moving target. The resulting velocity estimation for T_5 is worse than that for the other targets. For T_1 to T_4 , velocity estimates from the monopulse processing agree very well with dGPS measurements with no more than 3% deviation, and displacement corrections show correct target positions.

In Table 5.1, we see how the velocity measurement ambiguities indicated by the factors m and n defined in (4.19) can be resolved by using the dual-frequency information. We solved the system of equations (compare columns 3 and 4 in Table 5.1) and assumed that the condition of the velocities being inside of the least common multiple velocity in (4.18) is fulfilled with $x = 4$. Obviously, we could not solve such a system for targets T_2 (blind speed at 94 GHz) and T_5 (weak signal at 94 GHz). For T_2 , the indication from the companion frequency at 35 GHz can be used to state a blind velocity as $0 + m \cdot 2.71$ m/s. However, this approach does not work for a target that is moving with a velocity different from a blind speed but with a weak echo, such as T_5 . There, the amplitude threshold of (4.33) or the monopulse threshold of (4.37) would have to be relaxed once a moving target has been detected in the companion frequency. With our a-priori knowledge from the dGPS measurements and by assuming two convoys of similar velocities, we filled in the

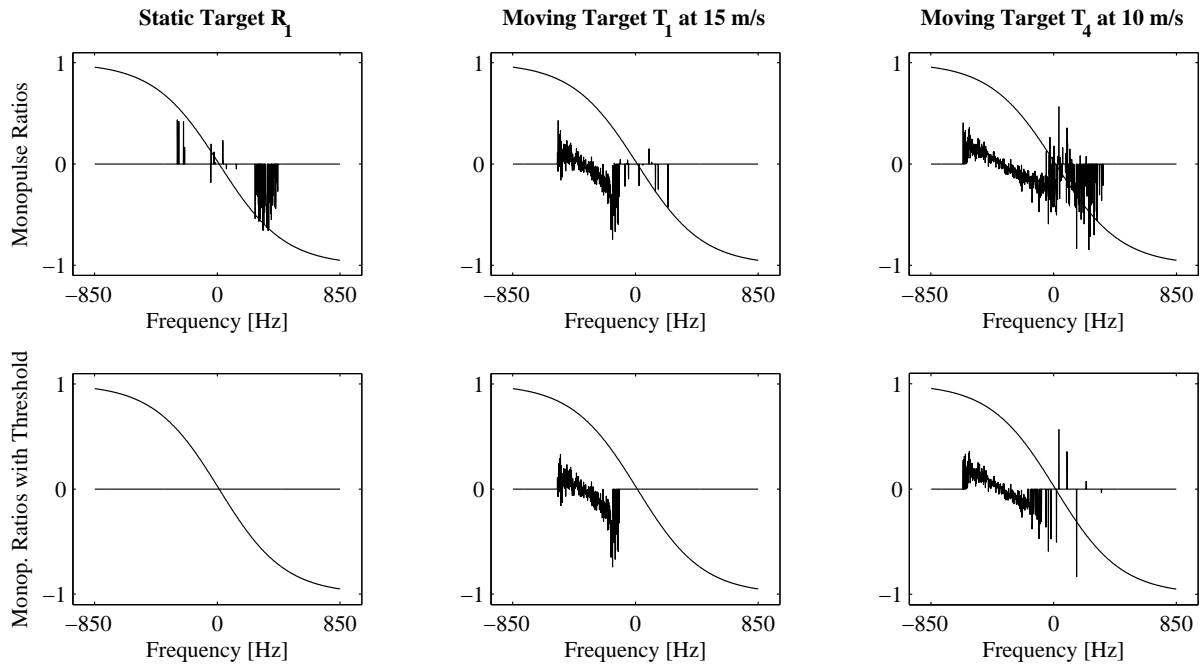


Fig. 5.3: Monopulse ratios at 94 GHz for the Emmen experiment before (top) and after (bottom) thresholding with T_M for the same targets at the same time as in Fig. 5.2. Left: Ratios of a static reflector fit on the adaptively calculated monopulse curve. Middle: Indication of T_1 moving at 15 m/s. Right: Indication of T_4 moving at 10 m/s.

corresponding ambiguity factor m in parentheses and obtained a good velocity estimate.

For targets T_1 , T_3 , and T_4 we could determine a mean dual-frequency velocity. The difference $\Delta\epsilon$ between the resulting ambiguity-resolved velocities at 35 and at 94 GHz is of the same order as that one between the SAR and GPS measurements, indicating that the GMTI algorithm worked fine at both frequencies.

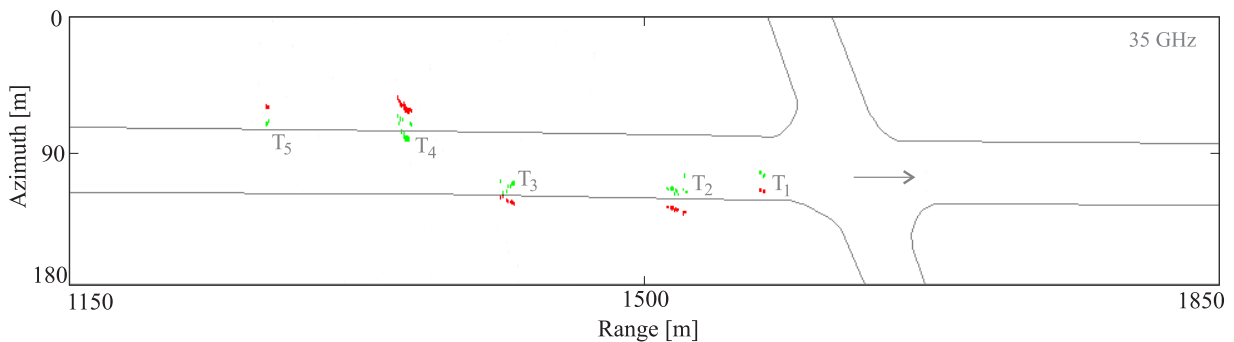


Fig. 5.4: Automatically indicated (red) and position-corrected (green) moving targets at 35 GHz carrier frequency. The static corner reflectors R_1 and R_2 have correctly disappeared.

Table 5.1: CONTROLLED ENVIRONMENT RESULTS (SEE FIGS. 5.4 AND 5.5): ABSOLUTE NOMINAL VALUES AND MEASURED RADIAL VELOCITIES OF MOVING TARGETS BY dGPS AND BY THE MEMPHIS DUAL-FREQUENCY MONOPULSE SAR SENSOR. NEGATIVE VALUES INDICATE A MOVEMENT AWAY FROM THE SAR. THE NUMBERS OF DOPPLER AMBIGUITIES m AND n ARE RESOLVED VIA LEAST COMMON MULTIPLES TO GET THE DUAL-FREQUENCY VELOCITY ESTIMATE. $\Delta\epsilon$ IS THE DIFFERENCE BETWEEN THE 35 AND 94 GHz VELOCITY MEASUREMENTS GIVEN BY (4.20).

Target	Nom. Velocity (ground) [m/s]	35 GHz SAR Vel (radial) [m/s]	94 GHz SAR Vel (radial) [m/s]	m	n	$\Delta\epsilon$ [m/s]	Dual-Freq SAR Vel (radial) [m/s]	dGPS Vel (radial) [m/s]	Δ SAR-GPS [m/s]
T_1	15	$0.57 + m \cdot 7.28$	$-0.64 + n \cdot 2.71$	-2	-5	0.2	-14.1	-14.4	0.3
T_2	15	$0.66 + m \cdot 7.28$	blind	(-2)	—	—	(-13.9)	-14.0	0.1
T_3	15	$0.73 + m \cdot 7.28$	$-0.46 + n \cdot 2.71$	-2	-5	0.2	-13.9	-14.2	0.3
T_4	10	$-1.05 + m \cdot 7.28$	$-0.58 + n \cdot 2.71$	-1	-3	0.4	-8.5	-8.8	0.3
T_5	10	$-0.64 + m \cdot 7.28$	too weak	(-1)	—	—	(-7.9)	-8.7	0.8

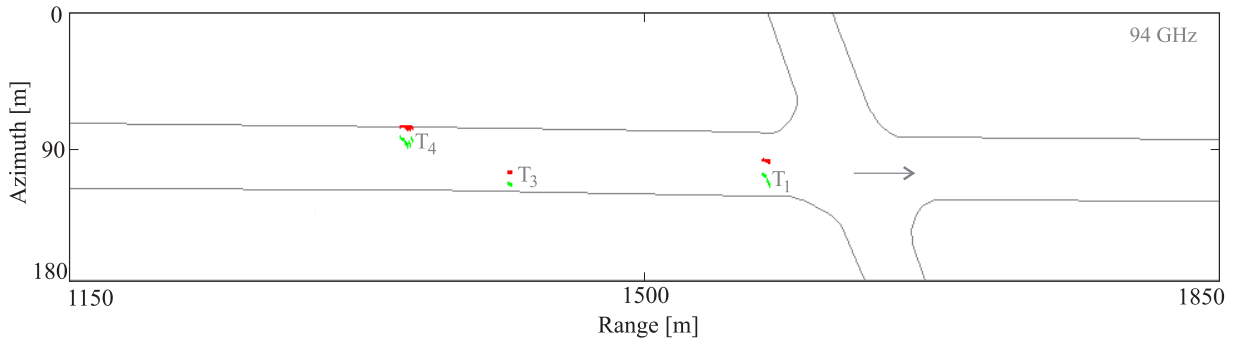


Fig. 5.5: Automatically indicated (red) and position-corrected (green) moving targets at 94 GHz carrier frequency. T_2 is moving with a blind speed while T_5 is too weak to be indicated.

5.2 Field Paths GMTI

The success of the experiment with five targets in the controlled environment of an airfield encouraged the attempt to test the capabilities of MEMPHIS for targets in a much more difficult environment in 2005. A 3 m wide field path running around the hilltop of Mont Racine northwest of Neuchâtel in western Switzerland was chosen. This path is sometimes twisted, sometimes straight and does not allow for a single, constant target velocity. Trees, rocks, and some huts are located in the immediate neighborhood of the path and the terrain is bumpy.

The same type of moving targets as on the airfield (see Chapter 5.1 above) was used. They are called T_6 , T_7 , and T_8 in the following. T_6 and T_8 were outfitted with corner reflectors and all three vehicles carried GPS equipment logging position and velocity. The target velocities were to be around 10 m/s, but were ultimately determined by path conditions and the drivers' discretion. Multiple SAR flights around the hill were planned, always with the knoll at the center. There, three reflectors R_4 , R_5 , and R_6 were positioned, looking perpendicular to the various planned flight tracks. As we will see, they are all three always visible in the recorded data, regardless of the look direction and serve as static reference targets.

In Fig. 5.6, the area of the experiment on the Mont Racine is shown. The view in the photograph is from the last of the three targets and shows the two front Puch as well as the SAR carrier platform in the top left corner.

Fig. 5.7 shows the focused SAR images of the field path at 35 and 94 GHz. These images have been processed with the monopulse GMTI algorithm presented in Chapter 4.4. Unlike the results from the airfield of the previous Chapter 5.1, the GMTI results are directly represented as color pixels in the SAR image. All signals found to be deviating from the monopulse curve $M(\omega_d)$ have been marked in the Doppler domain before separately inversely Fourier-transforming the static and non-static signals back into the time domain. This gives us the advantage of having the static information of the SAR image combined



Fig. 5.6: Experiment area on the Mont Racine. Three Puch all purpose vehicles are moving along a field path. Their positions and velocities are logged by dGPS.

with the moving target information. To give some more emphasis on small moving targets, their immediately neighboring pixels may be colored, too, as has been done in Fig. 5.7 and all following images of combined SAR and GMTI results.

In both, Fig. 5.7(a) and (b), the three static corner reflectors R_4 , R_5 , and R_6 are clearly visible. Since none of them is colored red, they have been correctly identified as static targets. The three moving targets T_6 to T_8 were moving towards the SAR sensor. At 35 GHz carrier frequency, the SAR image shows all three targets clearly. T_6 is moving at a greater angle relative to the sensor line of sight than the other two. Hence, its radial velocity is smaller, and its displacement in azimuth away from the path is less than for T_7 and T_8 . T_7 without a corner reflector shows a weaker target signature and its GMTI corrected position is not on the path but some meters south. If we look at the 94 GHz image in Fig. 5.7(b), we see that T_7 is not even indicated as a target. A closer analysis shows that the brightest returns from T_7 at 94 GHz are about 8 dB above the clutter level while the GMTI algorithm only considered targets of $T_A = 10$ dB and higher (see (4.33)). T_6 on the other hand, is not indicated at 94 GHz as a moving target even though its signature is very prominent. Since its signature lies exactly on the path, we deduce that it was moving at a blind speed in 94 GHz SAR. T_8 was detected as the sole moving target. Its corrected position is almost on the path.

Furthermore and only visible when enlarged in Fig. 5.8, the hut in front of T_6 shows traces of GMTI colors on its roof in 94 GHz SAR. This is an indication for either a movement or—as a hut is unlikely to have moving parts on its roof—a misregistration

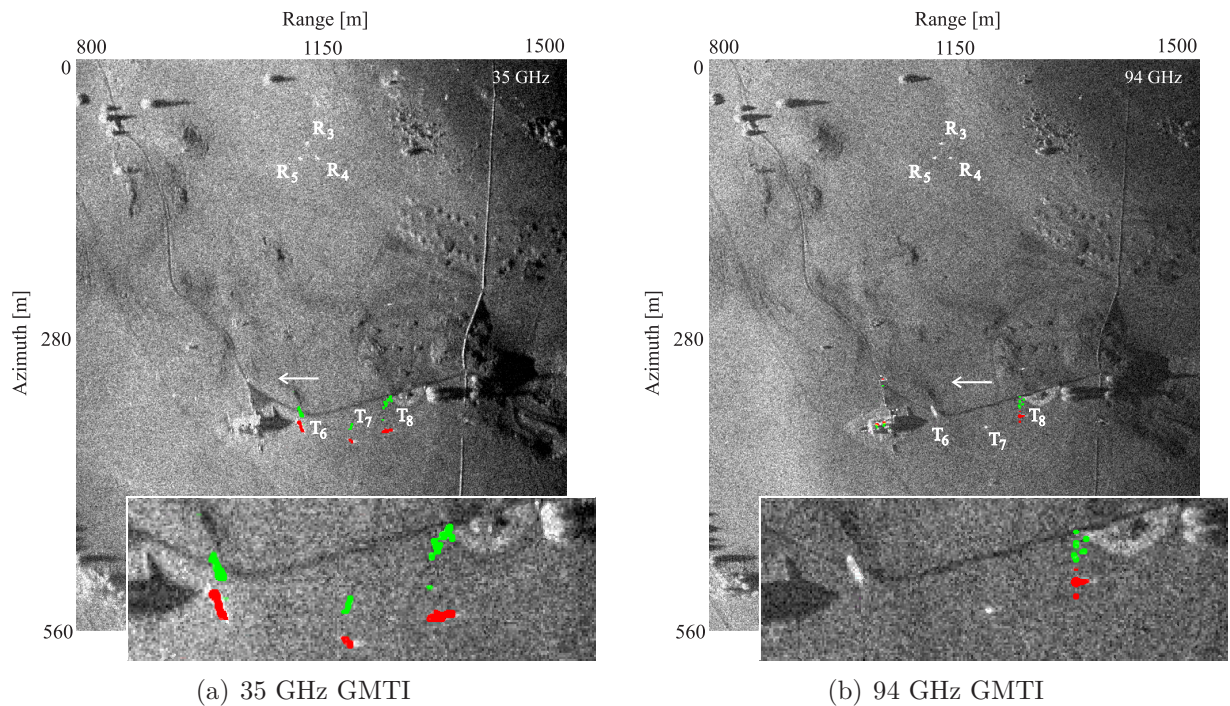


Fig. 5.7: Automatic indication of moving targets T_6 to T_8 , moving towards the SAR sensor, with detection (red) and position correction (green) done directly in the SAR image. The targets were moving on a field path. The image dimensions are $460 \times 540 \text{ m}^2$ with a resolution of 0.75 m. Enlarged at the bottom is the area of interest with the moving targets.

in the monopulse algorithm for this particular block of data, most likely coming from a Doppler centroid estimation of the data that is not accurate (Fig. 5.7(b) includes 6 processing blocks with individual monopulse curve estimations, see Chapter 4.4). The second assumption would be encouraged by the very small position correction on the hut roof targets, indicating a very slow movement that could come from a monopulse curve misfit. It would also explain why the corrected position of T_8 is not located on the path. The Doppler centroid at different data blocks, for example at the static corner reflectors in

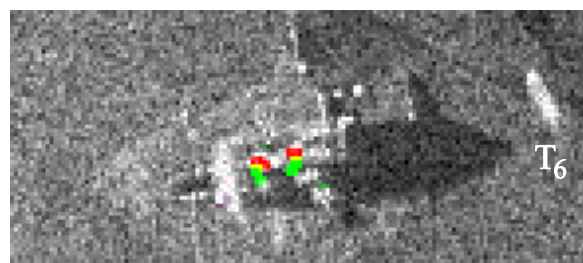


Fig. 5.8: Enlarged area of the hut in front of T_6 from Fig. 5.7(b). The 94 GHz GMTI processed result shows falsely indicated moving targets.

mid range, does not show any misregistration. Hence, another possibility may be that the range dependency of the Doppler centroid is not estimated correctly and the values are only inaccurate in near range. Most probable, however, is the assumption that metallic parts on the hut roof have saturated the SAR receive channels, resulting in incorrect phase recordings.

In Table 5.2, the target velocities are shown as evaluated by dGPS and by GMTI processing. Because T_7 is too weak and T_6 was moving at a blind speed in Fig. 5.7(b), their true radial dual-frequency velocity could only be calculated with the information from the dGPS data and have been put in parentheses. In addition, the data show that the two strong targets T_6 and T_8 have very precise velocity estimations compared with the dGPS data while the velocity of the weaker target T_7 could not be accurately estimated.

A second dual-frequency SAR imagery pair from the same experiment is shown in Fig. 5.9. The flight track was slightly different and the targets T_6 to T_8 were moving on a different section of the field path. This caused the constellation between SAR flight track and targets to be almost parallel, but in opposite directions. Such a constellation is the most difficult for a GMTI algorithm which is designed to detect radial velocities. However, as may be seen in the imagery and confirmed in Table 5.3, monopulse processing works

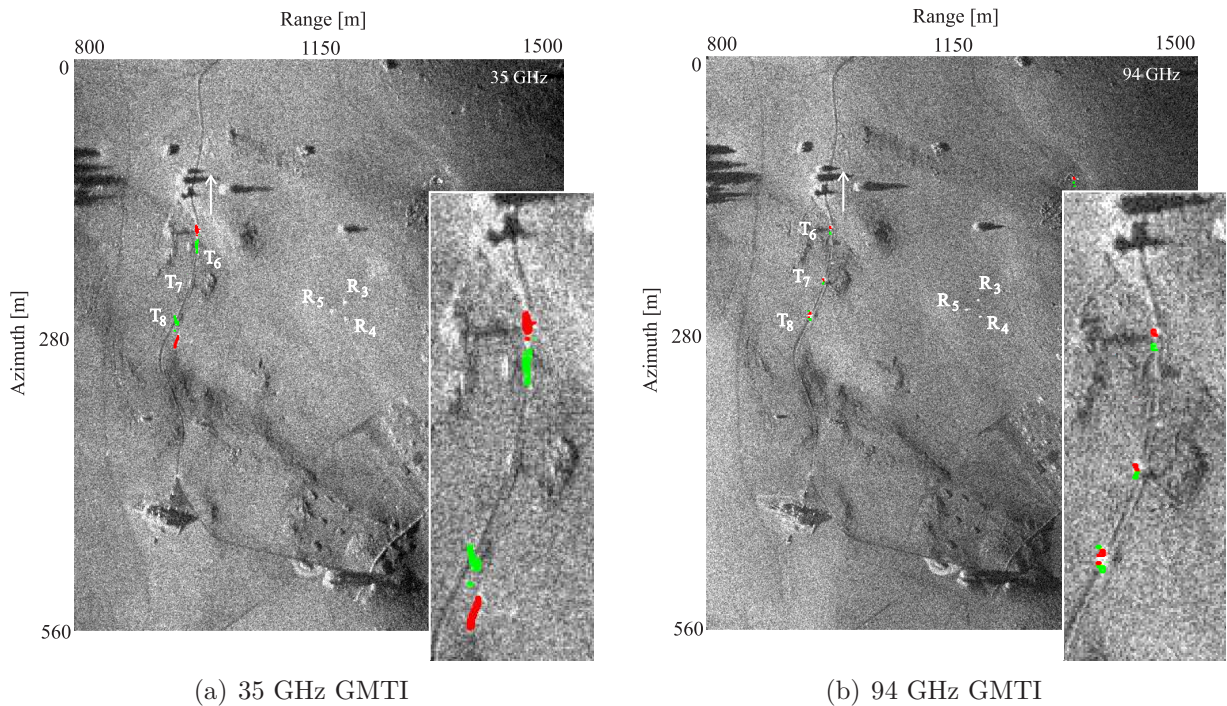


Fig. 5.9: Automatic indication of moving targets T_6 to T_8 , moving parallel and in opposite direction to the SAR sensor, with detection (red) and position correction (green) done directly in the SAR image. The targets were moving on a field path. The image dimensions are $460 \times 540 \text{ m}^2$ with a resolution of 0.75 m. Enlarged on the right side is the area of interest with the moving targets.

Table 5.2: FIELD PATH RESULTS FOR *perpendicular* TARGET MOVEMENT (SEE FIG. 5.7): MEASURED RADIAL VELOCITIES BY dGPS AND BY MEMPHIS. THE NUMBERS OF DOPPLER AMBIGUITIES m AND n ARE RESOLVED VIA LEAST COMMON MULTIPLES TO GET THE DUAL-FREQUENCY VELOCITY ESTIMATE. $\Delta\epsilon$ IS THE DIFFERENCE BETWEEN THE 35 AND 94 GHz VELOCITY MEASUREMENTS GIVEN BY (4.20).

Target	Nom. Velocity (ground) [m/s]	35 GHz SAR Vel (radial) [m/s]	94 GHz SAR Vel (radial) [m/s]	m	n	$\Delta\epsilon$ [m/s]	Dual-Freq SAR Vel (radial) [m/s]	dGPS Vel (radial) [m/s]	Δ SAR-GPS [m/s]
T_6	10	$0.85 + m \cdot 7.28$	blind	(1)	—	—	(8.1)	8.3	0.2
T_7	10	$0.76 + m \cdot 7.28$	too weak	(1)	—	—	(8.0)	9.5	1.5
T_8	10	$1.68 + m \cdot 7.28$	$0.74 + n \cdot 2.71$	1	3	0.0	8.9	9.1	0.2

Table 5.3: FIELD PATH RESULTS FOR *parallel* TARGET MOVEMENT (SEE FIG. 5.9): ABSOLUTE NOMINAL VALUES AND MEASURED RADIAL VELOCITIES OF MOVING TARGETS BY dGPS AND BY THE MEMPHIS DUAL-FREQUENCY MONOPULSE SAR SENSOR. NEGATIVE VALUES INDICATE A MOVEMENT AWAY FROM THE SAR. THE NUMBERS OF DOPPLER AMBIGUITIES m AND n ARE RESOLVED VIA LEAST COMMON MULTIPLES TO GET THE DUAL-FREQUENCY VELOCITY ESTIMATE. $\Delta\epsilon$ IS THE DIFFERENCE BETWEEN THE 35 AND 94 GHz VELOCITY MEASUREMENTS GIVEN BY (4.20).

Target	Nom. Velocity (ground) [m/s]	35 GHz SAR Vel (radial) [m/s]	94 GHz SAR Vel (radial) [m/s]	m	n	$\Delta\epsilon$ [m/s]	Dual-Freq SAR Vel (radial) [m/s]	dGPS Vel (radial) [m/s]	Δ SAR-GPS [m/s]
T_6	10	$-1.19 + m \cdot 7.28$	$-1.10 + n \cdot 2.71$	0	0	0.0	-1.2	-1.2	0.0
T_7	10	too weak	$-0.66 + n \cdot 2.71$	—	(-1)	—	(-3.4)	-3.7	0.3
T_8	10	$1.56 + m \cdot 7.28$	$-0.69 + n \cdot 2.71$	-1	-2	0.2	-5.9	-5.4	0.5

even in this difficult situation where radial target velocities are extremely small. As for the perpendicular target movements in Table 5.2, GMTI and dGPS velocities are compared and agree very well for the parallel target movements of Table 5.3.

At 35 GHz in Fig. 5.9(a), targets T_6 and T_8 are detected as moving and their shifted SAR positions are corrected. T_7 either has a too weak signature to be detected or is moving with a too low radial velocity. At 94 GHz in Fig. 5.9(b), all targets are detected and their positions are corrected. This shows that T_7 has a radial velocity, and it is its signature in the 35 GHz image that prevents indication there. A close analysis shows that the brightest returns from T_7 at 35 GHz are about 7 dB above the clutter level while the GMTI algorithm only considered targets of $T_A = 10$ dB and higher.

All three control targets, the corner reflectors R_4 , R_5 , and R_6 , are perfectly visible in the image. Non of them is colored, showing correct GMTI processing. A noticeable difference between the two images at 35 and 94 GHz in Fig. 5.9 is target smearing. At 35 GHz, the two visible targets are smeared significantly. The non-visibility of target T_7 may even be caused by this smearing. At 94 GHz, where the synthetic aperture of MEMPHIS is only about half as long as at 35 GHz and a target is illuminated by the SAR for a shorter time, the smearing is small. Targets are focused and with a clear signature. This is a significant advantage of a smaller synthetic aperture as discussed in Chapter 2.2.

On the other hand, small, non-smeared targets also present a disadvantage. While T_6 and T_8 in Fig. 5.9(a) at 35 GHz include almost 300 individual single look complex image pixels, they are made up of only 30 to 50 pixels in Fig. 5.9(b) at 94 GHz. This may reduce detectability considerably, especially if one would try to extend a GMTI algorithm with a threshold on target size and discard very small detected targets as phase disturbances, wind in trees, insufficient motion compensation of the SAR sensor movement, or many more effects influencing GMTI, including different look angles of the independent amplitude-comparison monopulse beams of the system (see Fig. 4.7(a)) as well as SAR speckle.

5.3 Freeway GMTI

A third experiment, again conducted in western Switzerland in 2005, included dual-frequency monopulse data collected over a freeway. The aim was to measure fast moving targets of opportunity on roads. Conclusions from this experiment give valuable information on traffic monitoring capabilities of mmW SAR.

Because a reference measurement on the ground was desirable to control GMTI SAR measurements, a team from the Swiss Federal Office of Metrology (METAS) was responsible for ground-based radar and laser measurements of targets moving southwards on the freeway and automatically taking photographs with time stamps and velocities of all measured vehicles.

A photograph of the freeway A12 at La Verrerie, the site of the experiment between Bulle and Châtel-Saint-Denis, is shown in Fig. 5.10. In Fig. 5.11, the ground truth mea-

surement setup with a laser and a radar is presented. A camera connected to the two measurement units was taking pictures of all vehicles being recorded. Measurements were only possible for vehicles moving south on the freeway. Traffic moving north was not



Fig. 5.10: Experiment with fast moving targets on the freeway A12 in La Verrerie. The picture was taken looking northwards from the bridge visible in Fig. 5.11.



Fig. 5.11: Ground truth measurement setup to record vehicle velocities on the freeway. A laser and a radar system were used and connected to a camera taking pictures of measured vehicles. The picture was taken looking southwards and showing the bridge visible in the center of the SAR images of Fig. 5.12

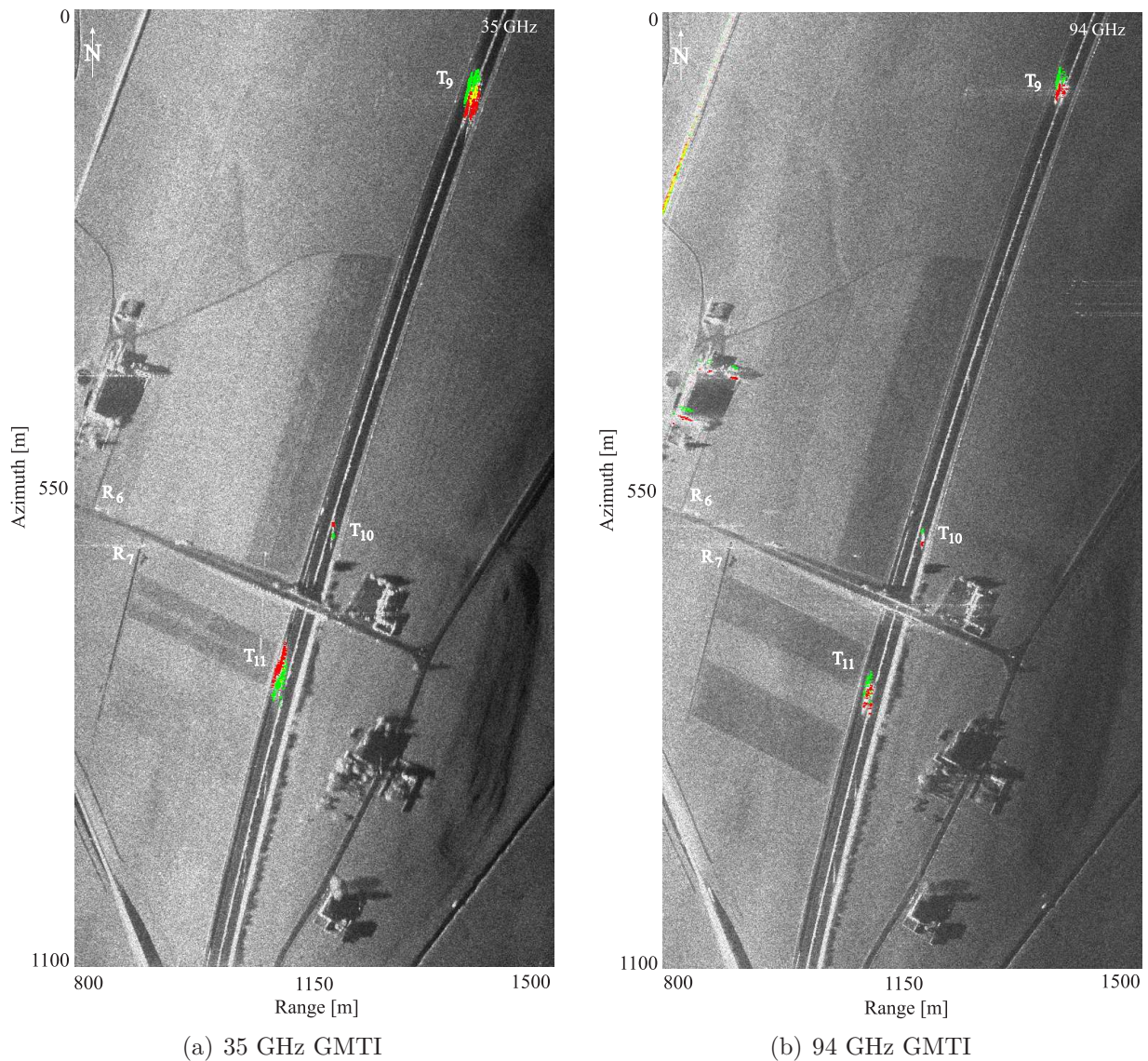


Fig. 5.12: Automatic indication of moving targets T_9 to T_{11} moving on a freeway, with detection (red) and position correction (green) done directly in the SAR image. Yellow areas exist where a detected target overlaps with a position-corrected one. The image dimensions are $500 \times 1000 \text{ m}^2$ with a resolution of 0.75 m .

recorded on the ground.

GMTI results show the 35 and 94 GHz SAR images from a recorded track in Fig. 5.12(a) and (b) where two large trucks are visible. They are colored red because they are correctly indicated by monopulse processing as moving and their calculated position shifts are given in green. When there are cases where an indicated target overlaps with a corrected position of the same or another target, the color used is yellow. Hence, the trucks were colored using the same method as in the previous experiment of Chapter 5.2, where monopulse

results and the static SAR image are fused to form a single image. We call the trucks, which were both moving southwards, T_9 and T_{11} . Another clearly visible target moving in the opposite direction is designated as T_{10} . There are two static corner reflectors R_6 and R_7 present in the data sets close to the left border. They serve as reference and control targets for the GMTI algorithms.

The flight heading to create the image in Fig. 5.12 was chosen as a compromise. For traffic monitoring, one would like to have a section of the road in the data that is as large as possible. This implies a flight heading parallel to the freeway. For GMTI, radial velocities are the largest for a flight track across the freeway. Finally, for an optimal radar cross section of targets, imaging from the side or from the front is optimal [136], requiring a flight track either parallel to or across the freeway. The chosen compromise consisted of a flight track at 20° to the freeway. This means that a large section of the freeway was included in the image. It also means that imaging of targets nearly from the side caused only a minimum reduction of their radar cross section while there would be a measurable radial target velocity. The main drawback would be a large target smearing because of the almost parallel movement with the SAR (see Chapter 2.2) or, if the targets were moving in opposite direction to the SAR, a very short illumination time.

With the given flight heading relative to the freeway and the exact depression angles, measured radial target speeds may be converted to true ground velocities on the road. A dual-frequency GMTI analysis resulted in a ground velocity of 21.1 m/s for T_9 and one of 23.9 m/s for T_{11} with $\Delta\epsilon$ equal to 0.3 m/s (T_9) and 0.2 m/s (T_{11}). T_{10} was moving in the opposite direction at 25.0 m/s and $\Delta\epsilon$ equal to 0.1 m/s. Ground based radar and laser measured T_9 moving at 22.5 m/s and T_{11} at 23.9 m/s. The northwards moving T_{10} was not measured on the ground. As a quality control, it may be observed that both corner reflectors R_6 and R_7 were identified as static targets.

The ground measurements were done near the bridge visible in Fig. 5.12, directly opposite to the indicated target T_{10} . This means that the velocity measurements of T_{11} happened within around 2 seconds, and hence almost simultaneously, for both, the SAR and the ground based radar. The difference between the two measurements is zero. The measurement of T_9 by the SAR was about 10 to 15 s earlier than the one on the ground. The two measurements differ by 1.4 m/s. This could well be because of a target slow down. After all, the ground based measurement installation was well visible from the road and would have caused most drivers to slow down slightly, be it due to curiosity or precaution.

T_9 and T_{11} could both be identified by the available photographs as trucks (see Fig. 5.13). However, in between the two trucks, two additional small cars were passing the ground measurement installation and were photographed. Their target signature could not be detected by the GMTI algorithm with $T_A = 10$ dB. Neither is their signature visible in the SAR images. A lower value for T_A , however, introduced too much phase noise and made a GMTI analysis impossible. The two cars were small and the fast movement parallel to the SAR must have caused such a large smearing and defocusing that they simply disappear in the clutter.



Fig. 5.13: Photographs of T_9 and T_{11} imaged by the camera connected to the laser and radar ground truth installation of Fig. 5.11.

Finally, there are disturbances visible on a building in Fig. 5.12(b), directly above the corner reflector R_6 , and also on the railway tracks visible in the top left corner. This is the same 94 GHz phenomenon discussed in the previous Chapter 5.2. Some GMTI processed data blocks may have experienced an insufficiently accurate Doppler centroid estimation in near range or an inaccurate monopulse curve estimation (Fig. 5.12(b) was GMTI processed with 12 blocks of independent monopulse curve estimations). Alternatively, sensor saturation may have caused incorrect phase recordings. The rest of the scene is processed correctly: the same railway track, falsely indicated in the North is also visible in the South at the bottom left corner and is indicated as static. Other buildings in center and far range, the corner reflectors, and also the bright freeway center guard rails are indicated as static.

5.4 Vibration, Rotation, and Targets of Opportunity

In Chapter 3, we presented additional experimental data from a forth experiment, again in Emmen, central Switzerland from vibrating and rotating targets. These too are ground moving targets and a correctly working GMTI algorithm has to be able to identify them.

Vibrating targets are difficult to detect. As seen in Chapter 3.7.2, there is often no visible signature in a SAR image indicating vibration. It may be possible to identify a vibrating object only through a time-frequency analysis. Therefore, a GMTI algorithm depending on a visible target amplitude as the one presented in this work will fail to indicate such a target.

Rotating target signatures, however, are well visible for the rotating corner reflector and the radar dish introduced in Chapter 3.8.2. A GMTI analysis promises the detection of such a movement as well as the determination of the radial velocity of rotation, allowing

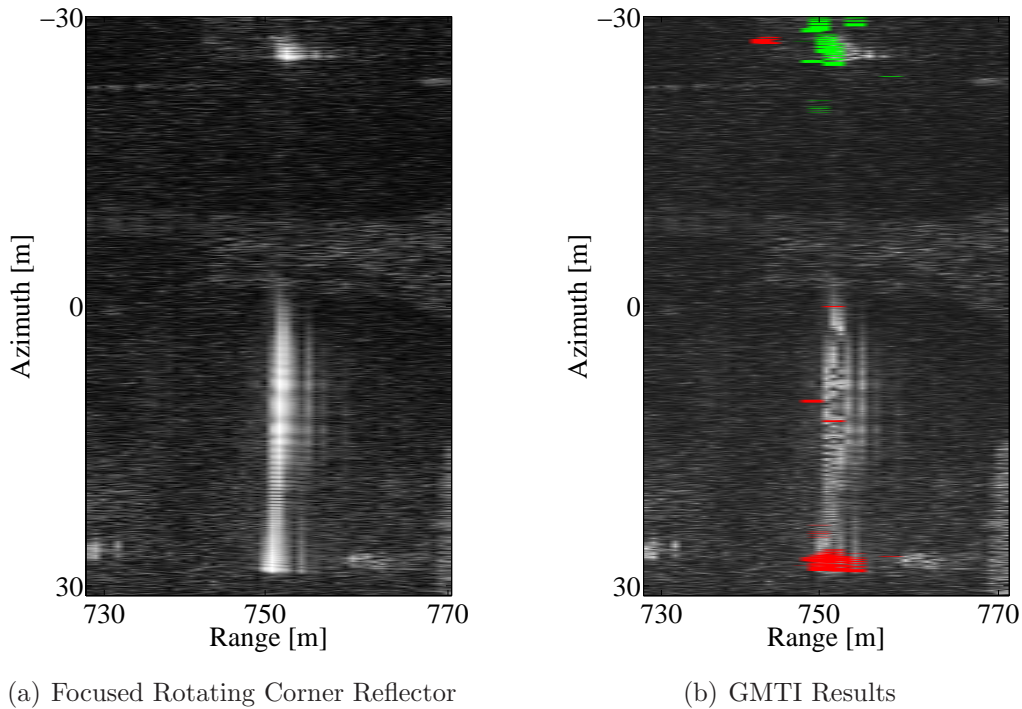


Fig. 5.14: (a) 94 GHz SAR intensity image of the rotating corner reflector from Fig. 3.23 turning on a pedestal with 1 Hz. (b) GMTI processing indicates the rotating parts in red and gives a correct corner position in green.

the calculation of the rate of rotation if target dimensions are known.

In Fig. 5.14(a), the signature of the rotating corner reflector presented in Chapter 3.8.2 is shown. GMTI results are given in (b). The reflector is indicated as moving and a position correction successfully relocates the signature to the true ground position of the reflector. Velocity estimation for the reflector indicates a maximum ambiguities-resolved velocity of -6.1 m/s on the ground and a range of velocities from -4.2 to -6.1 m/s. The negative values indicate a movement away from the SAR sensor. The reason for the wide range of velocities is directly implied in the rotation. The corner reflector has a constant angular velocity of 6.2 m/s derived from a lever arm that is 1 m long and a rotation frequency of 1 Hz. This angular frequency gives a wide range of radial velocities picked up by the SAR sensor. The lower bound of -4.2 m/s is given by the GMTI algorithm with amplitude and monopulse thresholds.

Fig. 5.15 shows GMTI results for the rotating radar dish introduced in Chapter 3.8.2. Again, the algorithm correctly identifies the target movement and does a position correction. The resulting maximum unambiguous target velocity determined by the algorithm is 7.8 m/s on the ground. Knowing the rotation frequency of the radar dish to be approximately 4 Hz, its diameter must be close to 5 m.

Finally, in Fig. 5.16 GMTI results of a MEMPHIS scene with targets of opportunity

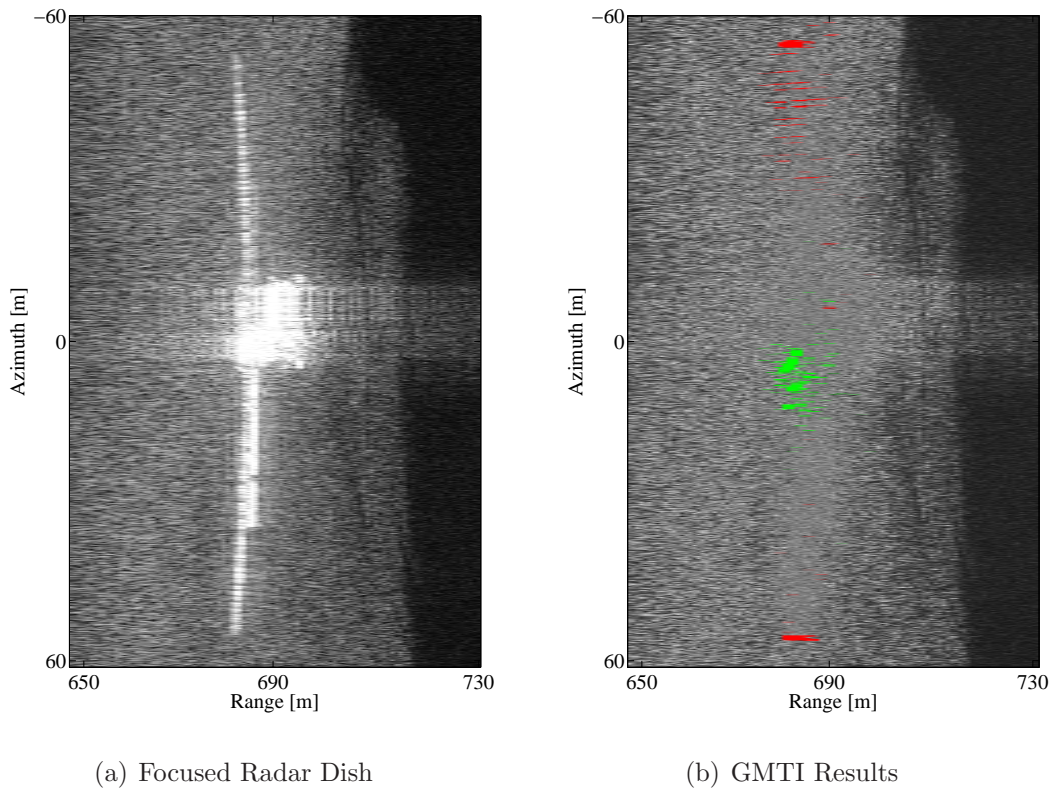


Fig. 5.15: (a) 94 GHz SAR intensity image of a ground-based radar antenna with a diameter of several meters, rotating at 0.25 Hz. (b) GMTI processing indicates the rotating parts in red and gives a correct radar position in green.

are shown. For ease of interpretation, large arrows have been added to mark targets (red) and their true ground position (green). Since there were no ground control measurements during the experiment for these targets, the only possibility to check on plausibility of GMTI results is target position. The three targets on the right in Fig. 5.16 are shown as moving on a road. Target size suggests that three cars are indicated. Additionally, the fourth indicated target on the left shows the rotating radar dish shown in Fig. 5.15, correctly identified as having rotated during the experiment.

5.5 Discussion

The first three experiments presented above highlight the capabilities of GMTI with a mmW SAR. They demonstrate good target detectability for slow moving targets as well as for large fast moving ones. However, if targets have a high velocity parallel to the SAR flight track and a small radar cross section as the cars on a freeway do, they may disappear. Adequate radar cross section is crucial in all experiments. Moving targets with corner reflectors show larger GMTI signatures and better velocity estimates and position

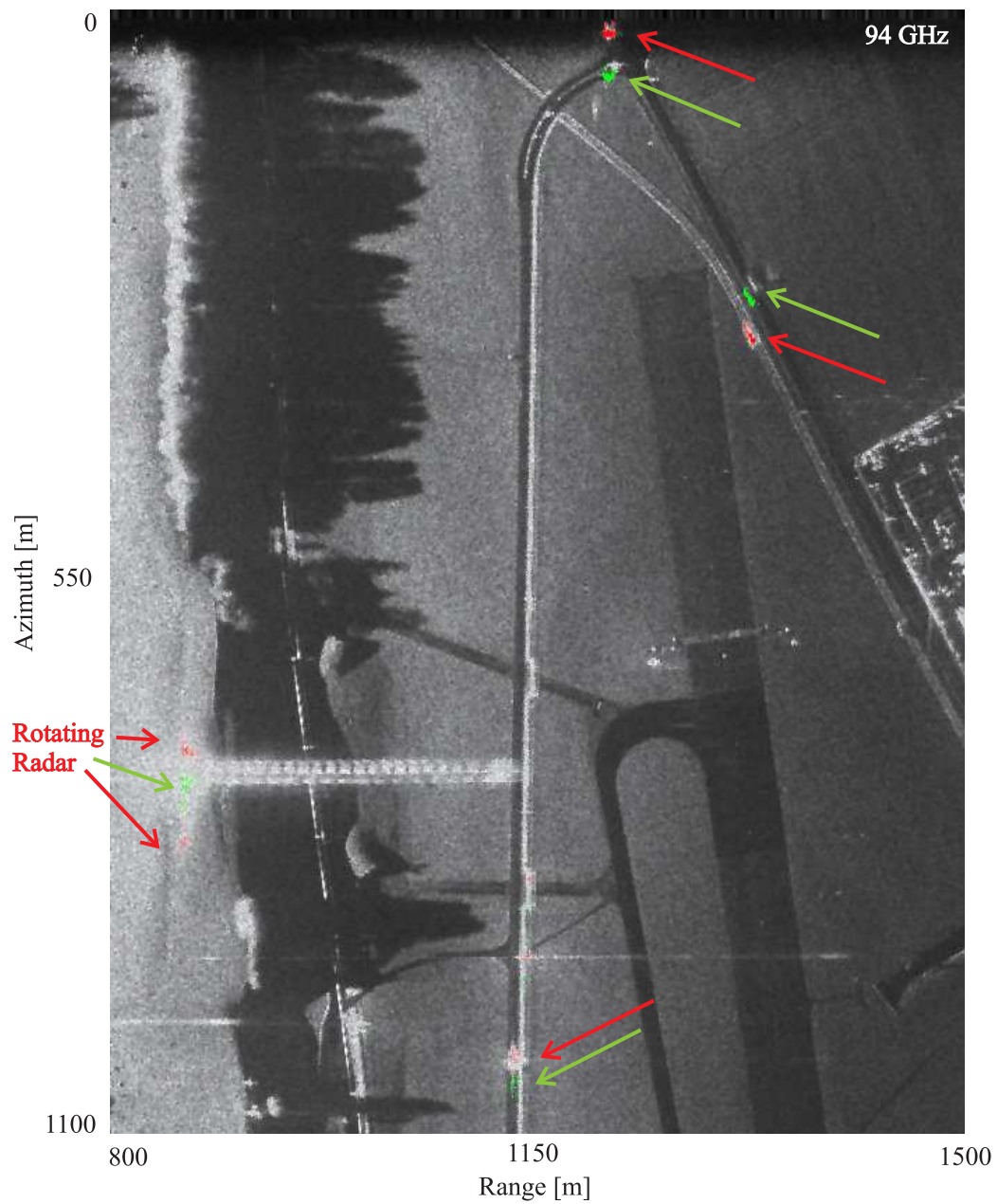


Fig. 5.16: GMTI of a MEMPHIS scene at 94 GHz with targets of opportunity. For ease of interpretation, large arrows have been added to mark targets (red) and their true ground position (green). Additionally, the rotating radar dish shown in Fig. 5.15 is visible on the left and correctly identified as moving.

correction.

The fourth experiment shows that vibrating targets are not detectable with the approach of this thesis because their signatures in the focused SAR images are not prominent enough. STAP detection techniques as described in [78] would probably be needed to filter out background clutter. Rotating targets, however, are well visible and indicated with dual-frequency GMTI. Large variations in the measured radial target velocity even allow the identification of the movement as a rotation.

For all four experiments, an amplitude threshold of 10 dB above the clutter level (see (4.33)) and also a monopulse threshold of 10 dB (see (4.37)) were used. Higher values suppressed too much information of targets and target movements. Lower values added disturbances from various sources such as phase disturbances from motion compensation and aircraft movement, effects of clutter movement by wind, or possibly target signature variations from different aspect angles by the squinted monopulse beams and speckle.

Important additional information on the quality of a GMTI outcome may be drawn from the number of pixels in an image. A single pixel being indicated as moving may well be caused by speckle or phase disturbances while several hundred clustered pixels provide a reliable moving target indication. This opens the possibility to include a filter based on target size to improve on a constant false alarm rate instead of the simple threshold used. A direct analysis of CFAR performance would be beyond the scope of this work, and the reader is referred to [66].

Furthermore, the presented GMTI algorithm is based on a theory assuming constant target velocity. Results on field paths, where targets necessarily had to break in bends and due to path conditions and then accelerate again, showed good results and no recognizable influence from such small non-constant movement effects. For an analysis of large target acceleration, see [65, 110].

Finally, change detection between the two images of a dual-frequency SAR may offer an additional help to decide on the indication of moving targets. A hut roof in Fig. 5.7(b) and railway tracks in Fig. 5.12(b) are indicated as moving at 94 GHz but not at 35 GHz. Change detection may be an unreliable technique, though, because target and clutter radar cross section may vary greatly, as may be seen by the frequency-dependent reflectivity of fields near target T_{11} in Figs. 5.12(a) and (b).

Chapter 6

Conclusion

In this chapter we briefly summarize our results and give possible directions for future research in the two areas considered, namely the analysis of target movement in mmW SAR and the development of suitable GMTI algorithms for it.

6.1 Summary of Results

6.1.1 Analysis of Target Movement

Constant movement and acceleration are well-known and well-discussed target movements in SAR. Nevertheless, a thorough understanding and analysis of movement effects are important when wanting to develop GMTI algorithms. Aliasing effects of blind speeds and ambiguous Doppler shifts are essential hurdles to overcome especially for mmW GMTI.

Related to constant movement and acceleration, micro-Doppler effects are an interesting field of SAR research. A system model was proposed that allows flexible simulations of vibration and rotation. It defines the instantaneous position of a target, its displacement effects in SAR imagery, and the Doppler shifts induced in the signal. An analysis of motion patterns in focused intensity images as well as in time-frequency distributions was conducted, showing micro-Doppler phenomena in simulations and in real data that match the underlying signal theory.

We introduced the reader to the possibilities of airborne mmW SAR imaging of vibrating and rotating targets. The large range of potential applications may include anything from the detection of vehicles standing in traffic jams with idling engines to the reconnaissance of airfields where rotating helicopter blades or ground-based radar dishes are present.

6.1.2 GMTI

For mmW SAR systems, amplitude-comparison monopulse data collection is a very effective GMTI recording technique that solves the dilemma of extremely short interferometric mmW baselines. It is a sound method with multiple channels sharing a single phase center. The basic concept is well-known from tracking radar applications and directly transferable to SAR GMTI scenarios.

Processing of monopulse data for SAR GMTI includes the mathematically complex nonlinear data modeling step presented in this work to fit received and compressed signals to a stochastically determined hyperbolic tangent function in the range Doppler domain. Resulting deviations of moving targets from this function and thus from the static scene are easily detectable and corrected, allowing for exact radial target velocity calculations and position shift corrections.

When calculating radial target velocities, a general problem for mmW SAR GMTI are high Doppler frequency shifts from the detected targets even at velocities of a few meters per second. PRF requirements for unambiguous velocity measurements would be exceedingly high. Using dual-frequency information, the concern about high PRF requirements is eliminated using the theory of least common multiples of the single velocity ambiguities. Indication of targets is very sensitive, and accurate position corrections are possible.

Experimental data was presented, recorded with the dual-frequency 35 and 94 GHz SAR system MEMPHIS. GMTI results obtained with the presented $\Sigma\Delta$ processing algorithm showed the effectiveness of monopulse processing for SAR and the capabilities in different environments and with various radial and tangential target velocities. Monopulse processing of the Δ/Σ Doppler signal ratios made use of complex signal information to estimate and generate a phase-corrected monopulse curve. Velocity estimates and target displacement corrections were accurate and could be fully automated using blockwise monopulse processing of large SAR scenes. Additional considerations and possibilities of dual-frequency SAR for GMTI were discussed, including target blind speed elimination and change detection.

The functionality of the GMTI algorithm discussed could even be extended to detect rotating targets. An experimental rotating corner reflector as well as a large airport radar dish could be indicated as moving and their rotation frequency could be determined without the help of a time-frequency representation.

Important for the GMTI performance in all target environments and for all target velocities proved to be accurate, range-dependent Doppler centroid values. Equally important were suppression of phase disturbances from motion compensation of aircraft movement, influences of clutter movement by wind, and speckle variations from different look angles of the monopulse beams. This suppression could be achieved by amplitude and monopulse thresholding.

It could be shown that the theoretical hyperbolic tangent monopulse curve fits very well

to measured static corner reflector data, giving proof to the practical application of our modeling approach, to the developed algorithm, and also to the theory of dual-frequency SAR.

6.2 Possible Directions for Further Research

There is a global trend towards higher and higher bandwidth in radar in general and airborne and spaceborne SAR in particular. mmW SAR is well suited to offer very large system bandwidth because of its high carrier frequencies within bands that are not intensely used as of today. Large bandwidth means high resolution. This implies more exact algorithms and fewer approximations. More exact algorithms are only possible when being able to do SAR focusing with a high accuracy regarding both signal processing and geometry. Time-domain algorithms such as backprojection offer exactly this, but at a high computational cost and only when accurate sensor motion and position data of the SAR antenna phase center are available. With a requirement for sub- λ phase accuracy, we are talking about sub-millimeter sensor motion and position determination. A difficult challenge.

While more accurate data processing is on one side of high resolution mmW SAR, better adaptive filters in GMTI are on the other. Approximations of general thresholds for signal intensity and monopulse curve on blocks of data may not be sufficient to do successful target indication in highly variable environments. STAP filtering of raw radar data points in exactly this direction; it has been, and will continue to be, one of the hot topics in radar and moving target indication.

Classic STAP as explained in [78] could also greatly improve results for weak targets hidden in clutter. The algorithms presented in this work only detect targets that are well visible and none that are suppressed by a high background clutter level. With a STAP preprocessing of raw radar data, it may even be possible to identify vibrating targets. While time-frequency distributions may indicate vibration as a micro-Doppler effect in the SAR image, it is computationally expensive and needs a reliable decision-making algorithm or human operator to identify patterns in a distribution.

Finally, if many moving targets are present within one scene, effective clustering algorithms to extract the single targets are needed. Similarly, clustering may help to identify large extended targets by assigning their individual pixels to them. Once a target is indicated, the algorithm's quality could be improved by adding a constant false alarm rate. Such a CFAR filtering could reduce residual errors of an algorithm. Furthermore, large misinterpretations—such as the railway track over a large part of a scene in Chapter 5.3—could be handled and dismissed as processing inaccuracies.

Today, mmW SAR GMTI offers a great tool in military reconnaissance and civilian traffic monitoring with small drones or UAVs as sensor carrier. And once the above mentioned obstacles are overcome, high resolution mmW SAR could prove to be the single most inexpensive and reliable way of GMTI of the near future.

Appendix A

The FGAN MEMPHIS SAR System

The multi-frequency experimental monopulse high-resolution interferometric SAR MEMPHIS designed and built by the German FGAN-FHR (Research Establishment of Applied Science for High Frequency Physics and Radar Techniques) is described in [1]. The following Table A.1 gives an overview of possible system modi, range of parameters, and hardware parameters at both carrier frequencies of 35 and 94 GHz. The two frequencies may be operated simultaneously.

Fig. A.1 shows the typical carrier platform of MEMPHIS, a *Transport Allianz C-160 Transall* of the German airforce. The SAR sensor is located at the rear parajumper door on the left side of the aircraft. The sensor itself is shown in Fig. A.2 from inside the aircraft and from outside with a view of the 35 and 94 GHz antennas.



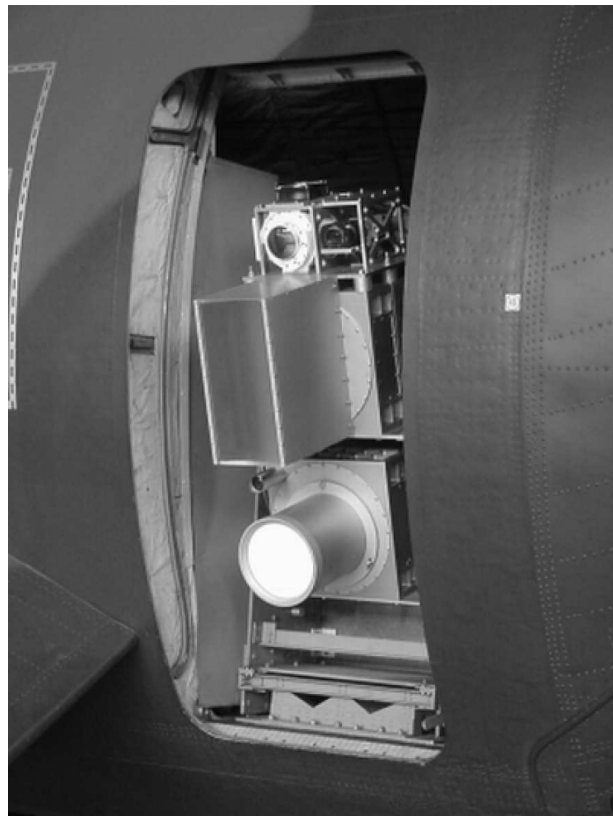
Fig. A.1: *Transport Allianz C-160 Transall* of the German airforce. The SAR sensor is located at the rear parajumper door behind the main gear.

Table A.1: FGAN MEMPHIS SYSTEM SPECIFICATIONS AND TYPICAL OPERATING PARAMETERS.

Frequency Band		K _a -Band at 35 GHz	W-Band at 94 GHz
Transmitter	Power	500 W	700 W
	PRF	1500 - 12948 Hz	
	Pulse Waveform	Up Chirp	
	Pulse Bandwidth	200 MHz	
	Max. Stepped Frequency Bandwidth	800 MHz	
	Pulse Length	0.4 or 1.2 μ s	
	Spectral Purity	> -70 dB/Hz	
	Phase Stability	10° RMS	
	Polarization	Linear H/V or Circular R/L, Switchable from Pulse to Pulse	
Receiver	Receive Channels	4	
	Dynamic Range	60 dB	
	System Noise Figure	15 dB (SSB)	
	Polarization	Co- and Cross-Polarization	
	Sampling Rate	200 MHz per Channel	
	Range Gates	550 or 1000	
	Bytes per Sample	2 Bytes (1 Byte Amplitude + 1 Byte Phase)	
SAR Antenna	Type	Monopulse or Interferometric, Asymmetric Dielectric Lenses	
	Diameter	0.3 m	
	3 dB Beamwidth Azimuth	3°	1°
	3 dB Beamwidth Elevation	16°	16°
	Gain	27 dB	29 dB
Data Acquisition	Data Rate	33 MByte/s	
	Simultaneous Channels	8 Data Channels + GPS/INS + Timecode	
	Storage Capacity	48 GByte	
Typical Flight Geometry	Flight Level	300 - 1000 m a Gnd	
	Aircraft Speed	75 m/s to Gnd	
	Sensor Depression Angle	18 - 32°	
	Slant Range	500 - 2000 m	



(a) Radar hardware



(b) Antennas

Fig. A.2: MEMPHIS inside the aircraft with a view of the radar hardware in (a) and from outside of the parajumper door with the visible 35 and 94 GHz antennas in (b). The 94 GHz antenna at the bottom of the image is a round asymmetric lens monopulse antenna while the shown 35 GHz antenna in the center is an interferometric array with four receive horns. On top of the two antennas is an additional infrared sensor. (Image courtesy of FGAN-FHR)

List of Figures

2.1	Typical SAR flight geometry.	7
2.2	Pulse compression.	9
2.3	The Doppler shift of a point target.	10
2.4	An illustration of the Doppler history.	11
2.5	EADS MiSAR.	13
2.6	Single pass interferometry with an aircraft and two SAR antennas.	17
2.7	Imperfect flight track or antenna misalignment for ATI.	17
2.8	Geometry of a two-pass cross-track interferometry experiment.	19
2.9	The fringe pattern on a flat surface caused by a spatial baseline.	20
2.10	Amplitude image of the river Reuss.	23
2.11	Raw along-track interferogram of the river Reuss.	24
2.12	Flattened along-track interferogram of the river Reuss.	25
2.13	Estimation of $\overline{\Delta\phi}$ over a small and 10-multilooked section of the Reuss. . .	25
2.14	Phase corrected coherence map of the along-track interferogram.	26
3.1	SAR geometry with a target moving perpendicular to the flight track. . . .	31
3.2	Two-dimensional SAR geometry for the system model used.	32
3.3	Pulse-compressed and focused intensity images of a point target at 94 GHz. . .	34
3.4	Focused SAR image of a static corner reflector at image center.	35
3.5	WVD of the pulse compressed data from a 94 GHz SAR point target. . . .	36
3.6	WVD of the pulse compressed SAR data of a static corner reflector. . . .	37
3.7	Focused SAR scenes with a constantly moving center target.	40
3.8	Ambiguous target displacement and blind target speed.	41
3.9	Fast targets: multiple Doppler ambiguities, smearing over many range bins. .	41
3.10	Time-Frequency representation (WVD) of the four target movements. . . .	43
3.11	SAR scenes with five point targets, including an accelerating center target. .	45

3.12	Time-Frequency representation (WVD) of the two accelerating targets. . .	46
3.13	Two focused 94 GHz SAR images, each with five simulated vibrating targets. . .	49
3.14	Time-frequency representation of four simulated SAR vibrating targets. . .	50
3.15	Measured vibration amplitudes of a truck running with an idle engine. . . .	52
3.16	Measured vibration frequencies of a truck running with an idle engine. . . .	52
3.17	Focused SAR intensity image of a static and a vibrating truck on a tarmac. . .	53
3.18	WVD of the Doppler spectrum for a static and a vibrating truck.	54
3.19	Model of a rotating target.	55
3.20	Three simulated focused 94 GHz rotating targets.	56
3.21	WVD of a simulated target rotating at 10 Hz.	57
3.22	WVD of two simulated targets rotating at 0.5 and 0.2 Hz.	58
3.23	Rotating corner reflector turning on a pedestal with 1 Hz.	59
3.24	Focused SAR intensity image of a rotating corner reflector.	59
3.25	Time-frequency representation of a rotating corner reflector.	60
3.26	An airfield air surveillance radar dish.	61
3.27	Focused SAR intensity image of a ground-based rotating radar antenna. . .	61
3.28	WVD of the ground-based radar antenna from Fig. 3.27.	62
3.29	Three SAR intensity images of a ground-based rotating radar antenna. . .	63
4.1	Schematic amplitude-comparison monopulse Cassegrain reflector antenna. . .	69
4.2	3-D antenna pattern from an amplitude-comparison monopulse antenna. . .	69
4.3	Amplitude- and phase-comparison monopulse.	70
4.4	Monopulse channel circuitry with four receive antennas.	71
4.5	Monopulse concept for a tracking radar.	72
4.6	Theoretical monopulse signals of a tracking radar.	75
4.7	Monopulse concept with a target seen by four independent receive channels. .	76
4.8	Focused 35 GHz SAR image of an airfield runway.	80
4.9	Focused 94 GHz SAR image recorded simultaneously with the one in Fig. 4.8. .	80
4.10	Theoretical Doppler spectra of monopulse SAR.	83
4.11	Monopulse processing of endo- and exo-clutter targets.	84
4.12	Monopulse data Σ and Δ channels at 35 GHz.	85
4.13	GMTI algorithm that generates a moving target map.	87
5.1	Experiment on the airfield of Emmen.	90

5.2	Monopulse ratios at 35 GHz for the Emmen experiment.	91
5.3	Monopulse ratios at 94 GHz for the Emmen experiment.	92
5.4	Indicated and position-corrected moving targets in Emmen at 35 GHz. . .	92
5.5	Indicated and position-corrected moving targets in Emmen at 94 GHz. . .	94
5.6	Experiment area on the Mont Racine.	95
5.7	Automatic indication of radially moving targets on the Mont Racine. . . .	96
5.8	Enlarged area of the hut in front of target T_6	96
5.9	Automatic indication of parallelly moving targets on the Mont Racine. . .	97
5.10	Experiment with fast moving targets on the freeway in La Verrerie.	101
5.11	Ground truth measurement setup in La Verrerie.	101
5.12	Automatic indication of moving targets T_9 to T_{11} in La Verrerie.	102
5.13	Ground photographs of targets T_9 and T_{11}	104
5.14	GMTI results of a rotating corner reflector.	105
5.15	GMTI results of a ground-based rotating radar antenna.	106
5.16	GMTI of a MEMPHIS scene at 94 GHz with targets of opportunity.	107
A.1	Transport Allianz C-160 Transall of the German Luftwaffe.	113
A.2	MEMPHIS from inside and outside of the aircraft.	115

List of Tables

3.1	Important radar system parameters for mmW simulations.	34
5.1	Controlled environment GMTI results on the airfield of Emmen.	93
5.2	Field path GMTI results for <i>perpendicular</i> target movement.	98
5.3	Field path GMTI results for <i>parallel</i> target movement.	99
A.1	FGAN MEMPHIS system specifications and typical operating parameters.	114

List of Acronyms

A complete list of all acronyms appearing in this work is given below. If the terms are not self-explanatory or in a foreign language, a small explanation or a translation is given. Otherwise please refer to the index of this work and to the paragraphs where the acronyms appear for a full description of their meaning.

ATI	Along-Track Interferometry
CFAR	Constant False Alarm Rate
CW	Continuous Wave
CWFM	Continuous Wave Frequency Modulation
dGPS	differential GPS
DPCA	Displaced Phase Center Antenna
EHF	Extremely High Frequency—highest radio frequency band between 30 and 300 GHz
FGAN-FHR	Forschungsgesellschaft für Angewandte Naturwissenschaften—German research establishment of applied science for high frequency physics and radar techniques
GMTI	Ground Moving Target Indication
GPS	Global Positioning System
INS	Inertial Navigation System
InSAR	Interferometric SAR
lcm	least common multiple—as a mathematical operation
MEMPHIS	Multi-frequency Experimental MonoPulse High-resolution Interferometric System

METAS	Bundesamt für METrologie und Akkreditierung der Schweiz—Swiss federal office of metrology
mmW	MilliMeter Wave—all radio frequency signals inside the EHF band
MPR	MonoPulse Ratio
PRF	Pulse Repetition Frequency
PRI	Pulse Repetition Interval—the inverse of the PRF
SAR	Synthetic Aperture Radar
SNR	Signal to Noise Ratio
SRTM	Shuttle Radar Topography Mission—a Space Shuttle SAR mission in the year 2000
STAP	Space-Time Adaptive Processing
UAV	Unmanned Aerial Vehicle
WVD	Wigner-Ville Distribution—a time-frequency representation of signals

List of Symbols

α	Chirp rate of a pulsed chirp signal $p(t)$.
β	Linear coefficient of the pulsed chirp signal $p(t)$.
$\gamma(r, z)$	Complex correlation between the two coregistered SAR images.
$\gamma'(r, z)$	Phase corrected coherence map.
$ \gamma $	Coherence, a measure of interferometric phase noise.
δ_r	Slant range resolution.
δ_z	Azimuth resolution.
Δ	Monopulse radar difference channel.
Δ_{az}	Monopulse radar difference channel in azimuth.
Δ_{el}	Monopulse radar difference channel in elevation.
$\Delta\epsilon$	GMTI velocity estimation precision indicator defined as the deviation between the 35 and 94 GHz velocity measurements.
$\Delta\phi(r, z)$	Phase or phase difference in an interferogram of two focused SAR images.
$\overline{\Delta\phi}$	Average interferometric phase of a target.
Σ	Monopulse radar sum channel.
ψ	Angle between the tangent plane and the baseline B_S .
θ	Off-nadir angle of the SAR main beam, $\theta = \pi/2$ —depression angle.
κ	Paired echoes in a focused SAR image induced by target vibration.
λ	Wavelength of a signal or carrier wave with $\lambda = c/f_c$.
ν	Normalization constant for a Gaussian distributed signal, e. g. a Doppler spectrum with $\nu = 1/\omega_p$.

π	Ratio of a circle's circumference to its diameter: $\pi = 3.141592$.
τ_p	Pulse duration of a chirp signal $p(t)$.
ϕ	Signal phase of an arbitrary signal.
$\phi(r, z)$	Phase of the focused SAR image at range r and azimuth z .
ϕ_Δ	Signal phase of a monopulse difference channel.
ϕ_Σ	Signal phase of a monopulse sum channel.
ϕ_0	Initial angle of a rotating target towards the SAR sensor at time zero.
ϕ_d	Antenna aperture divergence angle in azimuth.
$\varphi(T)$	Target aspect angle as a function of the slow time T .
$\varphi(u)$	Target aspect angle as a function of the sensor position u .
φ_0	Squint angle between the beams of an amplitude-comparison monopulse radar.
φ_n	Target aspect angle of target n .
ω	Signal frequency in radians or temporal frequency domain for the fast time t .
ω_0	Doppler frequency shift between the monopulse channels resulting from the squinted antenna beams.
ω_c	Radar signal carrier or center frequency in radians, $\omega_c = 2\pi f_c$.
ω_d	Doppler domain or temporal frequency domain for the slow time T .
ω_p	Half-power frequency of a Gaussian distributed Doppler spectrum.
ω_R	Rotation frequency of a rotating target.
ω_V	Vibration frequency of a vibrating target.
ω_W	Radar signal bandwidth in radians, $\omega_W = 2\pi W$.
a	SAR signal return echo amplitude or a free parameter in data modeling.
$a(\omega, r, z)$	Generalized SAR signal amplitude as a combination of the physical target reflectivity A and the return echo amplitude a .
a_n	SAR signal return echo amplitude of target n .
a_r	Target acceleration radial to and away from the SAR sensor.
a_z	Target acceleration parallel to the SAR sensor movement.

\mathbf{a}	Two-dimensional acceleration vector of a target.
A	Physical target reflectivity constant.
$A(r, z)$	Amplitude of a focused SAR image at range r and azimuth z .
A_n	Physical target reflectivity constant of target n .
A_V	Vibration amplitude of a vibrating target.
\bar{A}	Average clutter return amplitude in a SAR image in dB.
\mathbb{A}	Monopulse antenna feed channel designator: physical channel located in the top left corner of a four-horn square.
b	free parameter in data modeling.
B	Length of spatial baseline for InSAR or of the antenna separation of a phase-comparison monopulse radar.
B_{\perp}	Perpendicular baseline length for InSAR.
B_S	Spatial baseline for InSAR.
B_T	Temporal baseline for InSAR.
\mathbb{B}	Monopulse antenna feed channel designator: physical channel located in the top right corner of a four-horn square.
c	Speed of light (in vacuum: $c = 2.997925e8$ m/s, in air: $c = 2.997078e8$ m/s) or a free parameter in data modeling.
\mathbb{C}	Monopulse antenna feed channel designator: physical channel located in the bottom left corner of a four-horn square.
d	Displacement of a moving target in azimuth due to a Doppler shift.
\mathbb{D}	Monopulse antenna feed channel designator: physical channel located in the bottom right corner of a four-horn square.
f_c	Radar signal carrier or center frequency.
f_d	Doppler shift or Doppler frequency.
g	Acceleration due to gravity. On earth at sea level $g = 9.80665$ m/s ² .
$h_{2\pi}$	InSAR phase value of ambiguity or topographic height difference of one full phase cycle.
$H(\omega, r, z)$	SAR transfer function.

$H_n(\omega, r, z)$	SAR transfer function of target n .
$i(r, z)$	Interferogram of two SAR images $s_{c1}(r, z)$ and $s_{c2}(r, z)$.
j	Imaginary unit of a complex number.
$J_\kappa(x)$	Bessel function of the first kind of order κ .
ℓ	Physical SAR antenna length.
$L(r)$	Antenna half-beamwidth at range r .
m	Index variable, e. g. for point targets of a rotating object n .
M	Monopulse curve defined as a parameterized function fitting the Δ/Σ ratios of a monopulse radar.
\mathbb{M}	Master channel as derived from a monopulse radar. Only ideally equal to an InSAR master image s_{c1} .
MPR	Monopulse ratio defined by the Δ/Σ ratio of a monopulse radar.
n	Index variable, e. g. to designed a specific target.
$p(t)$	Pulsed chirp signal as a function of the fast time t .
$P(\omega)$	Fourier transform of a pulsed chirp signal $p(t)$.
PRF	Pulse repetition frequency of a pulsed radar system.
\mathbf{Q}_n	location vector of point target n on the ground: $\mathbf{Q}_n = (r_n, z_n)$.
$\mathbf{Q}_{m,n}$	location vector of point target m belonging to rotating target n .
q	InSAR mode factor for interferometric phase differences.
r	Range or cross-track coordinate.
$r(t)$	Cross-track distance as a function of the fast time t .
\mathbf{r}	Radial look vector from the sensor to a target; may be a function of T .
r_n	Range to target n .
R	Distance to a target; may be a function of T and equal to $ \mathbf{r} $ in vector representation.
R_0	Range of closest approach from the sensor to a target.
R_c	Range to the center of the area of interest.

$R_{m,n}$	Radius to point target m of a rotating object n .
$s(t)$	Received or echoed SAR signal as a function of the fast time t or any generic signal.
$s(t, z)$	Received or echoed SAR signal as a function of fast time t and azimuth time T .
$s_0(t)$	Basebanded received SAR signal as a function of the fast time t .
$s_c(r, z)$	Compressed or focused two-dimensional SAR image depending on range r and azimuth z .
$s_{c1}(r, z)$	Complex InSAR master image.
$s_{c2}(r, z)$	Complex InSAR slave image.
$s_M(t)$	Matched-filtered or range-compressed SAR signal as a function of the fast time t .
$S(\omega)$	Fourier transform of the signal $s(t)$.
$S_0(\omega)$	Fourier transform of the basebanded signal $s_0(t)$.
$S_c(r, \omega_d)$	Range-Doppler spectrum of the focused SAR image.
$S_M(\omega)$	Fourier transform of the range-compressed SAR signal $s_M(t)$.
\mathbb{S}	Slave channel as derived from a monopulse radar. Only ideally equal to an InSAR slave image s_{c2} .
t	Fast time or the time in range r .
T	Slow time (the time in azimuth z) for the SAR sensor or the dwell time that the radar beam illuminates a target.
T_n	Radar target n on the ground.
T_A	Amplitude threshold constant in dB.
T_M	Monopulse threshold constant in dB.
u	Nominal sensor position in azimuth.
\hat{v}	Target velocity in the direction radial to and away from the SAR sensor. For a focused SAR image in slant range, $\hat{v} \approx v_r$.
\hat{v}_n	Target velocity in the direction radial to and away from the SAR sensor for a target n .

v_r	Target velocity in range—as opposed to \hat{v} which is the radial velocity: $v_r = \hat{v} \cdot \cos \varphi(T)$.
v_s	SAR sensor velocity in azimuth.
v_z	Target velocity in azimuth, parallel to the SAR sensor.
\mathbf{v}	Two-dimensional velocity vector.
\mathbf{v}_n	Two-dimensional velocity vector of a target n .
$ \mathbf{v} $	Absolute speed of a target.
$V_n(T)$	One-dimensional vibration movement vector of a target n .
W	Radar signal bandwidth.
x	Generic variable used to describe general signals and values.
z	Azimuth distance or along track coordinate.
z_n	Azimuth distance to target n .
$z(T)$	Azimuth or along track distance as a function of the slow time T .
z	Azimuth distance to target n .
\mathbb{Z}	The set of whole numbers $\{\dots-3, -2, -1, 0, 1, 2, 3\dots\}$.

Bibliography

- [1] H. Schimpf, H. Essen, S. Böhmendorf, and T. Brehm, “MEMPHIS - A Fully Polarimetric Experimental Radar,” *Proceedings of the IEEE International Geoscience and Remote Sensing Symposium IGARSS*, vol. 3, pp. 1714–1716, June 2002.
- [2] M. Rüegg, E. Meier, and D. Nüesch, “Vibration and Rotation in Millimeter Wave SAR,” *IEEE Transactions on Geoscience and Remote Sensing*, vol. 45, no. 2, pp. 293–304, Feb. 2007.
- [3] M. Rüegg, E. Meier, and D. Nüesch, “Capabilities of Dual-Frequency Millimeter Wave SAR with Monopulse Processing for Ground Moving Target Indication,” *IEEE Transactions on Geoscience and Remote Sensing*, vol. 45, no. 3, pp. 539–553, Mar. 2007.
- [4] M. Rüegg, M. Hägelen, E. Meier, and D. Nüesch, “Moving Target Indication with Dual Frequency Millimeter Wave SAR,” *Proceedings of the IEEE Radar Conference*, pp. 350–357, Apr. 2006.
- [5] C. A. Wiley, “Pulsed Doppler Radar Methods and Apparatus,” *United States Patent 3196436, Filed August 1954*, 1965.
- [6] M. I. Skolnik, Ed., *Radar Handbook, Second Edition*. New York: McGraw-Hill, 1990.
- [7] B. R. Mahafza and A. Z. Elsherbeni, *Matlab Simulations for Radar System Design*. Boca Raton: Chapman & Hall / CRC, 2004.
- [8] B. R. Mahafza, *Radar Systems Analysis and Design Using Matlab*. Boca Raton: Chapman & Hall / CRC, 2000.
- [9] R. J. Sullivan, *Microwave Radar: Imaging and Advanced Concepts*. Boston: Artech House Publishers, 2000.
- [10] D. C. Schleher, *MTI and Pulsed Doppler Radar*. Boston: Artech House, 1991.
- [11] G. W. Stimson, *Introduction to Airborne Radar*. Mendham, New Jersey: SciTech Publishing, Inc., 1998.

- [12] I. G. Cumming and F. H. Wong, *Digital Processing of Synthetic Aperture Radar Data, Algorithms and Implementation*. Boston: Artech House, 2005.
- [13] M. Soumekh, *Synthetic Aperture Radar Signal Processing with MATLAB Algorithms*. New York: John Wiley & Sons, Inc., 1999.
- [14] J. C. Curlander and R. N. McDonough, *Synthetic Aperture Radar - Systems and Signal Processing*. New York: John Wiley & Sons, 1991.
- [15] H. Klausning and W. Holpp, *Radar mit realer und synthetischer Apertur*. München: Oldenburg Verlag, 2000.
- [16] L. M. H. Ulander, H. Hellsten, and G. Stenström, "Synthetic-Aperture Radar Processing Using Fast Factorized Back-Projection," *IEEE Transactions on Aerospace and Electronic Systems*, vol. 39, no. 3, pp. 760–776, July 2003.
- [17] C. Cafforio, C. Prati, and F. Rocca, "SAR Data Focusing Using Seismic Migration Techniques," *IEEE Transactions on Aerospace and Electronic Systems*, vol. 27, no. 2, pp. 194–207, Mar. 1991.
- [18] W. G. Carrara, R. S. Goodman, and R. M. Majewski, *Spotlight Synthetic Aperture Radar: Signal Processing Algorithms*. Boston: Artech House Inc., 1995.
- [19] R. K. Raney, H. Runge, R. Bamler, I. G. Cumming, and F. H. Wong, "Precision SAR Processing Using Chirp Scaling," *IEEE Transactions on Geoscience and Remote Sensing*, vol. 32, no. 4, pp. 786–799, July 1994.
- [20] A. Moreira and Y. Huang, "Airborne SAR Processing of Highly Squinted Data Using a Chirp Scaling Approach with Integrated Motion Compensation," *IEEE Transactions on Geoscience and Remote Sensing*, vol. 32, no. 5, pp. 1029–1040, Sept. 1994.
- [21] A. Moreira, J. Mittermayer, and R. Scheiber, "Extended Chirp Scaling Algorithm for Air- and Spaceborne SAR Data Processing in Stripmap and ScanSAR Imaging Modes," *IEEE Transactions on Geoscience and Remote Sensing*, vol. 34, no. 5, pp. 1123–1136, Sept. 1996.
- [22] M. Sack, M. R. Ito, and I. G. Cumming, "Application of Efficient Linear FM Matched Filtering Algorithms to Synthetic Aperture Radar Processing," *IEE Proceedings Part F Communications*, vol. 132, no. 1, pp. 45–57, Feb. 1985.
- [23] R. Bamler, "A Comparison of Range-Doppler and Wavenumber Domain SAR Focusing Algorithms," *IEEE Transactions on Geoscience and Remote Sensing*, vol. 30, no. 4, pp. 706–713, July 1992.
- [24] L. J. Cutrona, W. E. Vivian, E. N. Leith, and G. O. Hall, "A High Resolution Radar Combat Surveillance System," *IRE Transactions on Military Electronics*, vol. 5, pp. 127–131, Apr. 1961.

- [25] M. M. J. L. van de Kamp, "Statistical Analysis of Rain Fade Slope," *IEEE Transactions on Antennas and Propagation*, vol. 51, no. 8, pp. 1750–1759, Aug. 2003.
- [26] H. J. Liebe, "Atmospheric EHF Window Transparencies Near 35, 90, 140 and 220 GHz," *IEEE Transactions on Antennas and Propagation*, vol. 31, no. 1, pp. 127–135, Jan. 1983.
- [27] N. C. Curie and C. E. Brown, Eds., *Principles and Applications of Millimeter-Wave Radar*. Norwood: Artech House Inc., 1987.
- [28] H. Essen, A. Wahlen, R. Sommer, G. Konrad, M. Schlechtweg, and A. Tessmann, "Very High Bandwidth Millimetre-Wave Radar," *IEE Electronics Letters*, vol. 41, no. 22, pp. 1247–1249, Oct. 2005.
- [29] M. Edrich, "Design Overview and Flight Test Results of the Miniaturised SAR Sensor MISAR," *Proceedings of the First European Radar Conference EURAD*, pp. 205–208, Oct. 2004.
- [30] R. K. Raney, "Synthetic Aperture Imaging Radar and Moving Targets," *IEEE Transactions on Aerospace and Electronic Systems*, vol. 7, pp. 499–505, May 1971.
- [31] J. K. Jao, "Theory of Synthetic Aperture Radar Imaging of a Moving Target," *IEEE Transactions on Geoscience and Remote Sensing*, vol. 39, no. 9, pp. 1984–1994, Sept. 2001.
- [32] M. Soumekh, "Moving Target Detection and Imaging Using an X-Band Along-Track Monopulse SAR," *IEEE Transactions on Aerospace and Electronic Systems*, vol. 38, no. 1, pp. 315–333, Jan. 2002.
- [33] S. R. J. Axelsson, "Position Correction of Moving Targets in SAR-Imagery," *Proceedings of SPIE*, vol. 5236, pp. 80–92, Jan. 2004.
- [34] R. Lipps, V. C. Chen, and M. Bottoms, "Advanced SAR GMTI Techniques," *Proceedings of the IEEE Radar Conference*, pp. 105–110, Apr. 2004.
- [35] R. G. White and D. J. Coe, "Detection Limits for Sideways Looking MTI Radars," *Radar 97*, pp. 434–438, Oct. 1997.
- [36] M. Soumekh, "Moving Target Detection in Foliage Using Along Track Monopulse Synthetic Aperture Radar Imaging," *IEEE Transactions on Image Processing*, vol. 6, no. 8, pp. 1148–1163, Aug. 1997.
- [37] V. C. Chen, F. Li, S.-S. Ho, and H. Wechsler, "Micro-Doppler Effect in Radar: Phenomenon, Model, and Simulation Study," *IEEE Transactions on Aerospace and Electronic Systems*, vol. 42, no. 1, pp. 2–21, Jan. 2006.

- [38] M. T. Fennell and R. P. Wishner, "Battlefield Awareness Via Synergistic SAR and MTI Exploitation," *IEEE Aerospace and Electronics Systems Magazine*, vol. 13, no. 2, pp. 39–45, Feb. 1998.
- [39] Z. Lu, R. Fatland, M. Wyss, S. Li, J. Eichelberger, K. Dean, and J. Freymueller, "Deformation of New Trident Volcano Measured by ERS-1 SAR Interferometry, Katmai National Park, Alaska," *Geophysical Research Letters*, vol. 24, no. 6, pp. 695–698, June 1997.
- [40] D. Massonnet, M. Rossi, C. Carmona, F. Adragna, G. Peltzer, K. Feigl, and T. Rabautte, "The Displacement Field of the Landers Earthquake Mapped by Radar Interferometry," *Nature*, vol. 364, pp. 138–142, July 1993.
- [41] K. E. Mattar, P. W. Vachon, D. Geudtner, A. L. Gray, I. G. Cumming, and M. Brugman, "Validation of Alpine Glacier Velocity Measurements Using ERS Tandem-Mission SAR Data," *IEEE Transactions on Geoscience and Remote Sensing*, vol. 36, no. 3, pp. 974–984, May 1998.
- [42] M. Bao, "On the Imaging of a Two-Dimensional Ocean Surface Wave Field by an Along-Track Interferometric Synthetic Aperture Radar," Ph.D. dissertation, Universität Hamburg, Hamburg, 1995.
- [43] R. Romeiser and D. R. Thompson, "Numerical Study on the Along-Track Interferometric Radar Imaging Mechanism of Oceanic Surface Currents," *IEEE Transactions on Geoscience and Remote Sensing*, vol. 38, no. 1, pp. 446–458, Jan. 2000.
- [44] S. J. Frasier and A. J. Camps, "Dual-Beam Interferometry for Ocean Surface Current Vector Mapping," *IEEE Transactions on Geoscience and Remote Sensing*, vol. 39, no. 2, pp. 401–414, Feb. 2001.
- [45] R. Romeiser, H. Breit, M. Eineder, H. Runge, P. Flament, K. de Jong, and J. Vogelzang, "Current Measurements by SAR Along-Track Interferometry from a Space Shuttle," *IEEE Transactions on Geoscience and Remote Sensing*, vol. 43, no. 10, pp. 2315–2324, Oct. 2005.
- [46] O. Eckert, M. Rombach, A. Holz, C. Hofmann, and M. Schwäbisch, "Traffic Monitoring Using Along Track Airborne Interferometric SAR Systems," *Conference Proceedings of 7th World Congress on Intelligent Transport Systems, Torino, Italy*, Nov. 2000.
- [47] H. Breit, M. Eineder, J. Holzner, H. Runge, and R. Bamler, "Traffic Monitoring Using SRTM Along-Track Interferometry," *Proceedings of the IEEE International Geoscience and Remote Sensing Symposium IGARSS*, vol. 2, pp. 1187–1189, July 2003.
- [48] M. Werner, "Shuttle Radar Topography Mission (SRTM) - Mission Overview," *Proceedings of EUSAR*, pp. 209–212, May 2000.

- [49] C. E. Livingstone and A. A. Thompson, "The Moving Object Detection Experiment on RADARSAT-2," *Canadian Journal of Remote Sensing*, vol. 30, no. 3, pp. 355–368, June 2004.
- [50] H. Runge, M. Eineder, G. Palubinskas, S. Suchandt, and F. Meyer, "Traffic Monitoring with TerraSAR-X," *Proceedings of the International Radar Symposium*, pp. 629–634, Sept. 2005.
- [51] J. Mittermayer and H. Runge, "Conceptual Studies for Exploiting the TerraSAR-X Dual Receive Antenna," *Proceedings of the IEEE International Geoscience and Remote Sensing Symposium IGARSS*, vol. 3, pp. 2140–2142, July 2003.
- [52] S. Suchandt, M. Eineder, R. Müller, A. Laika, S. Hinz, F. Meyer, and G. Palubinskas, "Development of a GMTI Processing System for the Extraction of Traffic Information from TerraSAR-X Data," *Proceedings of EUSAR*, pp. 1–4, May 2006.
- [53] J. Schulz-Stellenfleth, I. Hajnsek, and S. Lehner, "Retrieval of 2-D Current and Ocean Wave Information Using TanDEM-X in a Squinted Split Antenna Mode Configuration," *Proceedings of EUSAR*, pp. 1–4, May 2006.
- [54] C. E. Livingstone, I. C. Sikaneta, C. H. Gierull, S. Chiu, A. Beaudoin, J. Campbell, J. Beaudoin, S. Gong, and T. A. Knight, "An Airborne Synthetic Aperture Radar (SAR) Experiment to Support RADARSAT-2 Ground Moving Target Indication (GMTI)," *Canadian Journal of Remote Sensing*, vol. 28, no. 6, pp. 794–813, Dec. 2002.
- [55] A. Moccia and G. Rufino, "Spaceborne Along-Track SAR Interferometry: Performance Analysis and Mission Scenarios," *IEEE Transactions on Aerospace and Electronic Systems*, vol. 37, no. 1, pp. 199–213, Jan. 2001.
- [56] J. H. G. Ender and A. R. Brenner, "PAMIR - A Wideband Phased Array SAR/MTI System," *IEE Proceedings on Radar, Sonar and Navigation*, vol. 150, no. 3, pp. 165–172, June 2003.
- [57] G. Palubinskas, F. Meyer, H. Runge, P. Reinartz, R. Scheiber, and R. Bamler, "Estimation of Along-Track Velocity of Road Vehicles in SAR Data," *Proceedings of SPIE*, vol. 5982, no. 0T, pp. 1–9, Oct. 2005.
- [58] D. A. Imel, "AIRSAR Along-Track Interferometry Data," *AIRSAR Earth Science and Applications Workshop*, pp. 1–57, Mar. 2002.
- [59] H. Oriot and B. Vaizan, "Preliminary Results on Ground Moving Target Detection with L-Band Data Acquired with the RAMSES Sensor," *Proceedings of EUSAR*, pp. 1–4, May 2006.

- [60] S. I. Tsunoda, F. Pace, J. Stence, M. Woodring, W. H. Hensley, A. W. Doerry, and B. C. Walker, "Lynx: A High-Resolution Synthetic Aperture Radar," *Proceedings of the IEEE Aerospace Conference*, vol. 5, pp. 51–58, Mar. 2000.
- [61] J. H. G. Ender and R. Klemm, "Airborne MTI via Digital Filtering," *IEE Proceedings, Part F*, vol. 136, no. 1, pp. 22–28, Feb. 1989.
- [62] S. A. S. Werness, W. G. Carrara, L. S. Joyce, and D. B. Franczak, "Moving Target Imaging Algorithm for SAR Data," *IEEE Transactions on Aerospace and Electronic Systems*, vol. 26, no. 1, pp. 57–67, Jan. 1990.
- [63] H.-B. Sun, G.-S. Liu, H. Gu, and W.-M. Su, "Application of the Fractional Fourier Transform to Moving Target Detection in Airborne SAR," *IEEE Transactions on Aerospace and Electronic Systems*, vol. 38, no. 4, pp. 1416–1424, Oct. 2002.
- [64] J. R. Moreira and W. Keydel, "A New MTI-SAR Approach Using the Reflectivity Displacement Method," *IEEE Transactions on Geoscience and Remote Sensing*, vol. 33, no. 5, pp. 1238–1244, Sept. 1995.
- [65] J. J. Sharma, C. H. Gierull, and M. J. Collins, "The Influence of Target Acceleration on Velocity Estimation in Dual-Channel SAR-GMTI," *IEEE Transactions on Geoscience and Remote Sensing*, vol. 44, no. 1, pp. 134–135, Jan. 2006.
- [66] C. H. Gierull, "Statistical Analysis of Multilook SAR Interferograms for CFAR Detection of Ground Moving Targets," *IEEE Transactions on Geoscience and Remote Sensing*, vol. 42, no. 4, pp. 691–701, Apr. 2004.
- [67] S. Chiu, "A Constant False Alarm Rate (CFAR) Detector for RADARSAT-2 Along-Track Interferometry," *Canadian Journal of Remote Sensing*, vol. 31, no. 1, pp. 73–84, Feb. 2005.
- [68] A. Das and R. Cobb, "TechSat 21—Space Missions Using Collaborating Constellations of Satellites," *Proceedings of the 12th AIAA/USU Conference on Small Satellites*, pp. 1–5, Aug. 1998.
- [69] M. Martin and M. J. Stallard, "Distributed Satellite Missions and Technologies—The TechSat 21 Program," *Proceedings of AIAA Space Technology Conference and Exposition*, Sept. 1999.
- [70] D. Massonnet, "Capabilities and Limitations of the Interferometric Cartwheel," *IEEE Transactions on Geoscience and Remote Sensing*, vol. 39, no. 3, pp. 506–520, Mar. 2001.
- [71] Z. Li, Z. Bao, H. Wang, and G. Liao, "Performance Improvement for Constellation SAR Using Signal Processing Techniques," *IEEE Transactions on Aerospace and Electronic Systems*, vol. 42, no. 2, pp. 436–452, Apr. 2006.

- [72] U. Ouchi, "On the Multilook Images of Moving Targets by Synthetic Aperture Radars," *IEEE Transactions on Antennas and Propagation*, vol. 33, no. 8, pp. 823–827, Aug. 1985.
- [73] M. Kirscht, "Detection and Imaging of Arbitrarily Moving Targets with Single-Channel SAR," *IEE Proceedings on Radar, Sonar and Navigation*, vol. 150, no. 1, pp. 7–11, Feb. 2003.
- [74] J. M. B. Dias and P. A. C. Marques, "Multiple Moving Target Detection and Trajectory Estimation Using a Single SAR Sensor," *IEEE Transactions on Aerospace and Electronic Systems*, vol. 39, no. 2, pp. 604–624, Apr. 2003.
- [75] S. Chiu and C. E. Livingstone, "A Comparison of Displaced Phase Centre Antenna and Along-Track Interferometry Techniques for RADARSAT-2 Ground Moving Target Indication," *Canadian Journal of Remote Sensing*, vol. 31, no. 1, pp. 37–51, Feb. 2005.
- [76] J. H. G. Ender, "Space-Time Processing for Multichannel Synthetic Aperture Radar," *Electronics and Communication Engineering Journal*, vol. 11, no. 1, pp. 29–38, Feb. 1999.
- [77] L. E. Brennan and I. S. Reed, "Theory of Adaptive Radar," *IEEE Transactions on Aerospace and Electronic Systems*, vol. 9, no. 2, pp. 237–252, Mar. 1973.
- [78] J. Ward, *Space-Time Adaptive Processing for Airborne Radar*. Lexington, Massachusetts: Lincoln Laboratory, Massachusetts Institute of Technology, Technical Report 1015, Dec. 1994.
- [79] J. H. G. Ender, "Space-Time Adaptive Processing for Synthetic Aperture Radar," *IEE Colloquium on Space-Time Adaptive Processing*, pp. 6/1–6/18, Apr. 1998.
- [80] R. Klemm, *Principles of Space-Time Adaptive Processing*. London: The Institution of Electrical Engineers, 2002.
- [81] J. R. Guerci, *Space-Time Adaptive Processing for Radar*. Norwood, MA: Artech House, 2003.
- [82] R. Klemm, Ed., *Applications of Space-Time Adaptive Processing*. London: The Institution of Electrical Engineers, 2004.
- [83] S. Barbarossa, "Detection and Imaging of Moving Objects with Synthetic Aperture Radar. Part 1: Optimal Detection and Parameter Estimation Theory," *IEE Proceedings, Part F*, vol. 139, no. 1, pp. 79–88, Feb. 1992.
- [84] S. Barbarossa and A. Farina, "Detection and imaging of Moving Objects with Synthetic Aperture Radar. Part 2: Joint Time-Frequency Analysis by Wigner-Ville Distribution," *IEE Proceedings, Part F*, vol. 139, no. 1, pp. 89–97, Feb. 1992.

- [85] S. Barbarossa and A. Farina, "Space-Time-Frequency Processing of Synthetic Aperture Radar Signals," *IEEE Transactions on Aerospace and Electronic Systems*, vol. 30, no. 2, pp. 341–358, Apr. 1994.
- [86] C. Liu, "Effects of Target Motion on Polarimetric SAR Images," *Canadian Journal of Remote Sensing*, vol. 32, no. 2, pp. 51–64, Apr. 2006.
- [87] C. Liu and C. H. Gierull, "Using Ambiguities to Aid in Moving Target Detection in PolSAR Images," *Proceedings of EUSAR*, pp. 1–4, May 2006.
- [88] M. Jahangir, "Detecting Moving Targets in SAR Imagery Through Shadow Tracking," *Proceedings of EUSAR*, pp. 1–4, May 2006.
- [89] B. C. Armstrong and H. D. Griffiths, "Use of Difference Channel Information for Detection in Monopulse Radars," *IEE Proceedings of Radar and Signal Processing, F*, vol. 138, no. 3, pp. 199–210, June 1991.
- [90] T. Hagfors, "Some Properties of Radio Waves Reflected from the Moon and Their Relation to the Lunar Surface," *Journal of Geophysical Research*, vol. 66, no. 3, pp. 777–785, Mar. 1961.
- [91] A. E. Rogers and R. P. Ingalls, "Venus: Mapping the Surface Reflectivity by Radar Interferometry," *Science*, vol. 165, no. 3895, pp. 797–799, Aug. 1969.
- [92] L. C. Graham, "Synthetic Interferometer Radar for Topographic Mapping," *Proceedings of the IEEE*, vol. 62, pp. 763–768, June 1974.
- [93] H. A. Zebker and R. M. Goldstein, "Topographic Mapping from Interferometric Synthetic Aperture Radar Observations," *Journal of Geophysical Research*, vol. 91, no. B5, pp. 4993–4999, Apr. 1986.
- [94] R. M. Goldstein and H. A. Zebker, "Interferometric Radar Measurement of Ocean Surface Currents," *Nature*, vol. 328, pp. 707–709, Aug. 1987.
- [95] R. M. Goldstein, H. Engelhardt, B. Kamb, and R. M. Frolich, "Satellite Radar Interferometry for Monitoring Ice Sheet Motion: Application to an Antarctic Ice Stream," *Science*, vol. 262, no. 5139, pp. 1525–1530, Dec. 1993.
- [96] S. N. Madsen and H. A. Zebker, *Imaging Radar Interferometry*. New York: Principles and Applications of Imaging Radar, Manual of Remote Sensing, Third Edition, Volume 2, John Wiley & Sons, 1998, pp. 359–380.
- [97] R. Bamler and P. Hartl, "Synthetic Aperture Radar Interferometry," *Inverse Problems*, vol. 14, pp. 1–54, Aug. 1998.
- [98] D. Small, "Generation of Digital Elevation Models Through Spaceborne SAR Interferometry," Ph.D. dissertation, University of Zürich, Remote Sensing Laboratories, Department of Geography, Zürich, 1998.

- [99] P. A. Rosen, S. Hensley, I. R. Joughin, F. K. Li, S. N. Madsen, E. Rodriguez, and R. M. Goldstein, "Synthetic Aperture Radar Interferometry," *Proceedings of the IEEE*, vol. 88, no. 3, pp. 333–382, Mar. 2000.
- [100] R. F. Hanssen, *Radar Interferometry*. Dordrecht: Kluwer Academic Publishers, 2001.
- [101] L. G. Brown, "A Survey of Image Registration Techniques," *ACM Computing Surveys*, vol. 24, no. 4, pp. 325–376, Dec. 1992.
- [102] R. Scheiber and A. Moreira, "Coregistration of Interferometric SAR Images Using Spectral Diversity," *IEEE Transactions on Geoscience and Remote Sensing*, vol. 38, no. 5, pp. 2179–2191, Sept. 2000.
- [103] E. Sansosti, P. Berardino, M. Manunta, F. Serafino, and G. Fornaro, "Geometrical SAR Image Registration," *IEEE Transactions on Geoscience and Remote Sensing*, vol. 44, no. 10, pp. 2861–2870, Oct. 2006.
- [104] C. W. Chen and H. A. Zebker, "Phase Unwrapping for Large SAR Interferograms: Statistical Segmentation and Generalized Network Models," *IEEE Transactions on Geoscience and Remote Sensing*, vol. 40, no. 8, pp. 1709–1719, Aug. 2002.
- [105] A. M. Guarnieri and C. Prati, "SAR Interferometry: a "Quick and Dirty" Coherence Estimator for Data Browsing," *IEEE Transactions on Geoscience and Remote Sensing*, vol. 35, no. 3, pp. 660–669, May 1997.
- [106] D. Just and R. Bamler, "Phase Statistics of Interferograms with Applications to Synthetic Aperture Radar," *Applied Optics*, vol. 33, no. 20, pp. 4361–4368, July 1994.
- [107] C. Wimmer, R. Siegmund, M. Schwäbisch, and J. ao R. Moreira, "Generation of High-Precision DEMs of the Wadden Sea with Airborne Interferometric SAR," *IEEE Transactions on Geoscience and Remote Sensing*, vol. 38, no. 5, pp. 2234–2245, Sept. 2000.
- [108] M. A. Sletten, "An Analysis of Gradient-Induced Distortion in ATI-SAR Imagery of Surface Currents," *IEEE Transactions on Geoscience and Remote Sensing*, vol. 44, no. 7, pp. 1995–2002, July 2006.
- [109] R. Siegmund, M. Bao, S. Lehner, and R. Mayerle, "First Demonstration of Surface Currents Imaged by Hybrid Along- and Cross-Track Interferometric SAR," *IEEE Transactions on Geoscience and Remote Sensing*, vol. 42, no. 3, pp. 511–519, Mar. 2004.
- [110] M. Rüegg, E. Meier, and D. Nüesch, "Constant Motion, Acceleration, Vibration, and Rotation of Objects in SAR Data," *Proceedings of SPIE*, vol. 5980, no. 05, pp. 48–59, Oct. 2005.

- [111] L. Cohen, "Time-Frequency Distributions — A Review," *Proceedings of the IEEE*, vol. 77, no. 7, pp. 941–981, July 1989.
- [112] F. Auger, P. Flandrin, P. Goncalves, and O. Lemoine. (1996) Time-Frequency Toolbox for Use with MATLAB. [Online]. Available: <http://tftb.nongnu.org/>
- [113] V. C. Chen and H. Ling, *Time-Frequency Transforms for Radar Imaging and Signal Analysis*. Boston: Artech House, 2002.
- [114] V. C. Chen, F. Li, S.-S. Ho, and H. Wechsler, "Analysis of Micro-Doppler Signatures," *IEE Proceedings on Radar, Sonar and Navigation*, vol. 150, no. 4, pp. 271–276, Aug. 2003.
- [115] J. J. Sharma and M. J. Collins, "Simulation of SAR Signals from Moving Vehicles (Focusing Accelerating Ground Moving Targets)," *Proceedings of EUSAR*, vol. 2, pp. 841–844, May 2004.
- [116] J. L. Walker, "Range-Doppler Imaging of Rotating Objects," *IEEE Transactions on Aerospace and Electronic Systems*, vol. 16, no. 1, pp. 23–52, Jan. 1980.
- [117] N. S. Subotic, B. J. Thelen, and D. A. Carrara, "Cyclostationary Signal Models for the Detection and Characterization of Vibrating Objects in SAR Data," *Conference Record of the Thirty-Second Asilomar Conference on Signals, Systems and Computers*, vol. 2, pp. 1304–1308, Nov. 1998.
- [118] S. D. Silverstein and C. E. H. III, "Synthetic Aperture Radar Image Signature of Rotating Objects," *Conference Record of the Thirty-Eighth Asilomar Conference on Signals, Systems, and Computers*, vol. 2, pp. 1663–1667, Nov. 2004.
- [119] T. Sparr and B. Krane, "Time-Frequency Analysis of Vibrating Targets in Airborne SAR Systems," *IEE Proceedings on Radar, Sonar and Navigation*, vol. 150, no. 3, pp. 173–176, June 2003.
- [120] T. Sparr and B. Krane, "Micro-Doppler Analysis of Vibrating Targets in SAR," *IEE Proceedings on Radar, Sonar and Navigation*, vol. 150, no. 4, pp. 277–283, Aug. 2003.
- [121] D. Nüssler, H. Essen, and D. Büth, "Vehicle Classification by Vibration Analysis Using Millimeterwave Sensors," *Proceedings of the International Conference on Infrared and Millimeter Waves*, vol. 2, pp. 349–350, Sept. 2005.
- [122] *MS2002+ Acceleration Sensor Manual*, Syscom Instruments SA, Switzerland, 2002.
- [123] J. Li and H. Ling, "Application of Adaptive Chirplet Representation for ISAR Feature Extraction from Targets with Rotating Parts," *IEE Proceedings on Radar, Sonar and Navigation*, vol. 150, no. 4, pp. 284–291, Aug. 2003.

- [124] S. M. Sherman, *Monopulse Principles and Techniques*. Boston: Artech House Publishers, 1984.
- [125] D. K. Barton, *Monopulse Radar*. Artech House, 1977.
- [126] D. R. Rhodes, *Introduction to Monopulse*. Artech House, 1980.
- [127] H. T. Budenbom, "Monopulse Automatic Tracking and the Thermal Bound," *Convention Record of IRE First National Convention on Military Electronics*, vol. 20, pp. 387–392, June 1957.
- [128] S. Raman, N. S. Barker, and G. M. Rebeiz, "A W-Band Dielectric-Lens-Based Integrated Monopulse Radar Receiver," *IEEE Transactions on Microwave Theory and Techniques*, vol. 46, no. 12, pp. 2308–2316, Dec. 1998.
- [129] U. Nickel, "Overview of Generalized Monopulse Estimation," *IEEE Aerospace and Electronic Systems Magazine*, vol. 21, no. 6, pp. 27–56, June 2006.
- [130] J. Thraves and S. Fairweather, "Compact 24 Horn Linear Array," *Proceedings of the IEE Seventh International Conference on Antennas and Propagation, ICAP*, vol. 1, pp. 209–212, Apr. 1991.
- [131] L. Armijo, "A Theory for the Determination of Wind and Precipitation Velocities with Doppler Radars," *Journal of the Atmospheric Sciences*, vol. 26, no. 3, pp. 570–573, May 1969.
- [132] R. J. Doviak, D. S. Zrnic, and D. S. Sirmans, "Doppler Weather Radar," *Proceedings of the IEEE*, vol. 67, no. 22, pp. 1522–1553, Nov. 1979.
- [133] D. P. Jorgensen, T. R. Shepherd, and A. S. Goldstein, "A Dual-Pulse Repetition Frequency Scheme for Mitigating Velocity Ambiguities of the NOAA P-3 Airborne Doppler Radar," *Journal of Atmospheric and Oceanic Technology*, vol. 17, no. 5, pp. 585–594, May 2000.
- [134] G. Corsini, M. Diani, F. Lombardini, and G. Pinelli, "Simulated Analysis and Optimization of a Three-Antenna Airborne InSAR System for Topographic Mapping," *IEEE Transactions on Geoscience and Remote Sensing*, vol. 37, no. 5, pp. 2518–2529, Sept. 1999.
- [135] W. H. Press, B. P. Flannery, S. A. Teukolsky, and W. T. Vetterling, *Numerical Recipes in C: The Art of Scientific Computing, Second Edition*. Cambridge: Cambridge University Press, 1992.
- [136] G. Palubinskas, H. Runge, and P. Reinartz, "Radar Signatures of Road Vehicles: Airborne SAR Experiments," *Proceedings of SPIE*, vol. 5980, no. 06, pp. 60–70, Sept. 2005.

Index

- $\Sigma\Delta$ processing, *see* Monopulse
- Aircraft, 5
 - C-160 Transall, 113
 - movement, *see* Motion compensation
 - ultralight, 1
 - vibration, 64
- Along-track, *see* azimuth
- Along-track interferometry, *see* ATI
- Antenna, 1, 69, 114
 - aperture, 6, 30, 33
 - beam, 5, 9, 12, 14, 32, 68, 82
 - displaced phase center, *see* DPCA
 - footprint, 6
 - length, 11, 32
 - line of sight, 68
 - monopulse, 69
 - planar array, 32
 - radiation pattern, 31
 - rotating, 55, 60
- Aspect angle, 10, 30, 33, 38, 39, 44, 74
- ATI, 5, 15, 26, 67
 - baseline, 16, 77
 - GMTI, 15
 - principles, 16
 - river flow experiment, 22
 - theory, 18
- Attenuation, 1, 12
- Azimuth, 5
- Bandwidth, 7, 33, 111
- Baseline, 16, 77
 - perpendicular, 20
- Bessel function, 47
- Blind speed, 40, 67, 78, 91
- Cassegrain, 69
- CFAR, 14, 108, 111
- Chirp, 8
 - rate, 8
- Clutter, 3, 4, 14, 35, 42, 56, 63, 76
 - endo-clutter target, 83
 - exo-clutter target, 83
 - spectrum, 83
- Coherence, 21, 26
- Constant false alarm rate, *see* CFAR
- Continuous wave, *see* CW
- Cross-range, 5
- CW, 6, 68
- Differential GPS, *see* GPS
- Displaced phase center antenna, *see* DPCA
- Divergence angle, 30
- Doppler, 9, 14
 - ambiguity, 2, 4, 40, 78, 109
 - centroid, 88, 96, 104, 110
 - domain, 15
 - frequency, 18
 - history, 10, 36
 - micro-Doppler, 36, 46, 53, 55, 63, 109, 111
 - range-Doppler, 4, 81
 - range-Doppler processing, 11
 - shift, 6, 10, 15, 18, 29, 36, 39, 40, 47, 55, 63, 67, 76, 79, 82, 109, 110
 - spectrum, 48, 60
- DPCA, 15
- Dwell time, 6, 10, 29, 37, 42, 48, 57, 62, 64
- EHF, 12
- Extremely high frequency, *see* EHF
- Fast time, 5

- FGAN-FHR, 113
 FMCW, 6, 68
 Fourier transform, 8
 Frequency modulated continuous wave, *see* FMCW
 Global positioning system, *see* GPS
 GMTI, 1, 2, 14, 67
 - amplitude-comparison monopulse, 3, 77
 - dual-frequency, 80
 - experiments, 89, 94, 100, 104, 106
 - implementation, 84
 - radar, 14
 - SAR, 13, 14
 - spaceborne, 14, 15
 - theory, 81
 GPS, 4, 22
 - differential (dGPS), 4, 89–91, 97, 98
 Ground moving target indication, *see* GMTI
 Illumination time, *see* Dwell time
 Inertial navigation system, *see* INS
 INS, 22
 InSAR, 16, 67, 69
 - applications, 78
 - decorrelation, 16
 - phase unwrapping, 21
 - relation to monopulse, 72, 73
 - theory, 18
 Interferometric SAR, *see* InSAR
 Least common multiple, 78
 Master image, 18, 72
 Matched filter, 8
 MEMPHIS, 12, 33, 34, 48, 51, 58, 64, 67, 69, 77–79, 82, 85, 89, 94, 100, 105, 110, 113
 METAS, 100
 Micro-Doppler, *see* Doppler
 Millimeter wave, *see* mmW
 Miniaturization, 1, 12
 mmW, 1, 12, 46, 77, 109
 - advantages, 29
 - GMTI, 2, 3, 63, 106
 Monopulse, 67
 - amplitude-comparison, 69, 71, 73, 77
 - curve, 74, 104
 - definition, 68
 - difference channel, 70, 73
 - MEMPHIS, 77
 - phase-comparison, 68
 - processing, 67, 81
 - processing algorithm, 84
 - radar, 68
 - ratio, 73
 - SAR, 76
 - sum channel, 70, 73
 Monopulse Ratio, 73, 74, 76, 81, 85
 Motion compensation, 12, 100, 108, 110
 Moving target, *see* Target
 Off-nadir, 6, 21
 Paired echoes, 47, 48, 51, 64
 Phase, 18, 31, 36, 70
 - difference, 73, 74
 - interferometric, 19
 - sensitivity, 29
 PRF, 14, 22, 29, 40, 57, 78, 83, 84, 110
 PRI, 5
 Pulse duration, 8, 33
 Pulse repetition frequency, *see* PRF
 Radar, 1
 - coherent, 5
 - continuous wave, 5
 - monopulse, 68
 - pulsed, 5
 - synthetic aperture, *see* SAR
 Range, 5
 Reconnaissance, 1, 63, 111
 Resolution, 1, 12, 111
 - in azimuth, 6, 11
 - in range, 7, 9
 Rotation
 - earth, 14

- target, *see* Target
- SAR, 1
 - azimuth processing, 9
 - Doppler history, 37
 - dual-frequency, 29, 78
 - GMTI, 2, 13, 14, 67, 109
 - monopulse, 76
 - processing, 6, 11
 - range compression, 7
 - signal theory, 32
 - simulations, 36
 - system model, 31
 - theory, 5
- SAR Interferometry, *see* InSAR
- Shuttle Radar Topography Mission, *see* SRTM
- Signal to noise ratio, *see* SNR
- Slant Range, 5
- Slave image, 18, 72
- Slow Time, 5
- SNR, 12, 22
- Space-time adaptive processing, *see* STAP
- Squint angle
 - monopulse, 74
 - SAR, 6
- SRTM, 13
- STAP, 15, 108, 111
- Synthetic aperture radar, *see* SAR
- Target, 6
 - acceleration, 44
 - constant movement, 38
 - displacement, 29, 38, 64, 76
 - displacement correction, 3, 13, 14, 67, 83, 105, 108, 110
 - of opportunity, 3, 89, 100, 104
 - point target, 6
 - reflectivity, 33
 - rotation, 54, 56, 58, 104
 - smearing and defocus, 2, 29, 40, 100, 103
 - vibration, 46, 48, 51
- amplitude, 84, 90
- monopulse, 86, 90
- Time-frequency analysis, 2, 35, 42, 45, 48, 53, 57, 60
- Traffic monitoring, 1, 13, 15, 100, 111
 - vibrations, 47
- UAV, 12
- Unmanned aerial vehicle, *see* UAV
- Velocity ambiguity, 40, 67, 78
- Velocity estimation, 67, 90
 - ambiguous, 80
- Vibration, *see* Target
- Wavelength, 2, 12, 29, 77, 78
- Wigner-Ville distribution, *see* WVD
- WVD, 35
 - pseudo, 35
 - smoothed pseudo, 35, 36

About the Author

Maurice Rüegg was born in Kilchberg ZH, Switzerland, on May 4, 1978. He grew up in Zollikon at the beautiful shores of Lake Zurich. After visiting primary school, he attended the Realgymnasium Rämibühl in Zurich where he received a humanistic education, interrupted in 1995 when he spent a year in Rochester, New York, for the Senior year of high school. In 1998, he received the Matura Typus B and joined the Swiss Federal Institute of Technology in Zurich (ETH) to study electrical engineering and information technology. He received a master of science (dipl. El.-Ing. ETH) in 2003 after finishing his master's thesis "Virtual Private Network Provisioning in the Hose Model" at the Computer Engineering and Networks Laboratory. Two weeks later, he started working as a research and teaching assistant at the Remote Sensing Laboratories (RSL) of the University of Zurich. The dissertation at hand marks the completion of his work as a Ph.D. student during the years at RSL. He lives in Küsnacht with Vanessa, his favorite dentist of many years.

ISBN 978-3-03703-014-1



9 783037 030141